Simulations of Optical Effects in Nanostructures

Author: Yun Peng

Boston College

The Graduate School of Arts and Sciences

Department of Physics

SIMULATIONS OF OPTICAL EFFECTS IN NANOSTRUCTURES

A dissertation by

YUN PENG

submitted in partial fulfillment of the requirement for the degree of

Doctor of Philosophy

October, 2011

Abstract

In my work presented in this dissertation, I have focused on simulation studies of light interaction with nanostructures made of metals and dielectrics. Of particular interest have been plasmonic effects. The structures included the wire and coaxial nanowaveguides, as well as periodic arrays of planar quasi-triangles, and periodic arrays of nanoholes in thin metallic films. In the nanowaveguides I focused on plasmon polariton modes which resemble the TEM modes propagating in the corresponding conventional radio transmission lines. This collaborative research, involving an experimental effort, showed how the nanoscopic plasmon polariton modes reduce in the retarded limit to the TEM modes, and in the non-retarded limit to the corresponding surface plasmon modes. My simulations explained details of recent experimental results involving plasmonic waveguiding in metallic nanowires. Similar results have been obtained for nanocoaxial waveguides. My simulations of the optical absorption in the arrays of nano quasi-triangles, recently observed experimentally, helped identify those as due to Mie plasmonic resonances in these nanoparticles. They also explained the peak shifts in terms of the 2D surface plasmon dispersion, and the plasmon momentum quantization. In the study of the arrays evolution from holes to quasi-triangles, my simulations provided the clue to the critical behavior of the peak position for structures approaching the percolation threshold (the transitional structure in the series, for which film resistance diverges), and allowed to identify the series of structures as an analog of the percolation threshold problem. Finally, I have simulated optical performance of nanorod arrays (or multi-core nanocoax), which have been employed as platform for novel solar cells. My simulations have been employed to predict and optimize these cells. My work resulted in 5 publications and 2 manuscripts in preparation.

List of Contents

Acknowledgement

It is my pleasure to acknowledge the people, without whom this dissertation would not have been possible.

I am heartily thankful to my PhD advisor, Prof. Krzysztof Kempa, for providing me with the opportunity to study an exciting field of plasmonics. His broad view of physics and deep understanding of the field impressed me constantly. Also, he always inspired me to become better in the subject.

I owe deep gratitude to my committee member, Prof. Michael Naughton, who has been supportive throughout my graduate study. His constructive suggestions benefited me greatly and his positive attitude had great influence on my professional development.

I would like to express my sincere thanks to the other committee member, Prof. Kevin Bedell, who provided support and mentorship in many ways. He helped me to get through some of the difficult moments of my graduate life.

Great appreciation is given to my supervisor, Prof. Andrzej Herczynski, who allowed me the flexibility to do my research while working with him. He is also very inspiring and encouraging physicist and I am honored to work with him.

I would like to thank everybody in the physics department, including the professors, graduate students, administrative and research staff, for helping me in many ways. I give thanks to my friends, whose company made the journey more enjoyable.

Lastly, I want to give special thanks to my parents, Yuee Wang and Yuzhi Peng, for their eternal love and to Tomasz whose presence made all the difference in my life. This dissertation is dedicated to them.

List of Publications

Peng, Y., Wang, X., and Kempa, K., "TEM-like optical mode of a coaxial nanowaveguide," Opt. Express 16, 1758 (2008).

Peng, Y., Marcoux, C., Kempa, K., Patoka, P., Hilgendorff, M., and Giersig, M., "Plasmonics of thin film quasi-triangular nanoparticles", Applied Physics Letters 96, 133104 (2010).

Naughton, M.J., Kempa, K., Ren, Z.F., Argenti, N., Gao, Y., Rybczynski, J., Wang, Y., Gao, W., Shepard, A., Naughton, J.R., **Peng, Y.**, Paudel, T., Lan, Y., McMahon, G., Burns, M.J., Clary, M., Ballif, C., Haug, F-J., Söderström, T., Cubero, O., and Eminian, C., "Nanocoax: A New Platform for Low Cost, High Efficiency Solar Power," Phys. Status Solidi RRL 4, No. 7, 181– 183 (2010).

Peng, Y., Paudel, T., Chen, W.-C., Padilla, W. J., Ren, Z.F., and Kempa, K., "Percolation and polaritonic effects in periodic planar nanostructures evolving from holes to islands", Applied Physics Letters 90, 041901 (2010).

Paudel, T., Rybczynski, J., Gao, Y.T., Lan, Y.C., **Peng, Y.**, Kempa, K., Naughton, M. J., and Ren, Z.F., "Nanocoax solar cells based on aligned multi-walled carbon nanotube arrays", Phys. Status Solidi A, 1– 4 (2011).

Nah, S., **Peng, Y.**, Ropp, C., Fourkas, J. T., Kempa, K., and Waks, E., "Photochemistry at a distance with guided, nonlinearly-generated emission in metal nanowires: A new paradigm for precision optical nanoassembly," submitted.

Peng, Y., and Kempa, K., "Surface plasmon propagation and coupling in silver nanowires", submitted.

List of Figures

Chapter 3

Chapter 4

Chapter 5

Chapter 1

Introduction

Plasmonics, a field emerged several decades ago, studies the interactions between electromagnetic waves, essentially light, and nanostructures consisting of metal and dielectrics. Because the charge carriers (often times free electrons) in metal form a plasma, these interactions can be viewed through the plasma dynamics (plasma waves and their resonances). Plasma frequency is the most important parameter for any plasma. The details of plasma frequency will be examined later, but its general physics significance can be described as: below plasma frequency, light reflects or scatters from the plasma; and above plasma frequency, light propagates through [Howard, 1992; Swanson, 2003].

The optical effects of nanostructures are tightly associated with surface plasma waves, which are electromagnetic waves at the interfaces of plasmas (free electron in metal). My PhD dissertation research is in the field of Plasmonics, and I focus on two kinds of nanostructures: nanowaveguides & the developed structures, and nanoparticle arrays & the developed structures. The dissertation is organized as follows.

In Chapter 1, a general introduction to plasmonics is given, including a brief history of the field, major achievements made and the challenges that still exist. The theoretical background of bulk plasmons and surface plasmons will then be given. Chapter 2 presents the two main methods used in my research which involve solving Maxwell's equations: the analytical method and the simulation method. The information about the material dispersion model and the actual parameters used in simulations is also introduced. In Chapter 3, the plasmonics of nanowires is investigated and its use in the fabrication of nanophotonic devices is presented. Chapter 4 studies nanocoaxial waveguide using both the analytical and the simulation method. The dissertation then moves on to a different nanostructure based on thin films. Chapter 5 studies the plasmonics of thin-film quasi-triangular nanoparticles and Chapter 6 studies the optical response of the nanostructure when it evolves from a nanohole array to a nanoquasi-triangular particle array. Chapter 7 presents the simulation results of the interaction of light with an array of nanopillars, including the propagation and absorbance of the light. Here also a proposal is made of the possible application in solar cell designs. Finally, a summary of the whole dissertation is given in Chapter 8.

1.1 Past, present and future

Long before investigations were made of the underlying physics of the optical effects of nanoparticles, its effects have been well-known and exploited to create vibrant colors in glass for thousands of years. One famous piece of work is the "Lycurgus cup" produced by Roman artisans dating back 2400 years ago. On the cup, the scene with Lycurgus is green when light comes from outside, but it turns bright red when the light is lit from inside the cup. The reason behind this exotic phenomenon, which remained unknown until about 100 years ago, is that the glass was stained by silver and gold particles of roughly 60nm and these nanoparticles reflect green light while transmitting red.

Some of the early scientific studies involving light and nanoparticles dates back to end of the 19^{th} century, when Lord Rayleigh formulated the theory of light scattering of dielectric particles that are much smaller than the wavelength of the incident light, and explained the blue color of the sky and red color of sunset. A few years after the development of the Drude Model [1900] of electric conduction in metals, it was used by Garnett to describe the bright colors of metal-stained glass [1904]. Soon after that, in 1908, Gustav Mie formulated his now well known "Mie theory" describing the general spherical scattering of the light by particles, dielectric or not, of various sizes. Mie theory agrees with the Rayleigh scattering theory for small particles and with geometric optics for large particles. Even to date, Mie theory is well cited in many areas of physics.

The field of plasma physics was developing around this time too. The first man-made plasma was discovered in the Crookes Tube in 1879, and its nature was identified by Thomson in 1897 as ionized gas. In the 1920's Langmuir borrowed the name "plasma" from biology to describe this state of matter, and used charge density waves, also known as Langmuir waves, to explain the oscillations of the plasma [Langmuir, 1928; Langmuir & Tonks, 1929]. The first person who derived the correct formula for the characteristic plasma frequency ω_p was actually H. Mott-Smith [Langmuir, 1928]. $\omega_p = \sqrt{ne^2 / \varepsilon_0 m}$, where n is the carrier density, e and m are charge and mass of an electron, respectively, and ε_0 is a constant called the vacuum permittivity.

A plasma is a gas composed of one or more of the following: ionized atoms and molecules (ions), and electrons. The nature of a plasma is not confined to the gas-state, as plasmas can exist in the 'solid-state'. Metals are the simplest solid-state plasma systems. In 1953, Bohm and Pines showed that one class of excitations in a strongly interacting electron gas (like that in metal) were longitudinal bulk plasmons, while the other was single-electron excitations. In 1956, David Pines predicted the "characteristic energy losses" experienced by fast electrons traveling through metals due to collective oscillation of free electrons. The existence of "surface plasmons" in thin metal films was first theoretically described as "collective oscillations" on metal surfaces by Ritchie (1957). These oscillations/excitations were experimentally demonstrated by Powell and Swan (1959), and were studied and named by Stern and Ferrell in 1960 "Surface plasmons", which are the quanta of the charge oscillations occurring at the interface.

1968 witnessed a major event in the development of the surface-plasma waves study when the methods used to optically excite surface-plasma waves on metal thin films were presented by Otto [1968], and Kretschmann and Raether [1968]. From then on, surface plasmons have became experimentally accessible to many researchers. In the same year, the uneven distribution of light on metal gratings, which was observed more than 60 years ago by Wood [1902], was explained [Ritchie, et al., 1968] by surface plasmon resonances excited on the gratings.

It wasn't until 1970 that the connection between the surface plasmons and the optical properties of metal nanoparticles was made [Kreibig and Zacharias, 1970]. Later, the term “surface plasmon polariton” was introduced to more accurately address the interaction between the oscillating electrons and the electromagnetic waves in the metal [Cunningham, et al., 1974].

Surface plasmons (SPs) describe the quantization of electron charge oscillations at the interface of a metal and a dielectric material. Surface plasmons have two major forms, from which various combinations can result: surface plasmon polaritons, often referred as surface plasmons, in which an electron density wave propagates along the metal-dielectric surface; and localized surface plasmons, in which an electron density wave becomes localized like a standing wave on the surface of the nanoparticles. SPs have many unique physical and optical properties which can result in interesting and exotic effects upon combination with different nanostructures, much of which is still under

investigation. These unique properties and effects can possibly be exploited in many practical applications in such fields as optical imaging, nano-manipulation, biotechnology, solar energy, and meta-materials.

Early work on SPs mainly focused on understanding the fundamental properties of solid state matter, and gradually has made the transition to more application-driven research. There have been many properties that have been studied and promising applications are currently being developed and predicted. Here I will give a brief introductory of a few of these unique structures and their optical properties in the field. Of course I will not be able to list all the work/ publications, and many good books and review papers collect more recent developments in the field [Brongersma & Kik, 2007; Maier, 2007; Pitarke et al., 2007; Shalaev & Kawata, 2007; Sweatlock, 2003].

The first system to address, one that has been mentioned a few times above, is one involving nanoparticles. Metal nanoparticles exhibit very different optical properties from their respective bulk-material properties. For example, silver and gold can show different colors (red and yellow etc.) from, well “silver” and “gold”, depending on their sizes. The optical properties, including transmission and absorption, are closely related to the plasma frequency of nanoparticles, which is very sensitive to the sizes and shapes of nanoparticles [Bohren & Huffman, 1983; Kreibig & Zacharias, 1970; Kreibig & Vollmer, 1994]. The SPs on metal nanoparticles can also couple to each other and can then be used to guide light. A lot of research has been done in this area, and possible

applications include optical waveguides, field enhancement, bridging-gaps in dielectric materials etc.

Structures based on metallic thin films are also being studied for their wave-guiding properties and their extraordinary transmission. SPs can propagate along the surface, and the slot waveguides have been studied by many researchers [Pendry, 2000; Lee et al.; 2000; Dionne et al., 2006; Wang & Kempa, 2007]. With simple structures built on metallic films, many exotic optical properties can result. The “extraordinary optical transmission” effect is one of these properties, and it was reported by Thomas Ebbesen and his coworkers in 1998. They studied the transmission of light through a sub-wavelength hole array on a 200nm thick silver film, and observed that there were sharp peaks at wavelengths a few times the hole size, with overall transmission more than that of the classical results from the 'open area'. Other properties and possible applications of thin metal film-based nanostructures include negative reflection perfect lenses, sub-wavelength lensing, and cloaking [Pendry, 2000; Barnes et al., 2003; Wang & Kempa, 2004; Zentgraf et al., 2007].

SPs can be strongly localized at the interface of the metal and dielectric material. The plasmonics on rough and smooth surfaces can be very different [Raether, 1988; Boyd et al., 1986]. It is the size and geometry of the interface, particularly one formed by nanoscale structures, rather than the light wavelength that determines the propagation properties of the SP fields. Nanostructures made from noble metals, such as silver and

gold, can support the propagation of SPs with wavelengths much shorter than the corresponding free-space wavelength [Nelayah et al., 2009; Sanders et al., 2006]. Many structures have been proposed to guide SPs, such as channel, groove, slit, hole, chain of particles and nanowires [Ebbesen et al., 1998; Kiyan et al., 2007; Krenn, 2000; Lamprecht et al., 2001; Lezec et al., 2002; Maier et al., 2002; Thio et al., 1999].

Junichi Takahara (1997) proposed the idea that metallic nanowires, which he called negative dielectric wires, could guide light with a sub-wavelength diameter. The metal nanowires can take different forms: wires, cylinder, coaxial cable etc. A lot of research has been done since then [Dickson & Lyon, 2000; Ditlbacher et al., 2005; Graff et al., 2005; Sanders, 2006; Baida et al., 2006; Rybczynski, et al., 2007; Peng et al., 2008]. The mechanism of waveguides made of metal nanowires is different from that of optical fibers, which use internal total reflection. Metal nanowire waveguides are based on SP propagation to create new opportunities to transport light at the sub-wavelength scale, and they mayprovide possibilities to build optical circuits.

The above mentioned areas are not classified as entirely distinct and often times they are intertwined with each other. There are many potential devices and applications of nanooptics developed recently based on plasmonics of nanostructures, such as bio-sensing (which was mentioned in almost half of the surface plasmon papers published), efficient photon collection (which can be useful in solar cell applications), photon switch, single-photon transistors, and long-range optical coupling [Englund, et al., 2005;

Birnbaum et al., 2005; Imamoglu et al., 1999] and many new meta-materials. Some other novel properties are also predicted for metal nanostructures [Schwartzberg & Zhang, 2008].

The prospect of controlling the propagation of light and the interactions of photons and optical structures is an exciting one and is a challenging field to enter in today's cutting edge nanoscale science and technology. The current fast development of plasmonics coincides with a crucial 'moment' of technology. A lot of current technologies are facing issues concerning fundamental physical 'limits'. Areas such as data storage, electronic circuits, and optical sensing are desperately in need of a make-over (or new substitution) to be able to keep developing. Some of these areas may be able to improve with the help of plasmonics, where SPs play an essential role in the optical properties. The possibilities of so many practical applications attract a lot of interest, and plasmonics has become a popular field for the last two decades. The fast growth of the field is also stimulated by the parallel development of many technological areas, such as advanced nanofabrication, and powerful computer and simulations algorithms/software.

With such fast development in the field, a lot of opportunities and challenges lay ahead too. First of all, a lot of the physics is still unknown or not fully explored. Secondly, due to SPs' unique dependency on the nanostructure, we are still just on our way to discover and develop a lot of new nanostructures/meta materials with new exotic optical properties and applications. Another challenge is that many of the applications are still ideas, and

we are still waiting for the better technology to be able to test and realize them. Even though prototypes are invented for some, most of them are still far away from mass production and commercialization.

1.2 Theory

We start with the elegant macroscopic Maxwell's equations, which summarize the basic electromagnetic phenomena and can be found in many textbooks [Jackson, 1999; Kong, 2005]

Gauss's law $\nabla \cdot \mathbf{D} = \rho$, (1.1.1)

Gauss's law for magnetism $\nabla \cdot \mathbf{B} = 0$, (1.1.2)

Faraday's law $\nabla \times \mathbf{E} + \frac{\partial \mathbf{B}}{\partial t} = 0$, (1.1.3)

Ampere's law $\nabla \times \mathbf{H} - \frac{\partial \mathbf{D}}{\partial t} = \mathbf{J}$. (1.1.4)

Here $\mathbf{D}$ is the electric displacement, ρ the free charge density, $\mathbf{B}$ the magnetic induction, $\mathbf{E}$ the electric field, $\mathbf{H}$ the magnetic field, and $\mathbf{J}$ is the free charge current density. If we have the electric and magnetic properties of the material, which will provide relations between $\mathbf{D}$ and $\mathbf{E}$, and between $\mathbf{B}$ and $\mathbf{H}$, then we can solve the Maxwell equations for a given problem.

1.2.1 Solutions of Maxwell's equations in a uniform medium

We can analytically solve Maxwell's equation, with a proper material-electromagnetic property model, to achieve a more fundamental understanding of the bulk plasmon. We start with material properties. We assume that $\mathbf{E}$ is small enough for us to only consider the linear excitation of $\mathbf{D}$. We consider non-chiral material, i.e. electric displacement $\mathbf{D}$ depends on electric field $\mathbf{E}$ not magnetic induction $\mathbf{B}$. We also consider an isotropic material, which means the dielectric function is not a tensor. Then the general form of the material electronic response relation is:

$$\mathbf{D}(\mathbf{r},t) = \int d\mathbf{r}' \int_{-\infty}^{+\infty} dt' \varepsilon_0 \hat{\varepsilon}(\mathbf{r},\mathbf{r}';t',t)\mathbf{E}(\mathbf{r}';t'), \tag{1.2.1}$$

where $\hat{\varepsilon} = \frac{1}{\sqrt{2\pi}}\varepsilon$, and ε is for relative permittivity, and ε_0 is the vacuum permittivity.

We first assume the response is local,

$$\hat{\varepsilon}(\mathbf{r},\mathbf{r}';t,t') \to \delta(\mathbf{r}-\mathbf{r}')\hat{\varepsilon}(\mathbf{r}';t,t'), \tag{1.2.2}$$

and equation (1.2.1) becomes

$$\mathbf{D}(\mathbf{r},t) = \int_{-\infty}^{+\infty} dt' \varepsilon_0 \hat{\varepsilon}(\mathbf{r},t,t')\mathbf{E}(\mathbf{r};t'). \tag{1.2.3}$$

We assume ε to be constant in space. If there is non-uniformity, it is approximated by uniform regions with constant ε, so we have

$$\hat{\varepsilon}(\mathbf{r};t,t') = \hat{\varepsilon}(t,t') . \tag{1.2.4}$$

Now equation (1.2.3) becomes

$$\mathbf{D}(\mathbf{r},t) = \int_{-\infty}^{+\infty} dt' \varepsilon_0 \hat{\varepsilon}(t,t') \mathbf{E}(\mathbf{r},t') . \tag{1.2.5}$$

We also assume translational invariance in time, i.e. there is no absolute time: an experiment can begin anytime, and the results will be same. Then we have

$$\mathbf{D}(\mathbf{r},t) = \int_{-\infty}^{+\infty} dt' \varepsilon_0 \hat{\varepsilon}(t'-t) \mathbf{E}(\mathbf{r},t') = \frac{1}{\sqrt{2\pi}} \int_{-\infty}^{+\infty} dt' \varepsilon_0 \varepsilon(t'-t) \mathbf{E}(\mathbf{r},t') . \tag{1.2.6}$$

Note that the t' integral is unrestricted, but the physics is, since the response must be causal, i.e. it cannot depend on future impulse. This requires that $\varepsilon(t-t')$ vanishes for $t' > t$. Since we assume linear responses, Maxwell's equations are linear. We can use linear algebra, which involves choosing a complete set of functions forming a base set in the Hilbert space. Maxwell's equations can be solved for these functions, and then for an arbitrary impulse, the complete solution is given by the linear superposition of these functions. Here we choose harmonic functions $e^{-i\omega t}$, which are known to form a complete set in Hilbert space. So we can write

$$\begin{aligned} \mathbf{D}(\mathbf{r},t) &= \mathbf{D}(\mathbf{r},\omega) e^{-i\omega t} \\ \mathbf{E}(\mathbf{r},t) &= \mathbf{E}(\mathbf{r},\omega) e^{-i\omega t} \end{aligned} , \tag{1.2.7}$$

and equation (1.2.6) now becomes, for each and every ω,

$$\mathbf{D}(\mathbf{r},\omega) e^{-i\omega t} = \frac{1}{\sqrt{2\pi}} \int_{-\infty}^{+\infty} dt' \varepsilon_0 \varepsilon(t'-t) \mathbf{E}(\mathbf{r},\omega) e^{-i\omega t'} .$$

which leads to

$$\mathbf{D}(\mathbf{r},\omega) = \varepsilon_0 \varepsilon(\omega)\mathbf{E}(\mathbf{r},\omega) \ , \tag{1.2.8}$$

where

$$\varepsilon(\mathbf{r},\omega)\frac{1}{\sqrt{2\pi}}\int_{-\infty}^{+\infty} dt\varepsilon(t)e^{-i\omega(t)} \ . \tag{1.2.9}$$

Note: We can follow the same procedure for the magnetic response relation and get

$$\mathbf{B}(\mathbf{r},\omega) = \mu_0 \mu(\omega)\mathbf{H}(\mathbf{r},\omega) \ , \tag{1.2.10}$$

where μ is the relative permeability and μ_0 is the vacuum permeability.

When there is no free charge or current sources, $\rho = 0$ and $\mathbf{J} = 0$. The third of Maxwell's equations (1.1.3) becomes

$$\begin{aligned} &\nabla \times [\mathbf{E}(\mathbf{r},\omega)e^{-i\omega t}] + \frac{\partial}{\partial t}[\mathbf{B}(\mathbf{r},\omega)e^{-i\omega t}] = 0 \\ &[\nabla \times \mathbf{E}(\mathbf{r},\omega) - i\omega\mu_0\mu(\omega)\mathbf{H}(\mathbf{r},\omega)]e^{-i\omega t} = 0 \end{aligned} \ .$$

Now we have

$$\nabla \times \mathbf{E}(\mathbf{r},\omega) - i\omega\mathbf{B}(\mathbf{r},\omega) = 0 \, . \tag{1.3.1}$$

Following the same procedure with the fourth of Maxwell's equations (1.1.4), we get

$$\nabla \times \mathbf{H}(\mathbf{r},\omega) + i\omega\mathbf{D}(\mathbf{r},\omega) = 0 \, . \tag{1.3.2}$$

By applying the operator $\nabla\times$ to both sides of the equation (1.3.1), we get

$$\begin{aligned} &\nabla \times (\nabla \times \mathbf{E}(\mathbf{r},\omega) + i\omega\mathbf{B}(\mathbf{r},\omega)) = 0 \\ &\nabla \cdot (\nabla \cdot \mathbf{E}(\mathbf{r},\omega)) - \nabla^2\mathbf{E}(\mathbf{r},\omega) + i\omega\mu_0\mu(\omega)(\nabla \times \mathbf{H}(\mathbf{r},\omega)) = 0 \end{aligned} \ .$$

By inserting Eq. (1.3.2) into above equation, and using Eq. (1.2.7), we get

$$\nabla \cdot (\nabla \cdot \mathbf{E}(\mathbf{r},\omega)) - \nabla^2 \mathbf{E}(\mathbf{r},\omega) - \omega^2 \mu_0 \mu(\omega) \varepsilon_0 \varepsilon(\omega) \mathbf{E}(\mathbf{r},\omega) = 0 . \qquad (1.4.1)$$

Now we also consider the fields being harmonic in space $\mathbf{E}(\mathbf{r},\omega) = \mathbf{E}_0(\omega) e^{i\mathbf{kr}}$, where $\mathbf{k}$ is the wave vector. We consider the medium being uniform in space. If there is non-uniformity, it is approximated by a set of uniform media regions.

$$\begin{aligned}
&\nabla \cdot \mathbf{E}(\mathbf{r},\omega) \\
&= \nabla \cdot \mathbf{E}_0(\omega) e^{i\mathbf{kr}} \\
&= \frac{\partial E_{0x}(\omega) e^{i\mathbf{kr}}}{\partial x} + \frac{\partial E_{0y}(\omega) e^{i\mathbf{kr}}}{\partial y} + \frac{\partial E_{0z}(\omega) e^{i\mathbf{kr}}}{\partial z} \\
&= i\mathbf{k}(\hat{i} E_{0x}(\omega)) e^{i\mathbf{kr}} + i\mathbf{k}(\hat{j} E_{0y}(\omega)) e^{i\mathbf{kr}} + i\mathbf{k}(\hat{k} E_{0z}(\omega)) e^{i\mathbf{kr}} \\
&= i\mathbf{k} \cdot (\mathbf{E}_0(\omega) e^{i\mathbf{kr}}) \\
&= i\mathbf{k} \cdot \mathbf{E}(\mathbf{r},\omega)
\end{aligned}$$

.

Using $\nabla \to i\mathbf{k}$, Equation (1.4.1) becomes

$$\mathbf{k} \cdot (\mathbf{k} \cdot \mathbf{E}(\mathbf{r},\omega)) - k^2 \mathbf{E}(\mathbf{r},\omega) - \mu_0 \mu(\omega) \varepsilon_0 \varepsilon(\omega) \omega^2 \mathbf{E}(\mathbf{r},\omega) = 0 , \qquad (1.4.2)$$

where k is the magnitude of the wave vector $\mathbf{k}$.

Note: The equivalent equation for magnetic field can be achieved by applying $\nabla \times$ both sides of Eq. (1.3.2).

$$\mathbf{k} \cdot (\mathbf{k} \cdot \mathbf{H}(\mathbf{r},\omega)) - k^2 \mathbf{H}(\mathbf{r},\omega) - \mu_0 \mu(\omega) \varepsilon_0 \varepsilon(\omega) \omega^2 \mathbf{H}(\mathbf{r},\omega) = 0 . \qquad (1.4.3)$$

As one can see, the electric field and magnetic field follow exactly the same equations, and so most times we can simply just study one of the equations.

Transverse modes

For the transverse modes, $\mathbf{k}$ is perpendicular to $\mathbf{E}$ and $\mathbf{H}$, in which case $\mathbf{k}\cdot\mathbf{E}=0$.

Equation (1.4.2) becomes

$$k^2\mathbf{E}(\mathbf{r},\omega)-\mu\mu_0\varepsilon\varepsilon_0\mathbf{E}(\mathbf{r},\omega)=0\,.$$

For non-zero fields, we get

$$\omega=(c/\sqrt{\mu\varepsilon})k\,. \qquad (1.5)$$

Here $c=1/\sqrt{\mu_0\varepsilon_0}$ is the speed of light in vacuum.

Longitudinal modes

For the longitudinal modes, i.e. $\mathbf{k}$ is parallel to $\mathbf{E}$, this means $\mathbf{k}\cdot(\mathbf{k}\cdot\mathbf{E})=k^2\mathbf{E}$. Equation (1.4.2) becomes

$$\mu\mu_0\varepsilon\varepsilon_0\mathbf{E}(\mathbf{r},\omega)=0\,,$$

For non zero fields, this leads to two conditions,

$$\varepsilon=0\,, \qquad (1.6.1)$$

and/or

$$\mu=0\,. \qquad (1.6.2)$$

Equation 1.6.1 is for the electric longitudinal bulk plasmon, and Equation 1.6.2 is for the magnetic longitudinal bulk plasmon.

For a case with nonmagnetic material, $\mu=1$, and Equation 1.5 reduces to the well-known dispersion relation of photons in uniform, nonmagnetic media:

$$\omega = \frac{kc}{\sqrt{\varepsilon}} \ . \qquad (1.7)$$

The plasmon dispersion relation depends on materials' properties. In my research, we only work with non-magnetic material, so the permittivity is the physical parameter that we primarily work with. It has been shown that the classic Drude model works very well for alkali metals with very low losses, and has the form

$$\varepsilon(\omega) = 1 - \frac{\omega_p^2}{\omega^2} \ , \qquad (1.8)$$

where ω_p is the plasma frequency.

Inserting Eq (1.8) into (1.7), one can get the dispersion for the transverse bulk plasmon mode,

$$\omega^2 = \omega_p^2 + c^2 k^2 . \qquad (1.9)$$

The transverse mode can propagate through the medium, and it is shown as the solid line in Fig. 1.1. It is clear that the spectrum has a propagation gap from 0 to ω_p, where no modes can propagate through the medium. In the vacuum, $\varepsilon(\omega) = 1$, the dispersion relation becomes $\omega = ck$. This is also known as the light line and is shown as the dashed line in Fig. 1.1. As mentioned before, longitudinal bulk plasmon mode is also allowed from Maxwell's equations, with $\varepsilon = 0$ leading to $\omega = \omega_p$. This longitudinal mode is shown as the dot-dashed line in Fig. 1.1.

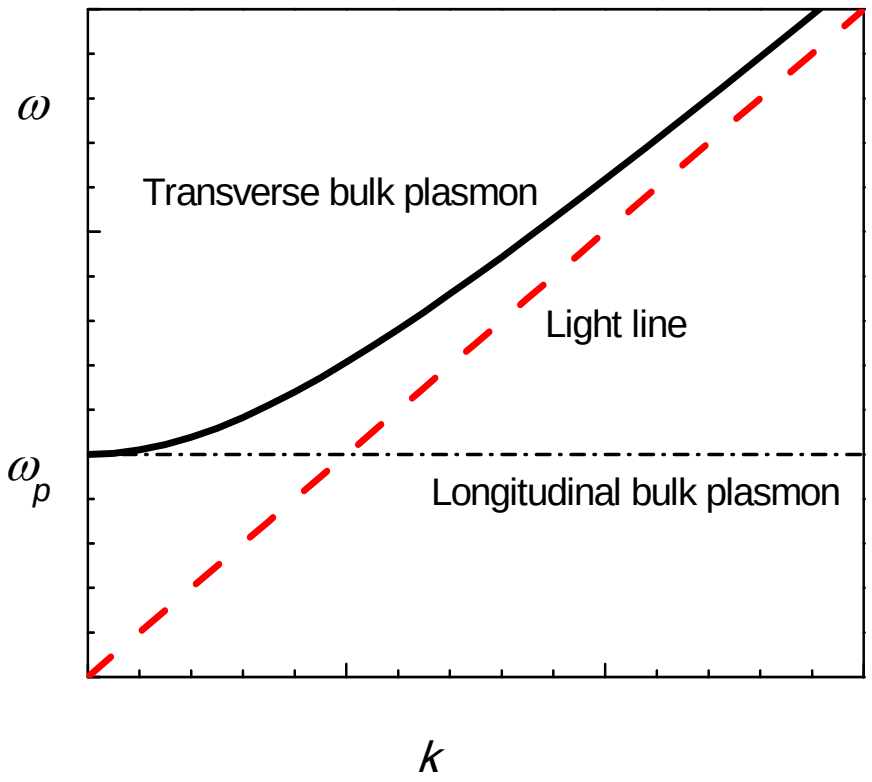

Fig. 1.1 Dispersion relation of a metal (schematic). Solid line: dispersion of the transverse bulk plasmon. Dashed line: photon line in vacuum. Dot-dashed line: dispersion of the longitudinal bulk plasmon.

1.2.2 Surface Plasmons

Surface plasmons, the propagation of coupled electromagnetic-charge waves along an interface, are generated when there is an interface between two media, often between a

metal and a dielectric material. Let us consider an ideal interface (an abrupt flat surface) at $z = 0$ between two non-magnetic materials with dielectric functions $\varepsilon_1(\omega)$ for $z < 0$, and $\varepsilon_2(\omega)$ for $z > 0$, as shown in Fig. 1.2. We consider p-polarized waves, i.e. the electric field is parallel to the incidence plane, which is formed by the incident light ray and the normal line at the point the incident light ray hits the surface.

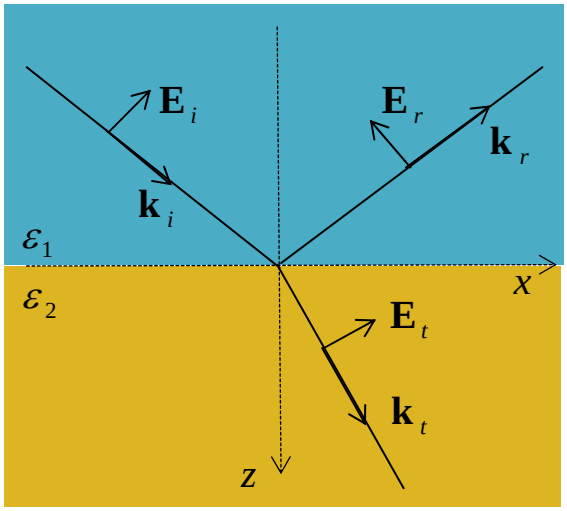

Fig. 1.2 Electromagnetic waves (p-polarized) transmit and reflect on the surface. The two materials have relative dielectric functions $\varepsilon_1(\omega)$ for $z < 0$, and $\varepsilon_2(\omega)$ for $z > 0$. The wave vectors and electric fields are shown for incident, reflected and transmitted waves.

We will not write (ω) for now, and it will come back explicitly a little later. As shown in Fig. 1.2, we consider a transverse wave that is p-polarized. We have

$$\begin{aligned} D_{z1} &= \varepsilon_0 \varepsilon_1 E_{iz} + \varepsilon_0 \varepsilon_1 E_{rz} \\ D_{z2} &= \varepsilon_0 \varepsilon_2 E_{tz} \end{aligned}, \qquad (1.11.1)$$

and

$$\begin{aligned} E_{x1} &= E_{ix} + E_{rx} \\ E_{x2} &= E_{tx} \end{aligned} . \qquad (1.11.2)$$

On the surface, the boundary conditions require the parallel components of the electric field **E** and perpendicular component of electric displacement **D** to be continuous at the interface [Jackson, 1998], this means

$$\begin{aligned} D_{z1} &= D_{z2} \\ E_{x2} &= E_{x2} \end{aligned} . \qquad (1.11.3)$$

Insert Eq. (1.11.1) and (1.11.2) to (1.11.3), we have

$$\begin{aligned} \varepsilon_1 E_{iz} + \varepsilon_1 E_{rz} &= \varepsilon_2 E_{tz} \\ E_{ix} + E_{rx} &= E_{tx} \end{aligned} . \qquad (1.11.4)$$

For transverse waves, the wave vector and electric field are related by $\mathbf{k} \cdot \mathbf{E} = \mathbf{0}$, or

$$\begin{aligned} k_{ix} E_{ix} + k_{iz} E_{iz} &= 0 \\ k_{rx} E_{rx} + k_{rz} E_{rz} &= 0 \\ k_{tx} E_{tx} + k_{tz} E_{tz} &= 0 \end{aligned} . \qquad (1.11.5)$$

Keeping in mind that

$$\begin{aligned} k_{ix} &= k_{rx} = k_{tx} = k_x \\ k_{iz} &= -k_{rz} = k_{1z} \end{aligned} , \qquad (1.11.6)$$

and also writing E_{tz} as E_{2z}, and k_{tz} as k_{2z}, Eqs. (1.11.5) become,

$$\begin{aligned} k_x E_{ix} + k_{1z} E_{iz} = 0 &\Rightarrow E_{ix} = -k_{1z} E_{iz} / k_x \\ k_x E_{rx} - k_{1z} E_{rz} = 0 &\Rightarrow E_{rx} = k_{1z} E_{rz} / k_x \\ k_x E_{tx} + k_{2z} E_{2z} = 0 &\Rightarrow E_{tx} = -k_{2z} E_{2z} / k_x \end{aligned} . \qquad (1.11.7)$$

By inserting Eq. (1.11.7) into the second equation in Eq. (1.11.4), it is seen that there is no solution for $k_x = 0$. For non-zero k_x, Eq. (1.11.4) becomes

$$\begin{aligned} \varepsilon_1 E_{iz} + \varepsilon_1 E_{rz} &= \varepsilon_2 E_{2z} \\ k_{1z} E_{iz} - k_{1z} E_{rz} &= k_{2z} E_{2z} \end{aligned} . \tag{1.11.8}$$

We define the reflection and transmission coefficient as

$$\begin{aligned} r &= E_{rz} / E_{iz} \\ t &= E_{tz} / E_{iz} \end{aligned} . \tag{1.12.1}$$

Dividing both equations in Eq. (1.11.8), and using definition (1.12.1), we have

$$\begin{aligned} \varepsilon_1 + \varepsilon_1 r &= \varepsilon_2 t \\ k_{1z} - k_{1z} r &= k_{2z} t \end{aligned} . \tag{1.12.2}$$

Now solving for r and t, we find

$$\begin{aligned} t &= \frac{\varepsilon_2 k_{1z} - \varepsilon_1 k_{2z}}{\varepsilon_2 k_{1z} + \varepsilon_1 k_{2z}} \\ r &= \frac{2\varepsilon_1 k_{1z}}{\varepsilon_2 k_{1z} + \varepsilon_1 k_{2z}} \end{aligned} . \tag{1.12.3}$$

The system has an eigenmode when the reflection coefficient and/or transmission coefficient diverge. From the equations (1.12.3), t and r diverge when

$$\varepsilon_2 k_{1z} + \varepsilon_1 k_{2z} = 0 . \tag{1.12.4}$$

The wave vector components satisfy the following relations: $k_x^2 + k_{jz}^2 = \varepsilon_j k^2$;

$k = \frac{2\pi}{\lambda} = \frac{\omega}{c}$ is the vacuum wavelength and $j = 1,2$ for the two media. Plugging the

expression for k_{jz} into Eq. (1.12.4), the resulting surface plasmon dispersion takes a more familiar form,

$$k_x = k\sqrt{\frac{\varepsilon_1\varepsilon_2}{\varepsilon_1+\varepsilon_2}} = \frac{\omega}{c}\sqrt{\frac{\varepsilon_1\varepsilon_2}{\varepsilon_1+\varepsilon_2}}, \qquad (1.13.1)$$

or if one medium is vacuum,

$$k_x = \frac{\omega}{c}\sqrt{\frac{\varepsilon_2}{\varepsilon_2+1}}. \qquad (1.13.2)$$

We can first get the asymptotic value of the surface plasma frequency in the non-retarded limit ($c \to \infty$) by letting

$$\varepsilon_2 + 1 = 0. \qquad (1.13.3)$$

Then we insert the classic Drude model for prefect metal: the dielectric function eq. (1.8) to Eq. (1.13.3); we can get the well-known formula for the surface plasmon frequency

$$\omega_{sp} = \omega_p / \sqrt{2}\ . \qquad (1.13.4)$$

We can also get the dispersion relation of SPs by inserting eq. (1.8) to eq. (1.13.2):

$$k_x = \frac{\omega}{c}\sqrt{\frac{\omega^2-\omega_p^2}{2\omega^2-\omega_p^2}}. \qquad (1.13.5)$$

Figure 1.3 shows in solid lines the two branches of SP's, which are solutions to equation (1.13.5). The upper branch represents the dispersion of light in the metal, and it has a cut-off frequency at the bulk plasmon frequency. This mode is not stable, and it will quickly dissipate into light as shown in the plot. The "light line (x-direction)" represents the light propagating in vacuum along the x direction, and all other light-modes have

smaller k_x for a given ω. There are an infinite number of light lines to the left of the "light line (x-direction)" and going through the origin, each corresponds to a light wave propagating at a different angle to the surface. For all the points on the surface plasmon upper branch, we can find a light line crossing at that point, the crossing representing simultaneous conservation of energy $\hbar\omega$ and momentum $\hbar k_x$, so that the surface plasmon can dissipate into light propagating in vacuum.

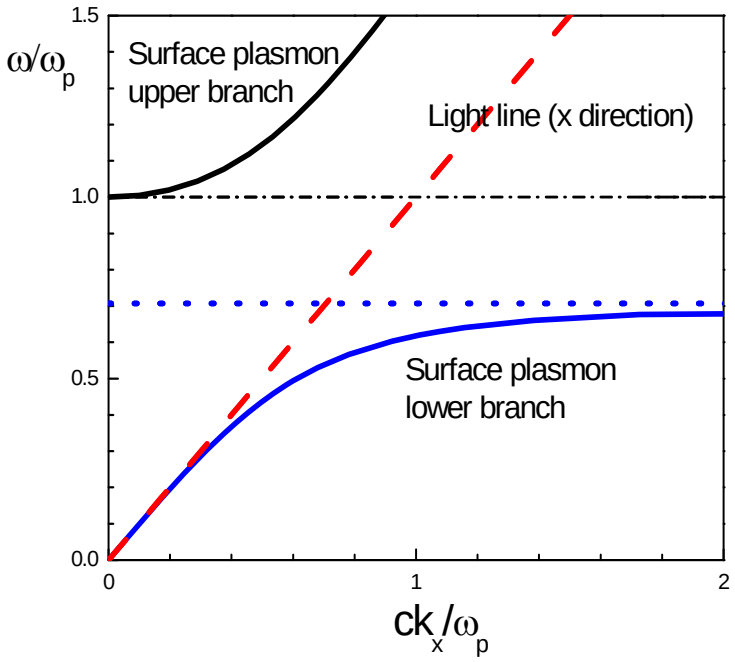

Fig. 1.3 Normalized frequency vs. the normalized in-plane wave vector for the surface plasmon (solid lines) (schematic). The dispersion relation for the x direction light line is shown as the dashed line, and for the longitudinal bulk plasmon ω_p the dash-dotted line. The surface plasmon frequency ω_{sp} is shown as the dotted line.

Since all light lines reside to the left of the light line (x-direction), the simultaneous conservation of energy and momentum cannot happen to the right of the "light line (x-direction)", thus the lower branch represents the stable SP's. They can exist on the interface and propagate. To excite a surface plasmon, extra momentum needs to be provided by a rough surface or some grating [Raether, 1988; Maier, 2007], for example. The lower branch approaches the surface plasmon frequency, $\omega_p / \sqrt{2}$, for large k_x.

Surface plasmons described in the Fig. 1.3 is also electric surface plasmons. If we consider an interface between vacuum and a magnetic medium, equation 1.13.1 will be [Wang, Plummer &Kempa, 2011].

$$k_x = \frac{\omega}{c}\sqrt{\frac{\varepsilon(\varepsilon-\mu)}{\varepsilon^2-1}}\,. \qquad (1.14)$$

If we consider the s-polarized wave, i.e. the electric field is perpendicular to the incidence plane, solutions on an interface between vacuum and a magnetic medium $\mu \neq 1$, we will get the dispersion for magnetic surface plasmon dispersion (equivalent of equation 1.14) [Wang, Plummer & Kempa, 2011].

$$k = \frac{\omega}{c}\sqrt{\frac{\mu(\mu-\varepsilon)}{\mu^2-1}}\,. \qquad (1.15)$$

The non-retarded limit for the magnetic surface plasma waves frequency can be derived from $\mu + 1 = 0$.

1.2.3 Localized surface plasma waves

The localized surface plasmon (LSP) is the other fundamental form of surface plasmons, and it is electron charge density oscillations that are localized on the surface of nanoparticles. These are standing surface plasma waves. A very important property of LSP's is that they have their own characteristic resonant frequencies. The interaction of light and small metal particles can be viewed as a boundary problem that can be solved using Maxwell's equations. Gustav Mie, though not the first to examine this problem, was however the first to formulate this problem beautifully as an electromagnetic scattering problem [1908]. Mie theory is able to treat the scattering problem of spherical particles of various sizes.

For a particle of radius $a \sim \lambda$, according to Mie Theory, the localized surface plasmon of spherical metal nanoparticles can be circumferentially quantized. Figure 1.4 illustrates an easy approximate way to understand this concept. When light hits the metal nanosphere, the electrons are momentarily shaken out of the surface, the Coulomb force will then pull them back and create surface electromagnetic waves (surface plasmon). The circumference is an integer number of the wavelength of the surface plasmon, which can also be expressed as $\pi d = l\lambda = l\frac{2\pi}{k}$. For a particle of certain diameter d, this equation defines the wave vector k for the resonant SP's (LSP's), and the corresponding frequency can be obtained approximately from the dispersion relation shown in Fig 1.3,

with $k = k_x$. It is the characteristic resonant frequency that gives the silver/gold particles their different beautiful colors depending on their sizes.

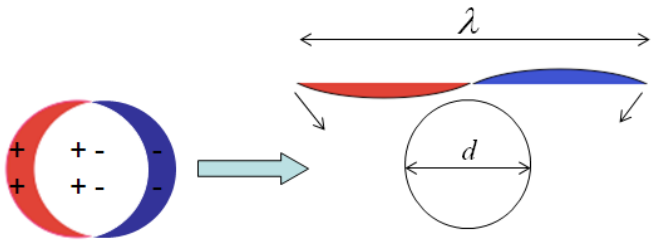

Fig. 1.4 Illustration of Mie's theory of circumferential quantization for metal sphere

For a particle of radius $a << \lambda$, one assumes that the external field is uniform, which is a quasi-static approximation. Mie's theory is analyzed and gives the resonant condition [Bohren & Huffman, 1983; Kreibig & Vollmer, 1995]:

$$\varepsilon + 2\varepsilon_m = 0. \qquad (1.16)$$

Considering a Drude metal sphere in vacuum, we use $\varepsilon_m = 1$, and substitute in the Drude model Eq (1.8) for ε, and we find the Mie frequency for nanoparticles

$$\omega_{Mie} = \omega_p / \sqrt{3}. \qquad (1.17)$$

Even though it is not studied as extensively as the propagating SP's, recent theoretical and experimental work suggests that LSP's might contribute to the enhanced transmission [Maier, 2007], and play a role in sharp metal tips and some nanoantennas [Bozhevolnyi& Lozovski, 2002; Bozhevolnyi et al., 2006].

Chapter 2

Methods

Two main methods to solve Maxwell's equations are used in this research: One is the traditional analytical method, and the other is the computational/calculation method, also referred to as the simulation. The given projects were first approached through the analytic method to solve Maxwell's equations given the boundary conditions. In the simplest case, the TEM mode in the nanocoaxial cable, a numerical solution has been found, and agrees well with the simulation results. As shown later, it is rather complicated, and in some cases almost impossible, to get sensible solutions for higher-order mode and/or complicated structures. A simulation method will be introduced to deal with the more complicated cases, which also result in sensible results.

2.1 Analytical method

The conventional analytical methods to solve Maxwell's equations have been used to solve simple homogeneous problems [Jackson, 1999; Shen, 1998; Yuan et al, 2000]. The analytical method can give exact answers to simple problems, such as homogeneous media in 1, 2 and 3 dimensions [Carlos, 2005], and multilayered solid structures [Caviglia & Morro, 2000]. Many examples, including these mentioned in the above references can be found to illustrate the analytic method. In this Chapter, I have solved for the electromagnetic wave propagation in a nanocoaxial waveguide. These results will be useful for the wire waveguide as well. An improved analytical method will be used to solve for the one-plasmon mode of the nanocoaxial cable by matching solutions of Maxwell's equations in cylindrical coordinates across the nanocoaxial interfaces. The geometry of the coaxial waveguide is shown schematically in Fig. 2.1. The metal core is a solid cylinder with radius a. The outer conductor is a hollow metallic cylinder with inner radius b, and outer radius c. Since we are interested here only in internally-guided modes, i.e. modes with fields localized between the core and the outer conductor, the outer conductor can be assumed to be infinitely thick (i.e. $c \to \infty$). This is a good approximation for any coaxial waveguide with an outer conductor much thicker than the field penetration depth of these internally guided modes.

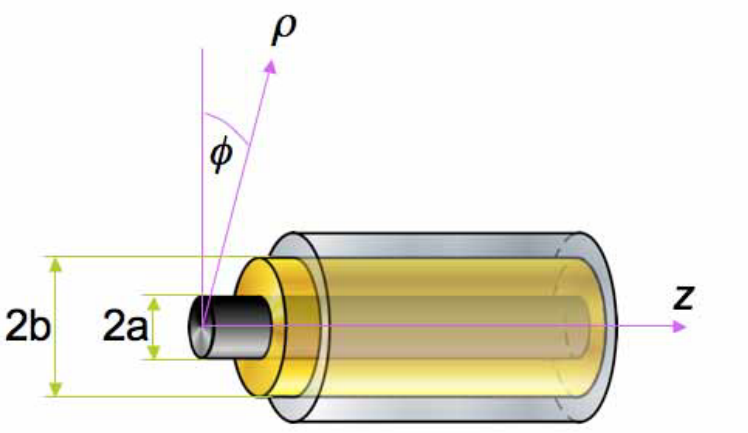

Fig. 2.1 Geometry of the nanocoaxial cable. Metal core has radius of a; Outer conductor shell has inner radius b and outer radius c. Dielectric cladding is in between radius a and b.

As shown previously, solving Maxwell's equations leads to equation (1.4.1), and for transverse waves and materials with $\mu(\omega) = 1$, it yields

$$\nabla^2 \mathbf{E}(\mathbf{r}, \omega) + \varepsilon(\omega) k_0^2 \mathbf{E}(\mathbf{r}, \omega) = 0 . \qquad (2.1)$$

The dielectric function takes the value $\varepsilon = \varepsilon_1$ inside the core and it changes to ε_2 in the cladding, and then changes to ε_3 in the outside material. $k_0 = \omega\sqrt{\mu_0 \varepsilon_0} = \omega / c$ is the wave vector in vacuum.

It is obviously helpful to work in a cylindrical coordinate system with ρ, ϕ, z. We choose, as is common, E_z and H_z as independent components. The equation for E_z in cylindrical coordinates becomes:

$$\frac{\partial^2 E_z}{\partial \rho^2} + \frac{1}{\rho}\frac{\partial E_z}{\partial \rho} + \frac{1}{\rho^2}\frac{\partial^2 E_z}{\partial \phi^2} + \frac{\partial^2 E_z}{\partial z^2} + \varepsilon k_0^2 E_z = 0. \qquad (2.2)$$

while H_z satisfies the same equation as above.

We use the method of separation of variables, and let $E_z(\rho, \phi, z) = F(\rho)\Phi(\phi)Z(z)$. We then obtain three ordinary differential equations (ODE's):

$$\begin{cases} \dfrac{d^2 Z}{dz^2} + \beta^2 Z = 0 \\ \dfrac{d^2 \Phi}{d\phi^2} + m^2 \Phi = 0 \\ \dfrac{d^2 F}{d\rho^2} + \dfrac{1}{\rho}\dfrac{dF}{d\rho} + (\varepsilon k_0^2 - \beta^2 - \dfrac{m^2}{\rho^2})F = 0 \rightarrow \textit{BesselFunc tion} \end{cases}, \qquad (2.3)$$

where β and m are two constants (m must be an integer).

The first two equations in (2.3) can be solved easily to obtain

$Z(z) = \exp(i\beta z)$ and $\Phi(\phi) = \exp(im\phi)$. While $F(\rho)$ satisfies the Bessel equation.

For simpler problems, such as a one-cylinder problem, Takahara et al. (1997) have given solutions with proper Bessel functions in different regions. Inspired by their paper, we also divide the space into three regions according to their refraction index number. We can write the general solutions of the electric field and magnetic field (by following the same recipe) of the above ODE's:

$$E_z = \begin{cases} AI_n(p\rho)\exp(im\phi)\exp(i\beta z) & \rho \le a, \varepsilon_1 \\ CI_n(q\rho)\exp(im\phi)\exp(i\beta z) + EK_n(q\rho)\exp(im\phi)\exp(i\beta z) & a < \rho \le b, \varepsilon_2 \\ GK_n(r\rho)\exp(im\phi)\exp(i\beta z) & \rho > b, \varepsilon_3 \end{cases}$$

$$H_z = \begin{cases} BI_n(p\rho)\exp(im\phi)\exp(i\beta z) & \rho \le a, \varepsilon_1 \\ DI_n(q\rho)\exp(im\phi)\exp(i\beta z) + FK_n(q\rho)\exp(im\phi)\exp(i\beta z) & a < \rho \le b, \varepsilon_2 \\ HK_n(r\rho)\exp(im\phi)\exp(i\beta z) & \rho > b, \varepsilon_3 \end{cases}$$

Here I_n and K_n are the modified Bessel Function of the first and second kinds. A, B, C, D, E, F, G, and H are some constants. Also p, q and r are given by $p^2 = \varepsilon_1 k_0^2 - \beta^2$, $q^2 = \varepsilon_2 k_0^2 - \beta^2$, $r^2 = \varepsilon_3 k_0^2 - \beta^2$.

From the relation $E_\phi = \frac{i}{p^2}[\frac{\beta}{\rho}\frac{\partial E_z}{\partial \phi} - \mu_0 \omega \frac{\partial H_z}{\partial \rho}]$, we can get:

$$E_\phi = \begin{cases} \frac{i}{p^2}(\frac{\beta}{\rho} imAI_n(p\rho) - \mu_0 \omega pBI_n'(p\rho))\exp(im\phi)\exp(i\beta z) & \rho \le a, \varepsilon_1 \\ (\frac{i}{q^2}[(\frac{\beta}{\rho} imCI_n(q\rho) + \frac{\beta}{\rho} imEK_n(q\rho))\exp(im\phi)\exp(i\beta z) & a < \rho \le b, \varepsilon_2 \\ -(\mu_0 \omega qDI_n'(q\rho) + \mu_0 \omega qFK_n'(q\rho))\exp(im\phi)\exp(i\beta z)]) & \\ \frac{i}{r^2}(\frac{\beta}{\rho} imGK_n(p\rho) - \mu_0 \omega rHK_n'(r\rho))\exp(im\phi)\exp(i\beta z) & \rho > b, \varepsilon_3 \end{cases}$$

Also from $H_\phi = \frac{i}{p^2}[\frac{\beta}{\rho}\frac{\partial H_z}{\partial \phi} + \varepsilon_0 n^2 \omega \frac{\partial E_z}{\partial \rho}]$, we get:

$$H_\phi = \begin{cases} \dfrac{i}{p^2}\left(\dfrac{\beta}{\rho} imBI_n(p\rho) + \varepsilon_0 n_1^2 \omega pAI_n'(p\rho)\right)\exp(im\phi)\exp(i\beta z) & \rho \le a, \varepsilon_1 \\ \dfrac{i}{q^2}\left[\left(\dfrac{\beta}{\rho} imDI_n(q\rho) + \dfrac{\beta}{\rho} imFK_n(q\rho)\right)\exp(im\phi)\exp(i\beta z)\right. & a < \rho \le b, \varepsilon_2 \\ \left. + \left(\varepsilon_0 n_2^2 \omega qCI_n'(q\rho) + \varepsilon_0 n_2^2 \omega qEK_n'(q\rho)\right)\exp(im\phi)\exp(i\beta z)\right] & \\ \dfrac{i}{r^2}\left(\dfrac{\beta}{\rho} imHK_n(p\rho) + \varepsilon_0 n_3^2 \omega rGK_n'(r\rho)\right)\exp(im\phi)\exp(i\beta z) & \rho > b, \varepsilon_3 \end{cases}$$

The eight boundary conditions are listed below as,

(1) E_z continues at $\rho = a$, (2) E_z continues at $\rho = b$, (3) H_z continues at $\rho = a$

(4) H_z continues at $\rho = b$, (5) E_ϕ continues at $\rho = a$, (6) E_ϕ continues at $\rho = b$

(7) H_ϕ continues at $\rho = a$, (8) H_ϕ continues at $\rho = b$

We then get the following eight equations, written in the format of a matrix:

$$S \times \begin{pmatrix} A \\ B \\ C \\ D \\ E \\ F \\ G \\ H \end{pmatrix} = \begin{pmatrix} s_{11} & s_{12} & s_{13} & s_{14} & s_{15} & s_{16} & s_{17} & s_{18} \\ s_{21} & s_{22} & s_{23} & s_{24} & s_{25} & s_{26} & s_{27} & s_{28} \\ s_{31} & s_{32} & s_{33} & s_{34} & s_{35} & s_{36} & s_{37} & s_{38} \\ s_{41} & s_{42} & s_{43} & s_{44} & s_{45} & s_{46} & s_{47} & s_{48} \\ s_{51} & s_{52} & s_{53} & s_{54} & s_{55} & s_{56} & s_{57} & s_{58} \\ s_{61} & s_{62} & s_{63} & s_{64} & s_{65} & s_{66} & s_{67} & s_{68} \\ s_{71} & s_{72} & s_{73} & s_{74} & s_{75} & s_{76} & s_{77} & s_{78} \\ s_{81} & s_{82} & s_{83} & s_{84} & s_{85} & s_{86} & s_{87} & s_{88} \end{pmatrix} \times \begin{pmatrix} A \\ B \\ C \\ D \\ E \\ F \\ G \\ H \end{pmatrix} = 0, \qquad (2.4)$$

with $s_{11} = I_n(pa), s_{12} = 0, s_{13} = -I_n(qb), s_{14} = 0, s_{15} = -K_n(qa), s_{16} = 0, s_{17} = 0, s_{18} = 0$,

$s_{21} = 0, s_{22} = 0, s_{23} = I_n(qb), s_{24} = 0, s_{25} = K_n(qb), s_{26} = 0, s_{27} = -K_n(rb), s_{28} = 0$,

$s_{31} = 0, s_{32} = I_n(pa), s_{33} = 0, s_{34} = -I_n(qa), s_{35} = 0, s_{36} = -K_n(qa), s_{37} = 0, s_{38} = 0$,

$s_{41} = 0, s_{42} = 0, s_{43} = 0, s_{44} = I_n(qb), s_{45} = 0, s_{46} = K_n(qb), s_{47} = 0, s_{48} = -K_n(rb)$,

$s_{51} = \frac{im\beta}{p^2 a} I_m(pa), s_{52} = -\frac{\mu_0 \omega p}{p^2} I_m'(pa), s_{53} = -\frac{im\beta}{q^2 a} I_m(qa), s_{54} = \frac{\mu_0 \omega q}{q^2} I_m'(qa)$,

$s_{55} = -\frac{im\beta}{q^2 a} K_n(qa), s_{56} = \frac{\mu_0 \omega q}{q^2} K_n'(qa), s_{57} = 0, s_{58} = 0$,

$s_{61} = 0, s_{62} = 0, s_{63} = \frac{im\beta}{q^2 b} I_n(qb), s_{64} = -\frac{\mu_0 \omega q}{q^2} I_n'(qb)$,

$s_{65} = \frac{im\beta}{q^2 b} K_n(qb), s_{66} = -\frac{\mu_0 \omega q}{q^2} K_n'(qb), s_{67} = -\frac{im\beta}{r^2 b} K_n(rb), s_{68} = \frac{\mu_0 \omega r}{r^2} K_n'(rb)$,

$s_{71} = \frac{\varepsilon_0 n_1^2 \omega p}{p^2} I_n'(pa), s_{72} = \frac{im\beta}{p^2 a} I_n(pa), s_{73} = -\frac{\varepsilon_0 n_2^2 \omega q}{q^2} I_n'(qa), s_{74} = -\frac{im\beta}{q^2 a} I_n(qa)$,

$s_{75} = -\frac{\varepsilon_0 n_2^2 \omega q}{q^2} K_n'(qa), s_{76} = -\frac{im\beta}{q^2 a} K_n(qa), s_{77} = 0, s_{78} = 0$,

$s_{81} = 0, s_{82} = 0, s_{83} = \frac{\varepsilon_0 n_2^2 \omega q}{q^2} I_n'(qb), s_{84} = \frac{im\beta}{q^2 b} I_n(qb)$,

$s_{85} = \frac{\varepsilon_0 n_2^2 \omega q}{q^2} K_n'(qb), s_{86} = \frac{im\beta}{q^2 b} K_n(qb), s_{87} = -\frac{\varepsilon_0 n_3^2 \omega r}{r^2} K_n'(rb), s_{88} = -\frac{im\beta}{r^2 b} K_n(rb)$.

Setting the determinant of matrix S equal to zero, i.e. $\det|S| = 0$, gives the dispersion relation. For the TEM mode, $n = 0$, and the relation becomes the following equation after some simplifications,

$$0 = \left(K_0(qb)\frac{I_0(qa)}{I_0(qb)}\frac{\varepsilon_1}{p}\frac{I_1(pa)}{I_0(pa)} - \frac{\varepsilon_2}{q}K_1(qa) - K_0(qa)\frac{\varepsilon_1}{p}\frac{I_1(pa)}{I_0(pa)} - K_0(qb)\frac{\varepsilon_2}{q}\frac{I_1(qa)}{I_0(qb)} \right)$$
$$\times \left(-\frac{\varepsilon_3}{r}K_1(rb) - K_0(rb)\frac{\varepsilon_2}{q}\frac{I_1(qb)}{I_0(qb)} \right)$$
$$- \left(K_0(rb)\frac{\varepsilon_2}{q}\frac{I_1(qa)}{I_0(qb)} - K_0(rb)\frac{I_0(qa)}{I_0(qb)}\frac{\varepsilon_1}{p}\frac{I_1(pa)}{I_0(pa)} \right) \left(\frac{\varepsilon_2}{q}K_1(qb) + K_0(qb)\frac{\varepsilon_2}{q}\frac{I_1(qb)}{I_0(qb)} \right) . \quad (2.5.1)$$

Furthermore, we assume that both conductors are made of the same nonmagnetic metal described by the Drude dielectric function,

$$\varepsilon_1 = \varepsilon_3 = \varepsilon_\infty - \frac{\omega_p^2}{\omega^2 + i\omega\gamma}$$

where ω is the frequency, ω_p is the metal's plasma frequency, γ is the damping parameter, and ε_∞ is the contribution from the "bound" electrons. A dielectric material, with dielectric constant ε_2, fills the space between the conductors. All fields are assumed to be transverse, and $\propto \exp[i(k_z z - \omega t]$, where k_z is the z-component of the wave vector. Each material interface is assumed to be abrupt, with standard boundary conditions used to match the electromagnetic fields.

The dispersion relation equation then becomes

$$\left(K_0(k_2 b)\frac{I_0(k_2 a)}{I_0(k_2 b)}\frac{\varepsilon_1}{k_1}\frac{I_1(k_1 a)}{I_0(k_1 a)} - \frac{\varepsilon_2}{k_2}K_1(k_2 a) - K_0(k_2 a)\frac{\varepsilon_1}{k_1}\frac{I_1(k_1 a)}{I_0(k_1 a)} - K_0(k_2 b)\frac{\varepsilon_2}{k_2}\frac{I_1(k_2 a)}{I_0(k_2 b)} \right)$$
$$\times\left(-\frac{\varepsilon_1}{k_3}K_1(k_3 b) - K_0(k_3 b)\frac{\varepsilon_2}{k_2}\frac{I_1(k_2 b)}{I_0(k_2 b)} \right)$$
$$-\left(K_0(k_3 b)\frac{\varepsilon_2}{k_2}\frac{I_1(k_2 a)}{I_0(k_2 b)} - K_0(k_3 b)\frac{I_0(k_2 a)}{I_0(k_2 b)}\frac{\varepsilon_1}{k_1}\frac{I_1(k_1 a)}{I_0(k_1 a)} \right)\left(\frac{\varepsilon_2}{k_2}K_1(k_2 b) + K_0(k_2 b)\frac{\varepsilon_2}{k_2}\frac{I_1(k_2 a)}{I_0(k_2 b)} \right)$$
$$= F(\omega, k_x) = 0 \quad ,$$

(2.5.2)

here $k_j = \sqrt{k_z^2 - (\omega/c)^2 \varepsilon_j}$, $j = 1,2,3$, and I_n, K_n are the n th ($n = 0,1$) order modified Bessel functions of the first and the second kind, respectively.

Equation 2.6 is the desired dispersion relation for the "TEM-like" mode, the details of which will be discussed in a later chapter. In the limit of $b \to \infty$ (a single electrode transmission line), it reduces to the formula for the "negative dielectric pin" as described in the paper of Takahara et al (1997), as expected

$$\left(-\frac{\varepsilon_2}{k_2}K_1(k_2 a) - K_0(k_2 a)\frac{\varepsilon_1}{k_1}\frac{I_1(k_1 a)}{I_0(k_1 a)} \right) = 0 \,, \qquad (2.6)$$

2.2 Computation/Simulation method

As the studied systems and phenomena become more and more complicated, as the above analysis has already given us an idea of how complicated the analytical method can become for some not-so-complicated structures, it is impossible to use the conventional analytical method to solve the problems. It requires that we use the help of computers to perform simulations for the research involving more complicated structures. There have been a lot of computational methods and software [Hafner, 1999; Hafner, Karkashadze et al, 2004; Smajic & Agio, 2010; Peters, 2010; Taflove, 1995; Toflove & Hagness, 2005] developed and employed to simulate electromagnetics in nanostructures. Some examples include the discrete dipole approximation (DDA) [Yang et al, 1995; Kelly et al, 2001; Kelly et al, 2003], which is particularly powerful for small isolated nanostructures; the multiple multipole method [Hafner, 1990; Hafner 1999], which is very difficult to use; T-matrix methods [Waterman, 1971], which is good for no-loss axially symmetric particles. The Finite-Difference Time-Domain (FDTD) method is one of the most popular numerical methods to solve electromagnetic problems and is discussed in many publications [Choi et al, 1986; Kunz & Luebbers, 1993; Taflove, 1995]. A brief introduction to the FDTD method is given below.

2.2.1 Finite-Difference Time-Domain (FDTD) method

Yee (Yee, 1966) proposed Yee's scheme, which later became the Finite-Difference Time-Domain (FDTD) Method, almost half century ago, and it has been proven to be a simple yet efficient way to solve Maxwell's equation in the time domain. Taflove, collaborating with Brodwin (1975), and later with Dugness [2000, 2005], further developed this method based on Yee's scheme, and the details are discussed in their book "Computational Electrodynamics: The Finite-Difference Time-Domain Method" (1995).

In the FDTD method, both space and time are discrete. Fields are represented differently at the mesh points on the Cartesian grid, as shown in Yee's lattice in Fig 2.2, which is one of the many kinds of Yee's 3d unit cells illustrations. The different electromagnetic field components are not located at the same place, but instead staggered around a grid.

In addition to the fact that they are discrete in space, fields are also evolving at discrete time steps. Given a function f at a discrete point in space and time as

$$f(i\Delta x, j\Delta y, k\Delta z, n\Delta t) = f^{n}_{i,j,k} \quad . \tag{2.7}$$

One example of the expressions is the first partial derivative in space of f in the x direction, at a particular time $t_n = n\Delta t$ [Taflove, 1995]:

$$\frac{\partial f}{\partial x}(i\Delta x, j\Delta y, k\Delta z, n\Delta t) = \frac{f^{n}_{i+1/2,j,k} - f^{n}_{i-1/2,j,k}}{\Delta x} + O[(\Delta x)^2] \quad . \tag{2.8}$$

Here i, j, k are the integers and indices in x, y, z coordinates; n is an integer and corresponds to the time steps; Δt is the increment of time; and $\Delta x, \Delta y, \Delta z$ are the increment of space in each direction.

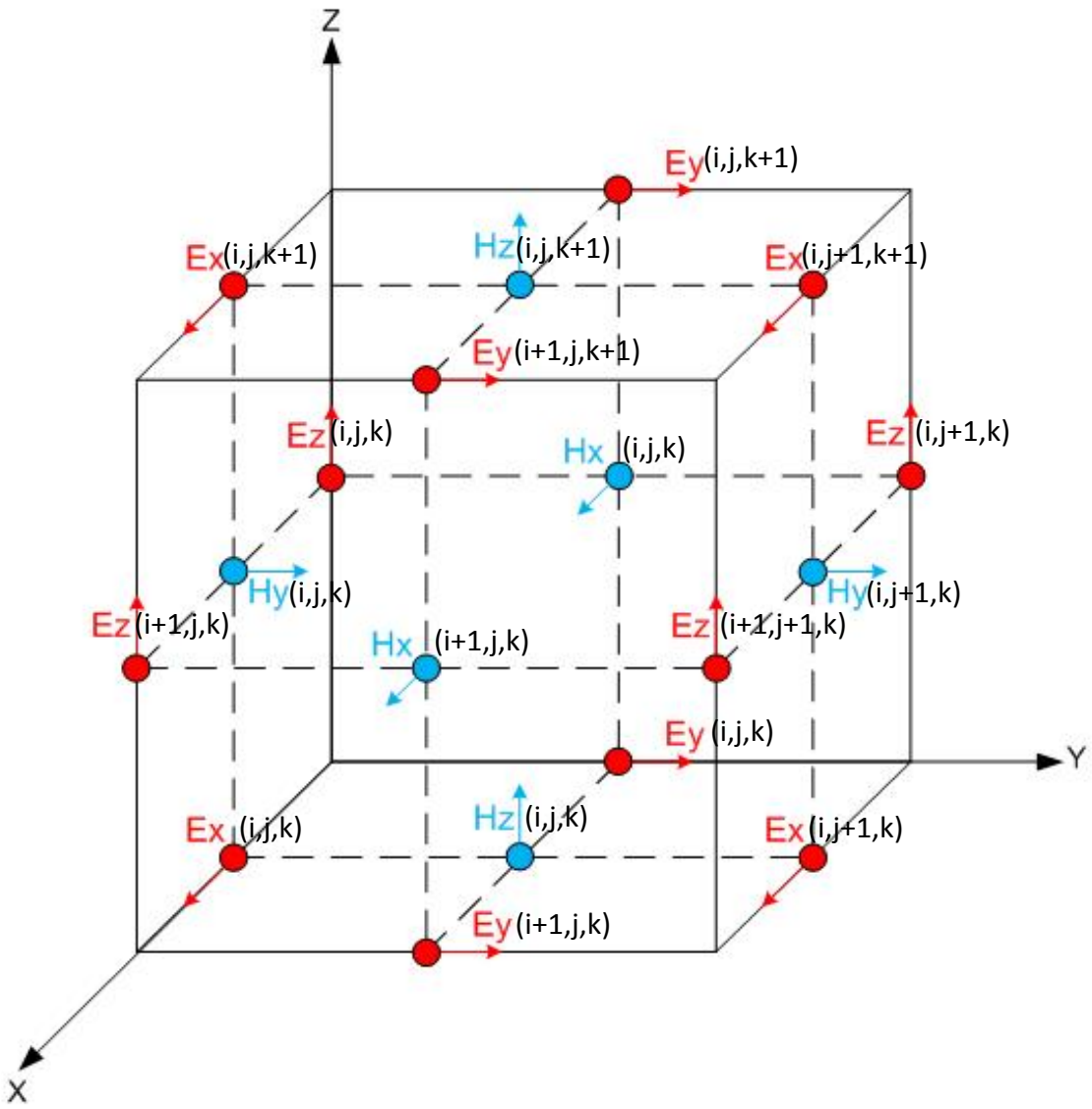

Fig. 2.2 Yee's lattice (unit cell) in a 3D meshed grid in FDTD method.

Similarly, the first time partial derivative in space of f, at a particular space point (i, j, k) is [Taflove, 1995]:

$$\frac{\partial f}{\partial t}(i\Delta x, j\Delta y, k\Delta z, n\Delta t) = \frac{f_{i,j,k}^{n+1/2} - f_{i,j,k}^{n+1/2}}{\Delta t} + O[(\Delta t)^2] \ . \qquad (2.9)$$

Yee used a central-difference expression for both space and time derivatives, so that Yee's scheme is accurate to the second order in both space and time.

Considering a source-less situation with a non-chiral, linear material, Maxwell's equations (1.1.3) Faraday's law and (1.1.4) Ampere's law, together with the relations between $\mathbf{B}$ and $\mathbf{H}$, $\mathbf{D}$ and $\mathbf{E}$, are listed as:

$$\nabla \times \mathbf{H} - \frac{\partial \mathbf{D}}{\partial t} = 0 \ , \qquad (2.10.1)$$

$$\nabla \times \mathbf{E} + \frac{\partial \mathbf{B}}{\partial t} = 0 \ , \qquad (2.10.2)$$

$$\mathbf{D} = \varepsilon \mathbf{E} \ , \qquad (2.10.3)$$

$$\mathbf{B} = \mu \mathbf{H} \ , \qquad (2.10.4)$$

Here ε is electric permittivity, and μ is magnetic permeability.

We can write the FDTD time stepping formulas in a Cartesian coordinate system that are induced from above four equations

:

$$E_x\Big|_{i,j,k}^{n+1} = E_x\Big|_{i,j,k}^{n} + \frac{\Delta t}{\varepsilon_{i,j,k}}\left(\frac{H_z\Big|_{i,j,k}^{n+1/2} - H_z\Big|_{i,j-1,k}^{n+1/2}}{\Delta y} - \frac{H_y\Big|_{i,j,k}^{n+1/2} - H_y\Big|_{i,j,k-1}^{n+1/2}}{\Delta z}\right)$$

$$E_y\Big|_{i,j,k}^{n+1} = E_y\Big|_{i,j,k}^{n} + \frac{\Delta t}{\varepsilon_{i,j,k}}\left(\frac{H_x\Big|_{i,j,k}^{n+1/2} - H_x\Big|_{i,j,k-1}^{n+1/2}}{\Delta z} - \frac{H_z\Big|_{i,j,k}^{n+1/2} - H_z\Big|_{i-1,j,k}^{n+1/2}}{\Delta x}\right)$$

$$E_z\Big|_{i,j,k}^{n+1} = E_z\Big|_{i,j,k}^{n} + \frac{\Delta t}{\varepsilon_{i,j,k}}\left(\frac{H_y\Big|_{i,j,k}^{n+1/2} - H_y\Big|_{i-1,j,k}^{n+1/2}}{\Delta x} - \frac{H_x\Big|_{i,j,k}^{n+1/2} - H_x\Big|_{i,j-1,k}^{n+1/2}}{\Delta y}\right) \quad . \quad (2.11)$$

$$H_x\Big|_{i,j,k}^{n+1/2} = H_x\Big|_{i,j,k}^{n-1/2} - \frac{\Delta t}{\mu_{i,j,k}}\left(\frac{E_z\Big|_{i,j+1,k}^{n} - E_z\Big|_{i,j,k}^{n}}{\Delta y} - \frac{E_y\Big|_{i,j,k+1}^{n} - E_y\Big|_{i,j,k}^{n}}{\Delta z}\right)$$

$$H_y\Big|_{i,j,k}^{n+1/2} = H_y\Big|_{i,j,k}^{n-1/2} - \frac{\Delta t}{\mu_{i,j,k}}\left(\frac{E_x\Big|_{i,j,k+1}^{n} - E_x\Big|_{i,j,k}^{n}}{\Delta z} - \frac{E_z\Big|_{i+1,j,k}^{n} - E_z\Big|_{i,j,k}^{n}}{\Delta x}\right)$$

$$H_z\Big|_{i,j,k}^{n+1/2} = H_z\Big|_{i,j,k}^{n-1/2} - \frac{\Delta t}{\mu_{i,j,k}}\left(\frac{E_y\Big|_{i+1,j,k}^{n} - E_y\Big|_{i,j,k}^{n}}{\Delta x} - \frac{E_x\Big|_{i,j,k+1}^{n} - E_x\Big|_{i,j,k}^{n}}{\Delta y}\right)$$

The discreteness of fields and time gives approximated results of the given electromagnetic problem. With the space grid and time step made smaller, this approximation becomes closer and closer to the true continuous fields, until convergence problems arise. Many practical problems can be simulated using this scheme, by reducing the size of the cell to achieve desired accuracy.

2.2.2 MEEP (MIT Electromagnetic Equation Propagation).

In this dissertation, the computational simulations are done with the FDTD method, using a freely available software package MEEP (MIT Electromagnetic Equation Propagation). Detailed information about the functions of the software can be found in their publication [Farjadpour et al, 2006; Oskooi et al, 2009; Oskooi et al, 2010], as well as on their website http://ab-initio.mit.edu/wiki/index.php/Meep. Relevant physics knowledge and examples can be found in the book "Photonic Crystals" [Joannopoulos, 2008]. Here, I will give a brief summary of the MEEP software.

Electric permittivity ε is in general frequency ω dependent, and MEEP supports any dielectric function in the form of a Lorentzian model, the details of which will be given later. The form is given as

$$\varepsilon = \varepsilon_\infty + \sum_j \frac{\sigma_j \omega_j^2}{\omega_j^2 - \omega^2 - i\gamma_j \omega} \ . \qquad (2.12)$$

The dielectric function has a term that is frequency independent, and a set of the harmonic resonances. ε_∞ is the frequency independent instantaneous dielectric constant, ω_j is the jth resonant frequency, γ_j is the resonance loss rate, and σ_j is a function to define the strength the jth resonance. Here all variables except ω, which is the frequency of the field, are user-defined constants. Theoretically, any $\varepsilon(\omega)$ can be

modeled by a number of these terms. Practically, we choose only several terms because the limitation of the memory and speed of the computer.

For the equations (2.10) and (2.11), having frequency-dependent ε causes computational difficulties (divergence etc.). A technique can be used to solve this problem. Using the original definition of electric displacement,

$$\mathbf{D} = \varepsilon_0 \mathbf{E} + \mathbf{P} . \qquad (2.13.1)$$

Knowing the electric polarization $\mathbf{P} = \varepsilon_0[\varepsilon(\omega) - 1]\mathbf{E}$ and considering equation (2.12), the polarization $\mathbf{P}$ along the electric field evolves via equation:

$$\frac{\partial^2}{\partial t^2}\mathbf{P} + \gamma_j \frac{\partial}{\partial t}\mathbf{P} + \omega_j^2 \mathbf{P} = \omega_j^2 \mathbf{E} . \qquad (2.13.2)$$

The equation (2.10.3) is substituted by two equations (2.13.1) and (2.13.2), in which the coefficients are no longer frequency ω dependent. The same procedure can be followed for the magnetic permeability. Thus for equations (2.10.1) - (2.10.4), we have six equations without the explicit frequency ω dependence. This will make the computational scheme more stable and more easily convergent.

Using the FDTD method described in earlier section, the new set of equations can be solved to get the electric and magnetic fields throughout the whole space.
Simulations must obey some boundary conditions, and there are different ways to define the boundary conditions [Anderson, 2001; Taflove, 2005; Oskooi et al, 2010]. Three basic types of boundary conditions are supported in MEEP: Bloch-periodic boundaries,

with the fields satisfying $f(x+L) = f(x)$; metallic walls, where the fields are forced to be zeros; and the perfect matching layer (PML) boundary condition, first proposed by Berenger [1994], which is a boundary made by fictitious material that absorbs all fields and has zero reflections. Different boundary conditions are chosen to be used in the simulations, depending on the problems. MEEP can be used to analyze electromagnetic problems in a few different ways, such as Field patterns and Green's functions, transmission/reflection spectra, and resonant modes. Different functions are chosen to help with the research to be accomplished.

2.3 Material parameters

Just as good samples are critical for obtaining good results in experiments, a precise description of the material (optical) parameters and permittivity over the chosen spectra is needed in order to perform high-fidelity simulations. The models with one Drude term and some Lorentzian terms are more commonly used [Vial et al, 2005; Lee & Gray, 2005; Skinner & Byrne, 2006; Pernice et al, Liu et al, 2007; Rodrigo, 2008]. Some improved extended models with four or five Lorentzian terms are claimed to be more accurate in different wavelength ranges [Hao & Nordlander, 2007, Rakic, 1998]. There

are also other models, such as the critical points (CP) model [Etchegoin et al, 2006; 2007] having been introduced recently.

In my research, for the different materials involved, a lot of the dielectric parameters are complex and frequency dependent functions. We choose to develop our own models based on the experimental data. Because the complexity of the multiple Lorentzian terms slows down the simulation and may cause divergence during the computation, more than one model is developed for some materials. For example, for metals, we have a simple classical Drude model and a Lorentz-Drude multi-oscillator model which consists of one Drude term and multiple Lorentzian terms. Simpler models are often used for a quick test; then a more complicated model will be used to achieve precise results. For dielectric materials, we only need to consider the real part of ε for most dielectrics. However, Lorentzian terms are used to model dielectrics with complicated dielectric functions.

2.3.1 Material dielectric functions

We work with non-magnetic materials, i.e. $\mu = 1$. We need to find a good model for only the dielectric functions to further our theoretical research. We first consider the classic Drude model [Drude, 1900]. The basic assumptions include: independent electrons, i.e. electron-electron interactions are not considered; free electrons, i.e. electron-ion interactions are not considered; and core scattering, i.e. only the scattering of electrons -

ion cores are considered. Electrons oscillate in response to an external driving field $\mathbf{E}$. The oscillations are damped at a characteristic damping frequency $\gamma = 1/\tau$. Here τ is the relaxation time of free electrons. The equation of the electron plasma motion is

$$m\ddot{\mathbf{x}} + m\gamma\dot{\mathbf{x}} = e\mathbf{E} \ , \qquad (2.14)$$

where m is the effective mass of an electron; and e is the effective charge of an electron. Since we assume the driving field has a harmonic time dependence of

$$\mathbf{E}(t) = \mathbf{E}_0 \exp(-i\omega t),$$

so a time-harmonic solution for the position of the electrons can be written as

$$\mathbf{x}(t) = \mathbf{x}_0 \exp(-i\omega t),$$

and we have $\ddot{\mathbf{x}} = -\omega^2\mathbf{x}$ and $\dot{\mathbf{x}} = -i\omega\mathbf{x}$. Substituting these into Eq (2.14), we find

$$-m\omega^2\mathbf{x} - im\gamma\omega\mathbf{x} = e\mathbf{E}$$

So $$\mathbf{x} = -\frac{(e/m)\mathbf{E}}{\omega^2 + i\gamma\omega} \ . \qquad (2.15)$$

The dipole moment of each electron is $\mathbf{p} = e\mathbf{x}$, so the macroscopic polarization is

$$\mathbf{P} = ne\mathbf{x} \ , \qquad (2.16)$$

where n is the charge density. Inserting Eq. (2.14) into Eq. (2.16), we get

$$\mathbf{P} = -\frac{(ne^2/m)\mathbf{E}}{\omega^2 + i\gamma\omega} \ , \qquad (2.17)$$

and since $\mathbf{D} = \varepsilon_0\mathbf{E} + \mathbf{P}$, insertion of Eq. (2.17) into this gives

$$\mathbf{D} = (1 - \frac{(ne^2/\varepsilon_0 m)}{\omega^2 + i\gamma\omega})\varepsilon_0\mathbf{E} \ , \qquad (2.18)$$

or $$\mathbf{D} = (1 - \frac{\omega_p^2}{\omega^2 + i\gamma\omega})\varepsilon_0 \mathbf{E} \ . \qquad (2.19)$$

where $\omega_p = \sqrt{\frac{ne^2}{\varepsilon_0 m}}$ is the plasma frequency of free electron gas [Langmuir, 1928].

Now we have the dielectric function as

$$\varepsilon = 1 - \frac{\omega_p^2}{\omega^2 + i\gamma\omega} \ . \qquad (2.20)$$

For alkali metals, there is no loss/decay, so that $\gamma = 0$. Eq (2.20) reduces to Eq. (1.8).

Yet for noble metals, some of the bound electrons also contribute to the polarization, which requires a small correction to the dielectric function, and it becomes

$$\varepsilon = \varepsilon_b - \frac{\omega_p^2}{\omega^2 + i\gamma\omega} \ , \qquad (2.21)$$

where ε_b is usually between 1 and 10. Eq. (2.21) is also called the extended Drude model.

The classic Drude model works well for alkali metals throughout the spectrum, but begin to show discrepancies for noble metals for the visible light portion of the spectrum. The Lorentz model considers an extra linear restoring force experienced by a single electron. Then equation (2.14) can be rewritten as

$$m\ddot{\mathbf{x}} + m\gamma\dot{\mathbf{x}} + K\mathbf{x} = e\mathbf{E} \ . \qquad (2.22)$$

By following the same procedure and defining the resonant frequency as $\omega_0^2 = K / m$

$$\mathbf{x} = \frac{(e/m)\mathbf{E}}{\omega_0^2 - \omega^2 - i\gamma\omega} \quad . \tag{2.23}$$

The complete dielectric function will then be

$$\varepsilon = \varepsilon_b + \frac{\omega_p^2}{\omega_0^2 - \omega^2 - i\gamma\omega} \quad . \tag{2.24}$$

Combining equations (2.21) and (2.24), we have the Lorentz-Drude multi-oscillator model:

$$\varepsilon = \varepsilon_b - \frac{\omega_p^2}{\omega^2 + i\gamma\omega} + \sum_j \frac{f_j \omega_{p,j}^2}{\omega_{0,j}^2 - \omega^2 - i\gamma_j \omega} \quad . \tag{2.25}$$

The first term is the bound-electron contribution; the second term is often referred as the Drude term; and there are j Lorentz terms. Each Lorentz term has its strength f_j, the plasma frequency $\omega_{p,j}$, resonant frequency $\omega_{0,j}$, and the damping frequency γ_j.

Comparing the physics model Eq. (2.25) and the model used in the MEEP equation (2.12), and noting that the Drude term can be viewed as one of the Lorentz terms with resonant frequency as 0, we understand that MEEP's model bears a close relation with the Lorentz-Drude model. Most times, by using 1 to 4 Lorentz terms, as shown later, we are able to build good models for the noble metals, such as silver and gold, which fits well with the experimental dielectric data. For the dielectric, we can just treat equation (2.14) as a mathematic model, and the same method can also be used to model the dielectric function of dispersive dielectrics based on experimental data.

2.3.2 Metals

Metals are an essential part of the different nanostructures being explored in this dissertation. $\varepsilon(\omega)$ of the metals can be determined by optical experiments, and data banks of the refractive indexes are readily available [Johnson & Christy, 1972]. Silver (Ag) is one of the metals we use a lot in our simulations. I use silver as an example to show how we develop metal parameters in out simulations. Other metals, such as gold (Au) and Titanium (Ti), are dealt with in similar way.

We have developed different simulation models based on the experimental data given in the paper by Johnson and Christy [1872], using both the classic Drude model with only the Drude term, and the Lorentz-Drude model with one Drude term and multiple Lorentzian terms. Fig. 2.3 shows two sample models of the dielectric function of Ag, together with the experimental data. The classic Drude model gives surprisingly good results in most calculations done within the optical range. The extended Lorentz-Drude model gives more precise results throughout the whole spectra.

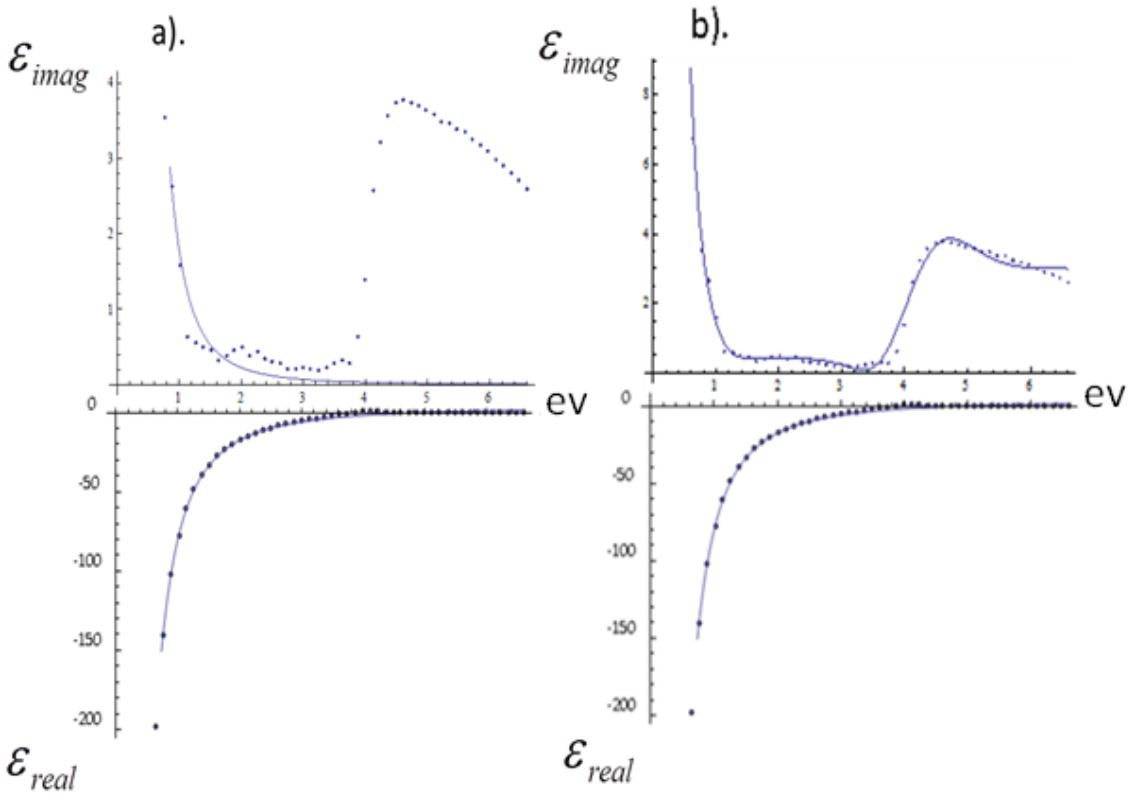

Fig. 2.3 Dielectric function of silver corresponding to the photon energy in eV. In all the plots, the scattered points are experimental data, and the solid lines are fit from the models. The imaginary part (ε_2) is shown in the top plot, and the real part (ε_1) is shown in the bottom plot. a). Classic Drude model, b). Extended Lorentz-Drude model with four Lorentz terms.

2.2.3 Dielectric materials

Dielectrics are represented by real dielectric constants, or dielectric functions. The parameters are either known from data banks, or can be determined by reflection/ transmission experiments.

Some of the dielectric materials we use in the simulations have simple forms, e.g. only the real part of the dielectric constants. The examples include air ($\varepsilon = 1$), glass ($\varepsilon = 2$) and ITO ($\varepsilon = 2$) and other simple non-loss materials. These materials are very easy to define, and seldom cause problems in the simulations.

Other dielectric materials have both real and imaginary parts of the permittivity, and situations may be a little bit more complicated for these materials. One example of this kind of dielectric materials that we use in the simulations, is the amorphous silicon (a-Si). The experimental dielectric parameters are known in the literature [McKenzie et al, 1983; Willardson et al, 1984]. Fig. 2.4 shows the experimental complex dielectric function vs. vacuum wavelength, and the corresponding fits. The more important part is the imaginary part, since we use a-Si as an absorber in our nanostructures, and the imaginary part of the permittivity controls the absorbing property.

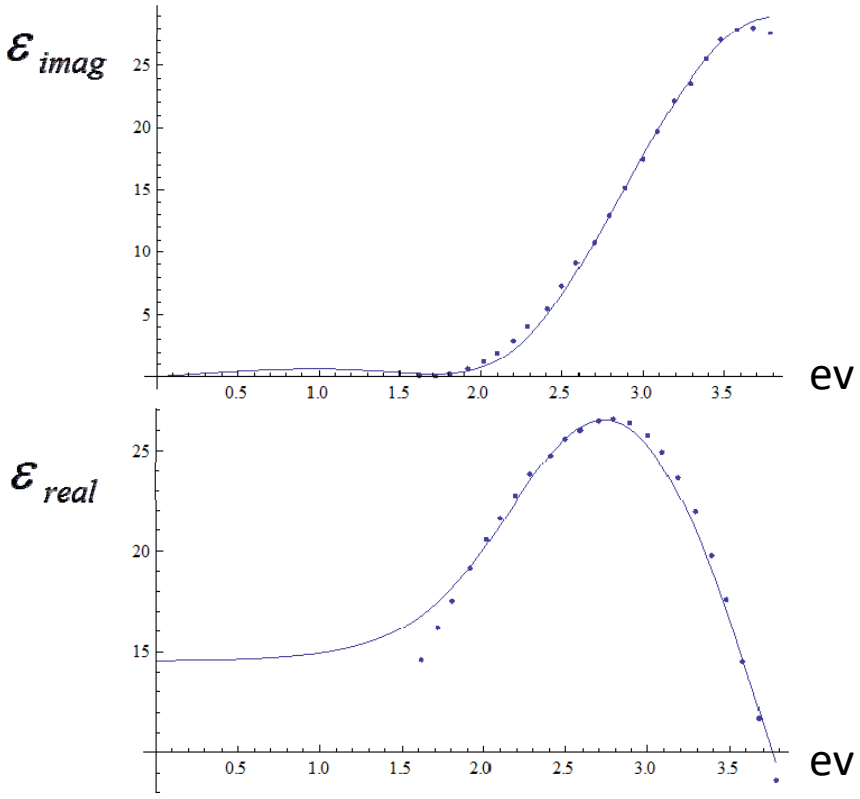

Fig. 2.4 Dielectric function of a-Si. The scattered points are experimental data, and the solid lines are fit from the models. Imaginary part (ε_2) is shown in the top plot, and real part (ε_1) is shown in the bottom plot. The model has two Lorentz terms.

Chapter 3

Plasmonics of a nanowire

On the metal-dielectric interface, light can excite surface plasmons, which can propagate along the interface for some distance, then couple back into the light at an outlet. In this chapter, I study the SPs in Ag nanowires with the help of MEEP, and the research findings are in agreement with the analytical results [Takahara et al, 1997], experimental results [Ditlbacher et al, 2005; Schider et al, 2003] and some preliminary simulation results [Laroche & Girard, 2006; Laroche & Vial, 2007]. The plasmon dispersion relations of the Ag nanowire, along with other properties, are achieved through the simulations. Portions of the materials from this chapter are being prepared for submission to a peer reviewed journal.

3.1 Introduction

Surface plasmons interact with photons to form surface plasmon polaritons, which are often referred to as surface plamons (SPs). SPs can be excited by light, can propagate along the interface, and be coupled back into light. Ag nanowires have been fabricated [Krenn, 2002; Sun et al, 2002; Sun et al, 2003] and studied for their plasmonic applications [Sanders 2006; Takajara, 1997]. Visible light that is coupled into a Ag nanowire, and the SPs can propagate for many micrometers, and their plasmonics have been studied both experimentally and theoretically [Dickson & Lyon, 2000; Ditlbacher et al, 2005; Graff et al, 2005; Sanders, 2006; Takahara, 1997]. My research continues the theoretical research on plasmonics of the Ag nanowires.

For Ag, the bulk free-electron plasmon frequency is well known, with the value $\omega_p \approx 8.99eV$. The surface plasmon frequency for a flat planar interface between Ag and a medium with dielectric constant ε_m is given by $\omega_{sp} = \omega_p / \sqrt{\varepsilon_b + \varepsilon_m}$. We assume the medium is air, so $\varepsilon_m = 1$. Since $\varepsilon_b = 5.6$ for Ag, the surface plasmon frequency is $\omega_{sp} \approx 3.5eV$. For Ag nanospheres, the plasmon frequency (Mie frequency), is given by $\omega_{Mie} = \omega_p / \sqrt{\varepsilon_b + 2\varepsilon_m}$ [Mie, 1908], which leads to $\omega_{Mie} \approx 3.2eV$. I show that for Ag nanowires, the non-retarded surface plasmon frequency $\omega_{wire} = \omega_{sp}$.

The ends of silver nanowires can act as a “lightening-rod”, enhancing a local, optical-frequency electric field [Bader & Jamid, 2007; Muhlschlegel et al, 2005; Tao & Yang, 2005]. A group of our collaborators (Fourkas et al) have utilized this effect to drive nonlinear generation of the luminescence at the ends of the nanowires [Nah et al, 2010]. Polymerization in certain photoresist happens at both the proximal and distal nanowire ends. In addition to the luminescence at the ends, light leakage/coupling also occurs when another nanostructure is brought close to the nanowire [Fang et al, 2010; Sanders et al, 2006]. I simulate the phenomena of both the “lightening rod” and “light leakage/ coupling” effects, and visualize them in terms of the electric field intensity.

3.2 Simulation Results

A silver nanowire of 2 μm length and 50 nm radius is placed in a low refractive constant material. Fig. 3.1 (a) shows the cross section of a silver nanowire submerged in a material with refractive index 1.7. A laser beam is focused on the left end of the wire in an area of 150x150 nm, moving along the y-direction, with the E field polarized along the z-direction. Fig. 3.1 (b) and (c) show the field propagation maps for incident vacuum wavelengths of 365 nm and 730 nm, respectively.

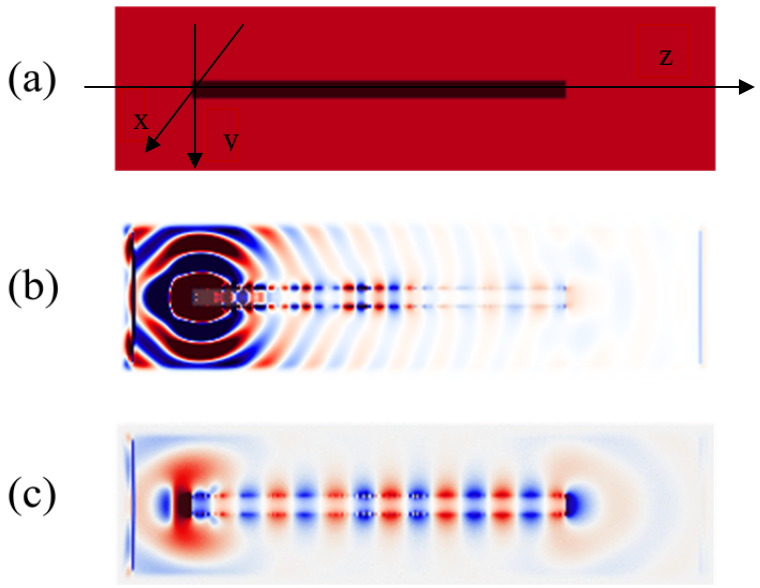

Fig. 3.1 Illustration of SPs propagation along a Ag nanowire. (a) Ag nanowire with 2 μm length and 50 nm radius submerged in a dielectric material with $n \approx 3.4$. (b) and (c) SPs propagation maps for different incident wavelengths of 365 nm and 730 nm. The color intensity is proportional to E_z amplitude, and color represents E_z sign (direction).

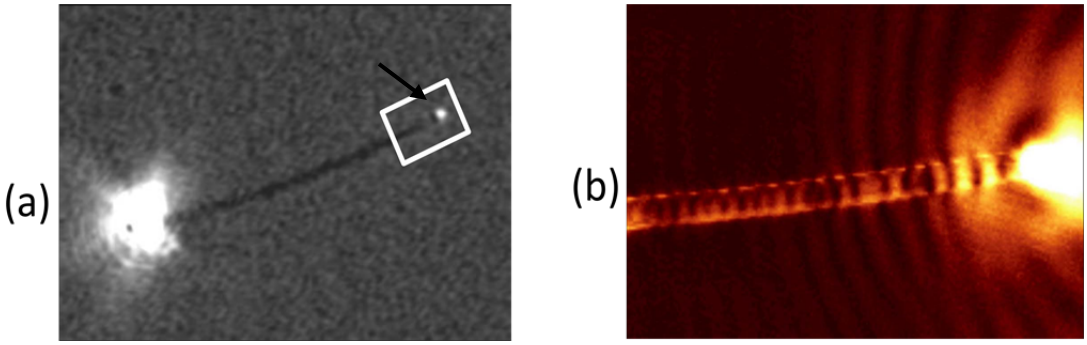

Fig. 3.2 SPs propagating along a 18.6 μm long Ag nanowire. (a) Microscopic image: the bright spot to the left is due to the focused exciting light. The arrow indicates light scattered from the distal wire end. (b) SNOM image—the image area corresponds to the white box in (a). The pictures are taken from [Ditlbacher et al, 2005].

Knowing that the energy density is proportional to the square of the field amplitude, one easily oberves that Fig. 3.1 (c) agrees nicely with Fig. 3.2, which is the scanning near-field optical microscopy (SNOM) image reported by Ditlbacher et al (2005).

I have developed a more systematic way to study the plasmonics of a similar system. This involves a Ag nanowire surrounded by air. A laser beam is focused on the left end (the proximal end) of the wire in an area of 150x150 nm, and is going along the y-direction, with the E field polarized along the z-direction. The flux spectra are measured on the other end, the distal end, of the nanowire. Spectra for Ag nanowires of length 2, 4, 6, 8, 10, and 12 μm are simulated. The results are shown in Fig. 3.3.

The oscillations in Fig. 3.3 show that the nanowire behaves much like a resonating nanoFabry-Perot cavity, in which standing waves form. Similar phenomenon have been observed in experiments [Ditlbacher et al, 2005], and simulations [Laroche & Girard, 2006; Laroche & Vial, 2007]. Assuming that the nanowires act like Fabry-Perot cavities means that the spectra minima occur at the Febr-Perot resonances with the resonant wavelength $\lambda_n = 2l/n$, where n is an integer. Knowing the energy/frequency of the corresponding resonances, we can obtain the dispersion relation; this is shown as small black dots in Fig. 3.4. As can be seen from Fig. 3.4, the simulation results are very close to the experimental values, as indicated by the crosses. These are experimental results obtained by Ditlbacher et al (2005), where the Ag nanowires of 120 nm diameter and of various lengths are deposited on glass. The experimental results have been normalized to

their vacuum values by dividing their wave vectors by effective refractive index number $\bar{n} = 1.275$ ($\bar{n} = \sqrt{(\varepsilon_{glass} + \varepsilon_{air})/2} = 1.275$, with $\varepsilon_{glass} = 2.25$). My calculations agree well with the normalized experimental results, and it is clear from Fig. 3.4 that we can treat silver nanowires as Fabry-Perot resonators.

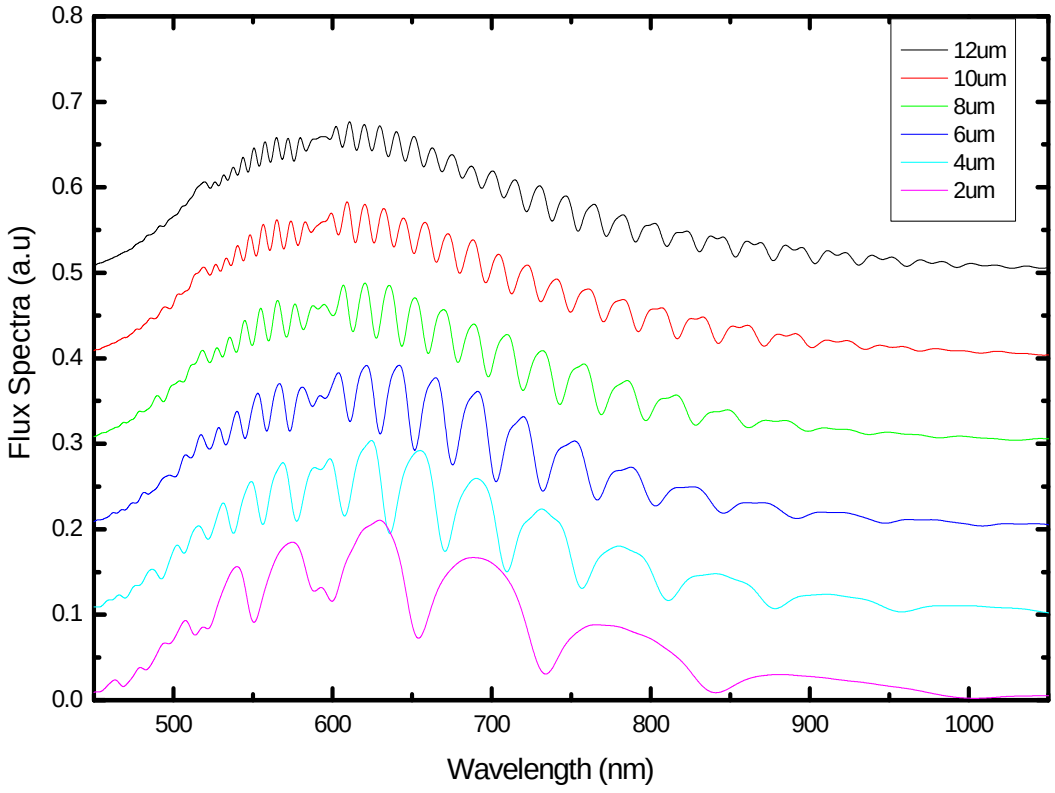

Fig. 3.3 Simulated flux spectra vs. vacuum wavelength for various wire lengths. From the bottom to the top, the lengths are 2, 4, 6, 8, 10, and 12 μm respectively. The spectra are offset for clarity.

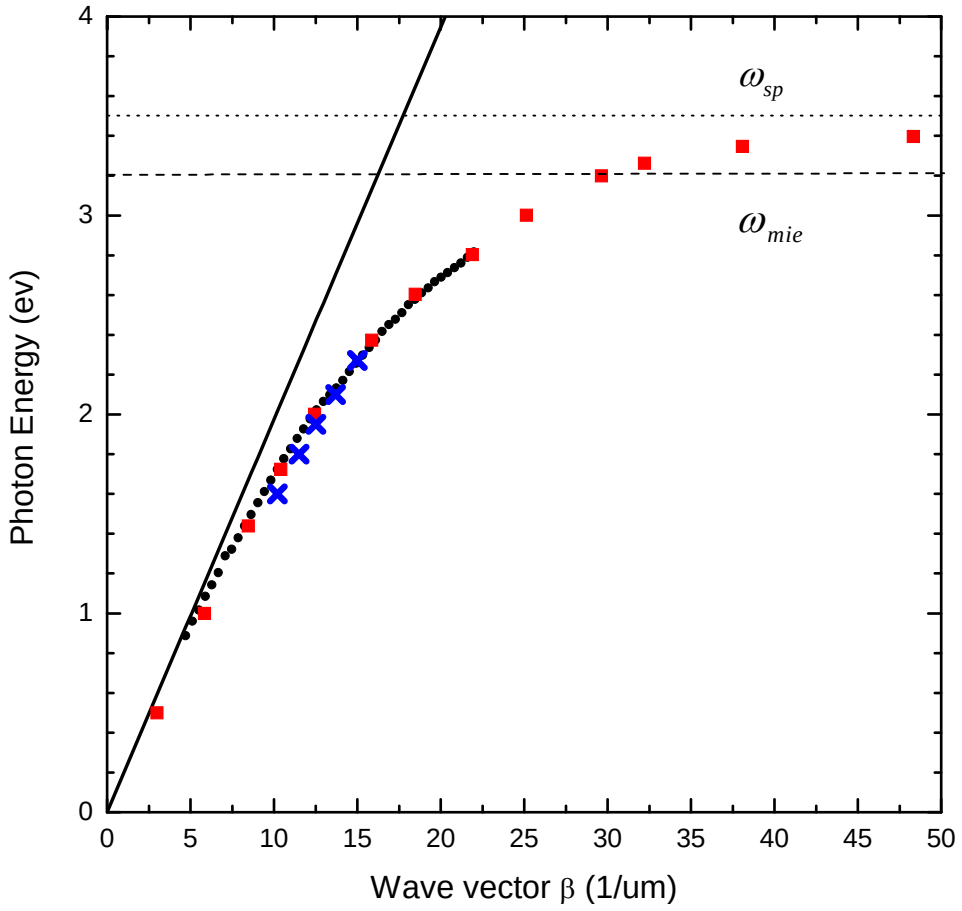

Fig. 3.4 Photon energy vs. wave vector in the z-direction for a Ag nanowire. Solid line: Light line in vacuum. Dotted line: surface plasmon frequency $\omega_{sp} \approx 3.5eV$. Dashed line: nanosphere plasmon frequency $\omega_{mie} \approx 3.2eV$. Small black dots: Dispersion relation calculated from the flux spectra, assuming that the spectra minima happen at Fabry-Perot resonances. Big red squares: Dispersion relation derived directly from simulation results for an infinitely long nanowire. Blue crosses: Normalized experimental results from Ditlbacher et al (2005).

We also want to find out whether these resonances are Fabry-Perot resonances of surface plasmons. We have uses a direct way to simulate the surface plasmon dispersion relation of an infinitely long silver nanowire. We simply simulate the field distribution of the propagating surface plasma wave, and take "snapshots/maps" of the field before the wave reaches the other end of the nanowire. Direct measurement of the field maxima locations determines the wavelength λ_{sp} of SPs in an infinitely long wire. From this we obtain the wave vector $\beta = 2\pi / \lambda_{sp}$. Fig. 3.5 shows such an electric field distribution map along the silver nanowire surface at a given incident photon energy. By repeating this procedure for a number of frequencies of incident light, I obtain the dispersion relation of an infinitely long Ag nanowire. The results are shown in Fig. 3.4 as big red squares.

The dispersion of surface plasmons on an infinitely long Ag wire, agrees with the results for Fabry-Perot resonances, so we can conclude that the Ag nanowire can indeed be viewed as Fabry-Perot resonator of surface plasmons. Another convenient result, as indicated in Fig. 3.4, is that the limit of the SP frequency of Ag nanowire seems to be very close to $\omega_{sp} \approx 3.5eV$. This is also what we can derive from our analytic results. In equation (2.6) from the previous chapter, when $k_z a \to \infty$, $I_0(k_z a)K_1(k_z a) \to \frac{1}{k_z a}$ and $I_1(k_z a)K_0(k_z a) \to \frac{1}{k_z a}$. This immediately implies $\varepsilon_1 + \varepsilon_2 = 0$. Given our Ag parameter, we have $\omega_{wire} = \omega_{sp} \approx 3.5eV$.

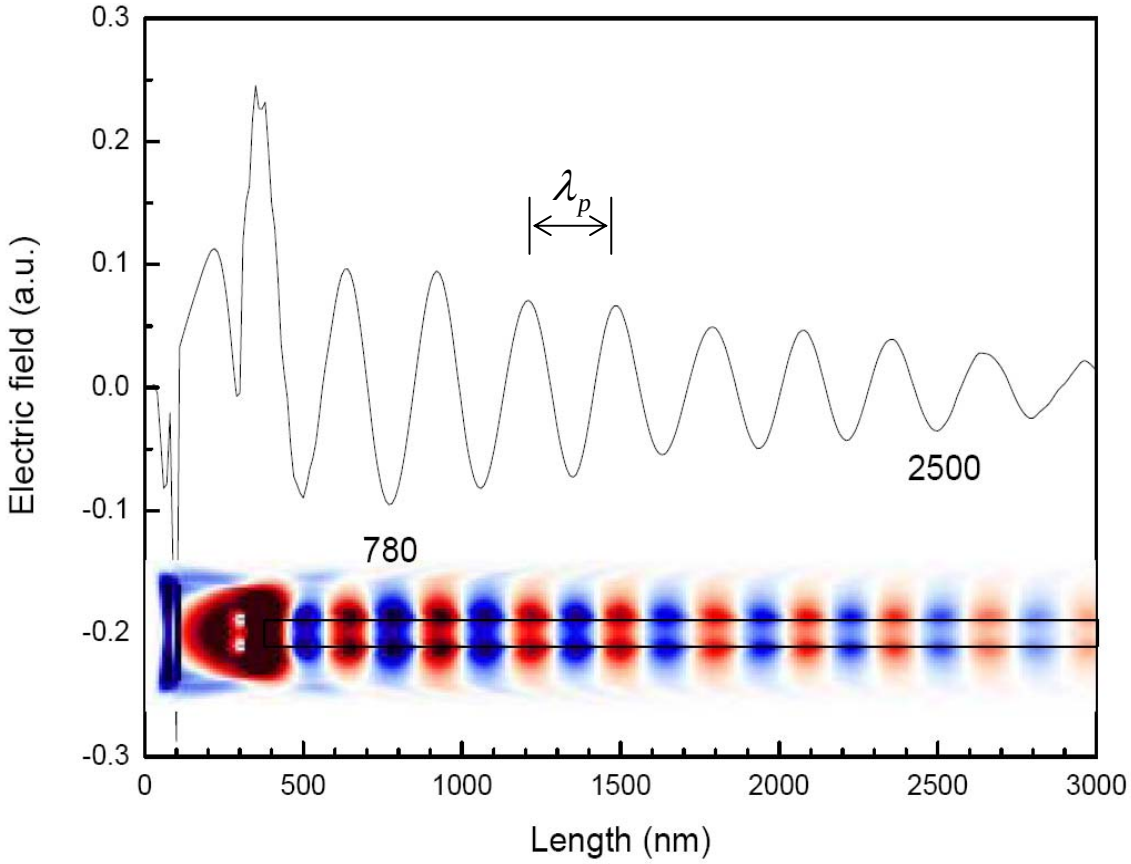

Fig. 3.5 E_z field distribution along a Ag nanowire-air surface. The nanowire is 8 μm in length and has a 50 nm radius. The incident light has photon energy of 2.8 ev, e.g. vacuum wavelength 442 nm. The measured SPP wavelength is 287 nm, so the SP wave number is calculated to be 21.89 (1/μm). The colored electric field map across the Ag nanowire is shown to scale with the plot. The color intensity is proportional to the E_z amplitude, and color represents the E_z sign (direction).

By using the same method of taking snapshots, and plotting along the direction perpendicular to the silver nanowire, the decay in the axial direction can be extracted. One example is shown in Fig. 3.6, where we plot the E_z field distribution across the nanowire. Considering the lowest TM mode, one can follow the analytic method described in Chapter 2, and easily find that the field's axial decay follows the modified Bessel function $E_{z2} = BK_0(q\rho)$ for $\rho > a$, where a is the radius of the nanowire. From the plot in Fig. 3.6, one can see that the field slowly decays with the distance from the wire to about half of its magnitude at 150 nm. Our simulation results are in good agreement with the predictions of Takahara (1997).

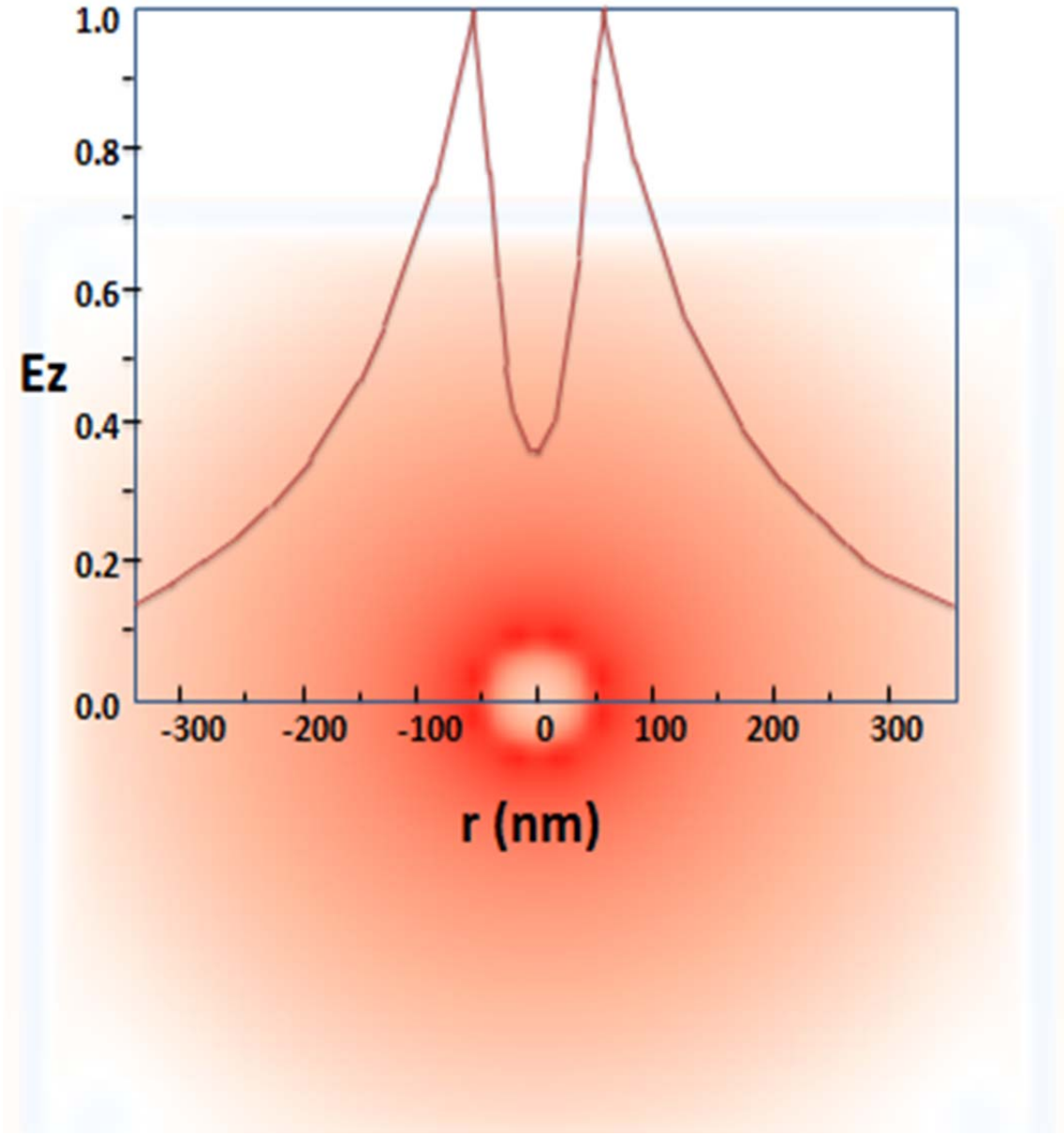

Fig. 3.6 E_z field distribution along the middle line perpendicularly across the silver nanowire. The electric field is normalized against the electric field at the surface, where the field is the strongest. The colored background shows the map of the E_z field across the silver nanowire. The color intensity is proportional to the E_z amplitude, and color represents the E_z sign (direction).

3.3 Experimental Studies

Ag nanowire can guide the SPs that are excited by light for a long distance of a few microns, and then emit light at the end of the nanowire. Our collaborators at Maryland University, John Fourkas's group, use these nanowires to guide luminescence to induce polymerization in a photoresist at both the nanowire ends. In addition, as shown in my simulation, the field of the SP wave extends well outside the wire along the surface as well. It is not hard to imagine that when another nanostructure is brought in the proximity of the nanowire, SPs can couple to the other nanostructure. The leakage of guided light [Sanders et al, 2006; Fang et al, 2010] induces polymerization and "spot-welds" the nanostructure to the nanowire. By combining this technique with a method for solution-based nanomanipulation [Ropp et al, 2010; Ropp et al, 2010], Fourkas et al demonstrate the high-precision fabrication of nanophotonic devices. Our research helps to understand the procedure and predict more possible applications.

Simulations show that the field enhancement occurs along the entire surface of the wire, and thus the surface field enhancement should polymerize a thin film of resist (tens of nanometers) along the wire surface. This indeed happens in the experiment, and this thin film acts as "instant glue" that immobilizes the adjacent wires or quantum dots (QDs) to the wire. Fig. 3.7 shows the simulation of the field distribution of a silver nanowire and different adjacent nanostructures.

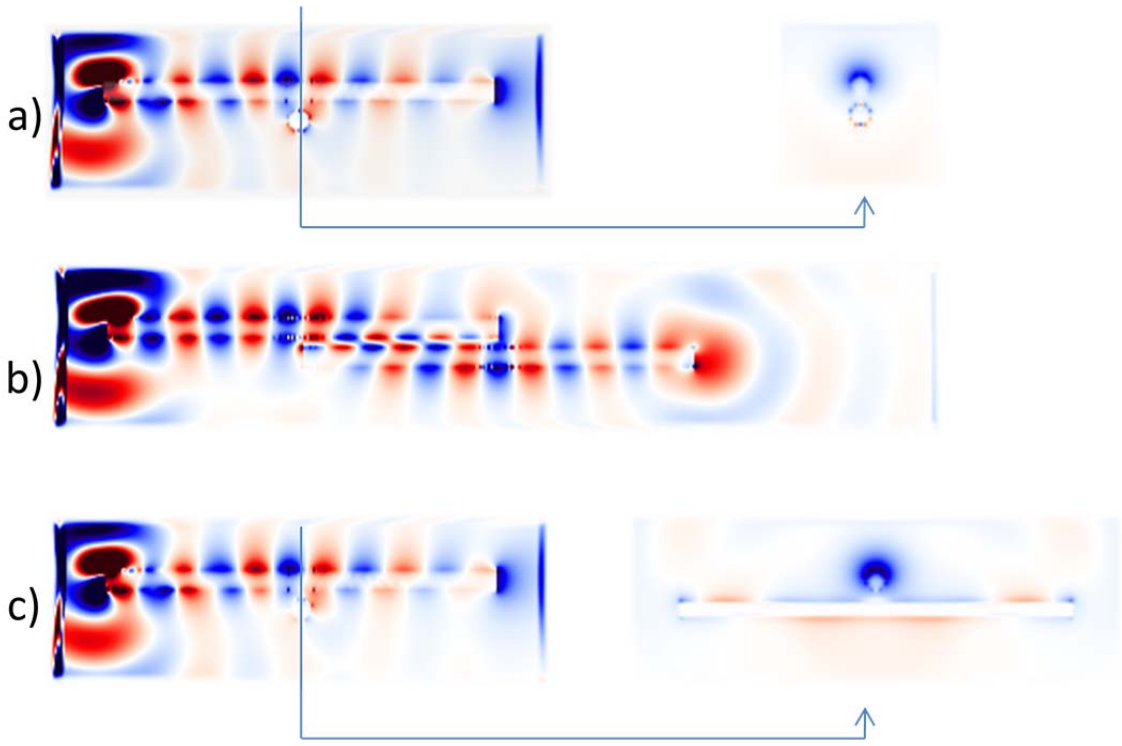

Fig. 3.7 Plasmonic coupling: E_z field at different cross sections showing an electromagnetic wave of 800 nm (vacuum) wavelength propagating along a Ag nanowire of diameter 100 nm coupling optically to a), or a Ag nanosphere (a QD) of diameter 100 nm; b), another Ag nanowire that is parallel to the first nanowire; c), another Ag nanowire that is perpendicular to the first nanowire. The left end of the Ag nanowire is excited locally by an electromagnetic wave. The distance between the Ag nanowire and the adjacent nano-structure is 50 nm. The color intensity is proportional to the E_z amplitude, and color represents the E_z sign (direction).

As shown in Fig. 3.7, the SPs couple onto the adjacent nanostructures and enhance the electric field on the ends and their surfaces. The pictures are only snapshots of the field distribution at a given time; more information is available from looking at the field evolution over time. In the appendix, a series of pictures of the electric field distribution evolving over time clearly illustrates that the coupling between the silver nanowire and other nanostructures can be strong at times.

Fourkas et al. utilize the "lightening-rod" and "leakage" effects, combined with solution-based nanomanipulation [Ropp et al, 2010; Ropp et al, 2010], to fabricate nanophotonic devices of high precision; and their results are to be published soon [Nah et al]. The detailed experimental set-up and procedure can be found in their publications [Nah et al, 2010; Nah et al, to be published]. The basic idea will be introduced briefly here. Ag nanowires are deposited on substrates, and submerged in certain liquid photoresist solution. A laser beam shines on the Ag nanowire in the solution. Non-linear optical excitations happen and SPs are excited and propagate along the nanowire. Polymerization happens where SPs are, on the surface and the ends of the nanowire. Polymer forms a thin film around the cylindrical side and big clusters at both the proximal and distal ends. SPs can couple onto adjacent metal nano-structures, for example, when another silver nanowire is deposited on (close to) the chosen nanowire, it can be glued or "welded" onto the original nanowire due to the polymerization. One can easily imagine that we can build complicated structures following these procedures, depending on our ability to manipulate the "building bricks" (different nanostructures).

3.4 Conclusions

Our simulation results demonstrate that the nanowires can be treated as efficient Fabry-Perot resonators. We proposed a way to directly simulate the plasmon dispersion relation of Ag nanowire, with a convenient result: $\omega_{wire} = \omega_{sp}$.

The decay of the field perpendicular to the Ag nanowire is also calculated, and simulated to be in agreement with the well-known results of Takahara et al (1997). Besides demonstrating agreement with classic theory and experimental results, our research provides important information on plasmonics in one dimensional structures, and guides future research on the applications in many different fields such as: surface plasmon channeling, nano-transmission lines, nano-circuit building [Assefa et al, 2010], and nanostructure fabrication [Nah et al, 2010] etc. The interaction between Ag nanowire and other nanostructures are also simulated and analyzed to serve as confirmation and guidance for experiments to build nanophotonic devices, experimental results of which have been submitted for publication [Nah et al, submitted].

Chapter 4

Nanocoaxial waveguide

In this chapter, we study propagation of electromagnetic waves in a single nanocoaxial waveguide for frequencies around and below the surface plasmon frequency. We show, that for frequencies sufficiently lower than the surface plasmon frequency, the waveguide supports a plasmon polariton mode that resembles, and indeed reduces to the conventional transverse electromagnetic (TEM) mode of the conventional coaxial transmission line, known in radio technology. Some of the results presented in this chapter are published [Yun et al, 2008].

4.1 Introduction

Commonly used optical waveguides, of which optical fiber is the most common one, have been used in several applications, including telecommunication and optical sensing [Midwinter, 1971; Monro et al, 2001; Okamato, 2000]. Conventional optical waveguides are usually limited by the diffraction limit: $\sim \lambda / 2n$ [Lamprecht et al, 2001; Pile & Gramotnev, 2004], where λ is the wavelength, and n is the refraction index number of the waveguide. This means the minimal size of a conventional waveguide is limited to $\sim \lambda / 2n$, below which the waveguides have very poor, if any, ability to transmit light [Lee et al, 2000, Yariv & Yeh, 1984].

There are many ways to transport light more efficiently; and to be able to transmit light in a large range of frequency (wavelength) is one of the challenges. The idea of a nanocoaxial transmission line, known in the radio technology, is examined. A coaxial cable (as shown previously in Fig. 2.1), constructed with a metal core, some dielectric cladding and a metal shell, is a good candidate to transmit TEM waves without having a cutoff frequency. Actually coaxial cables are already in our daily life, transmitting electromagnetic signals for our radio, television, phone and internet. Can we adapt the ideas from radio technology to the optical regime? Will light behave the same way, given the complexity of the plasmonic phenomenon?

Recently, transmission of visible light through nanoscopic, coaxial transmission lines based on carbon nanotubes, has been demonstrated [Rybczynski et al, 2007]. The light propagates, without any frequency cut-off, along narrow channels much thinner than the light wavelength (λ), and over large distances much larger than λ. This resembles the transmission of radio-waves through the conventional coaxial cable [Pozar, 2005] via its basic mode, the transverse electromagnetic (TEM) wave, which does not possess any cut-off frequency (i.e. it is gapless).

In this chapter, we demonstrate theoretically, that a metallic nanocoax indeed supports a gapless polaritonic mode, the 0th order transverse magnetic (TM_0) mode, which for frequencies sufficiently lower than the surface plasmon frequency of the metal, resembles, and for much smaller frequencies, reduces to the text-book TEM coax mode. This allows for a "radio engineering" treatment of the light propagation through nanocoaxial transmission lines, involving, for example, an impedance analysis for the line matching and coupling [Pozar, 2005]. While the dispersion of the gapless polaritonic mode has been calculated by various authors such as Kushwahal and Djafari-Rouhani (2003, 2005), Ancey et al (2004), Baida et al (2006), Garcia and Bai (2006), and Takahara et al (1997), its detailed character in the low frequency limit has not been identified.

4.2 NanoCoax study

4.2.1 Analytical approach

We begin with a standard analytical approach, based on matching solutions of the Maxwell's equations (in cylindrical coordinates) across the nanocoax interfaces. This approach has been commonly used in the theory of fiber optic transmission lines. In the case of the nanocoax, the difference is the presence of metallic regions, in which the dielectric function is a strong function of frequency, and below the plasma frequency becomes negative. Optics of such systems, with "negative dielectrics", were investigated in general by Takahara et al (1997), and a "gapless" mode was referred to as a "one dimensional (1D) optical wave". We call it a "TEM-like" mode.

The geometry of the coaxial waveguide is shown in Fig. 2.1. With the assumption that both conductors of the coaxial cable are made of the same, nonmagnetic metal described by the Drude dielectric function

$$\varepsilon_1 = \varepsilon_3 = \varepsilon_b - \frac{\omega_p^2}{\omega^2 + i\omega\gamma}$$

A dielectric material, with dielectric constant ε_2, fills the space between the conductors. All fields are assumed to be transverse, and $\propto \exp[i(k_z z - \omega t]$, where k_z is the z-component of the wave vector.

The details of solving the Maxwell's equations analytically are given in the previous chapter. The achieved dispersion relation equation is rewritten here

$$\left(K_0(k_2 b)\frac{I_0(k_2 a)}{I_0(k_2 b)}\frac{\varepsilon_1}{k_1}\frac{I_1(k_1 a)}{I_0(k_1 a)} - \frac{\varepsilon_2}{k_2}K_1(k_2 a) - K_0(k_2 a)\frac{\varepsilon_1}{k_1}\frac{I_1(k_1 a)}{I_0(k_1 a)} - K_0(k_2 b)\frac{\varepsilon_2}{k_2}\frac{I_1(k_2 a)}{I_0(k_2 b)} \right)$$
$$\times\left(-\frac{\varepsilon_3}{k_3}K_1(k_3 b) - K_0(k_3 b)\frac{\varepsilon_2}{k_2}\frac{I_1(k_2 b)}{I_0(k_2 b)} \right)$$
$$-\left(K_0(k_3 b)\frac{\varepsilon_2}{k_2}\frac{I_1(k_2 a)}{I_0(k_2 b)} - K_0(k_3 b)\frac{I_0(k_2 a)}{I_0(k_2 b)}\frac{\varepsilon_1}{k_1}\frac{I_1(k_1 a)}{I_0(k_1 a)} \right)\left(\frac{\varepsilon_2}{k_2}K_1(k_2 b) + K_0(k_2 b)\frac{\varepsilon_2}{k_2}\frac{I_1(k_2 a)}{I_0(k_2 b)} \right)$$
$$= F(\omega, k_x) = 0 \quad , \qquad (2.6)$$

where $k_m = \sqrt{k_z^2 - (\omega/c)^2 \varepsilon_m}$, $m = 1,2,3$, and I_n, K_n are the n th-order modified Bessel functions of the first and the second kind, respectively.

To evaluate the solutions to Equation (2.6), we chose a nanocoax made of silver, a low loss metal, which also is known to have negligible, non-local, quantum mechanical corrections [Wang & Kempa, 2007]. The Drude parameters of silver are $\hbar\omega_p = 9.9ev$, $\hbar\gamma = 0.04ev$, and $\varepsilon_b = 6.8$ [Wang & Kempa, 2007].

Results for other metals are similar if properly scaled in plasmon units (i.e. by expressing the frequency as ω/ω_p , and the damping parameter as γ/ω_p). For simplicity, we also assume that $\varepsilon_2 = 1$. It is clear from Equation 2.6, that only ratios of dielectric functions are relevant, and thus changing the value of ε_2 is a simple simultaneous scaling of the parameters k_z, ω, $1/a$ and $1/b$. We chose the following nanocoaxial dimensions: $a = 50nm$ and $b = 150nm$.

Numerical solutions of Equation 2.6 are shown in Fig. 4.1 and represented as crosses. The mode is gapless, with a linear (acoustic) dispersion for small frequencies (see Fig. 4.1). In fact, it is a plasmon polariton, a hybrid of photons and plasmon excitation, exactly like its slot waveguide "cousin" [Wang & Kempa, 2007]. The imaginary part of k_z, the inverse of which is the TEM-like mode propagation length L, is shown in Fig. 4.2. There is a plateau for frequencies above γ, and well below the renormalized plasma frequency ($\overline{\omega}_p = \omega_p/\sqrt{\varepsilon_b} = 3.8eV/\hbar$), where $\mathrm{Im}(k_x)$ ranges from $0.00005nm^{-1}$ to $0.0001nm^{-1}$, which corresponds to $L = 1/\mathrm{Im}(k_x)$ ranging from $20\mu m$ to $10\mu m$. This is in agreement with the experimental results of Rybczynski et al (2007). For frequencies approaching $\overline{\omega}_p$, $\mathrm{Im}(k_x)$ rapidly increases (and so L decreases). This is characteristic of the plasmonic domain, and reflects increasing losses due to the EM energy entering the metal as plasma waves. The inset in Fig. 4.2 shows the dispersion for very low (below γ) frequency domain. The solid line is for the TEM-like mode, and the dashed curve is for

the TEM mode of a classic, macroscopic coaxial cable, given by the textbook formula [Pozar, 2005]

$$\mathrm{Im}(k_z) = \frac{1}{2\sigma\delta}\sqrt{\frac{\varepsilon_0}{\mu_0}}\frac{(1/a+1/b)}{\ln(b/a)} = \frac{1}{2\omega_p\sqrt{2}}\frac{(1/a+1/b)}{\ln(b/a)}\sqrt{\gamma\omega} \qquad (4.1)$$

where σ is the static conductivity of the metal, and δ is the penetration depth.

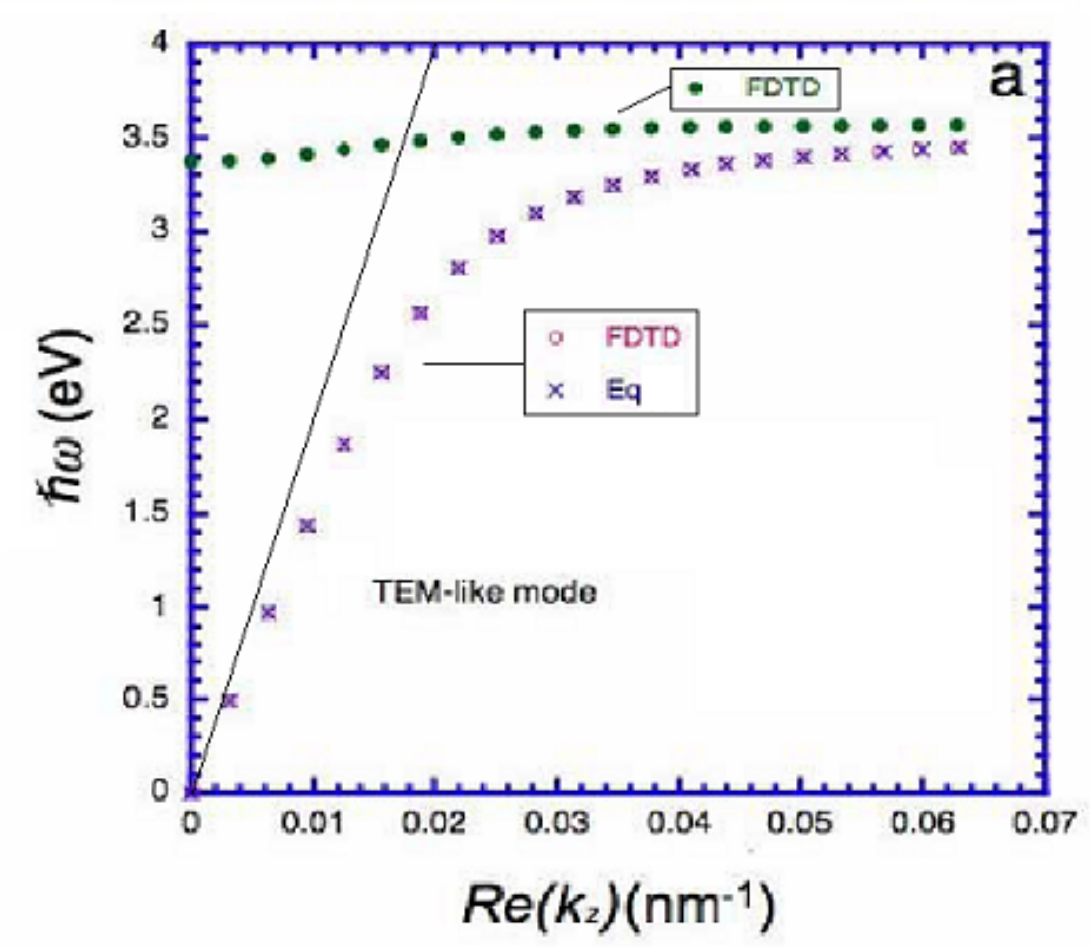

Fig. 4.1. Dispersion of the selected nanocoax modes. Frequency ω (real) vs real part of the wave vector k_z. "TEM-like" mode dispersion is represented by crosses (from Equation 2.6), and open circles (FDTD calculation). The solid circles represent dispersion of the plasmonic gapped mode.

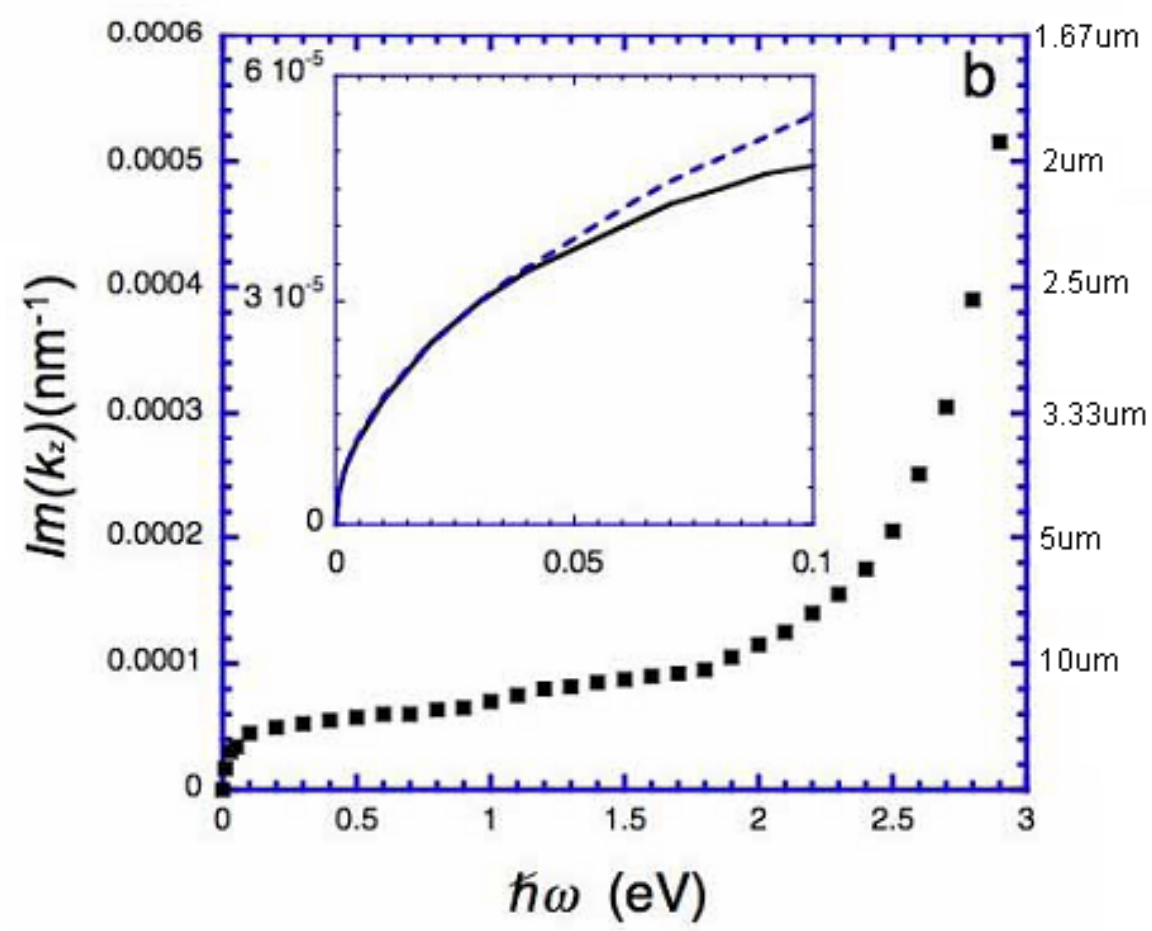

Fig. 4.2 Dispersion of the selected nanocoax modes. Imaginary part of k_z vs ω for the TEM-like mode (solid squares) obtained from Equation (2.6). The inset is the zoomed-in section of this curve for very small ω, with solid curve from Equation (2.6), and dashed from the formula for macroscopic coax (Equation 4.1).

From Fig. 4.2, it is clear that for $\hbar\omega < 0.03eV$, the dependence of the damping constant on frequencies for the "TEM-like" mode is indistinguishable from that for the classic TEM mode (given by Equation 4.1). Simultaneously, in this frequency range, the dispersion of the "TEM-like" mode is purely "acoustic" (see Fig. 4.1). There is a ~ 36% reduction of the slope of this "acoustic" section (i.e. reduced velocity), as compared with the light propagating in free space (velocity equal to speed of light). This renormalization of the light-line dispersion is well known [Baida et al, 2006; Takahara et al, 1997; Wang & Kempa, 2007]. The effect that the dispersion relation deviates from the "light line" is negligible for gap dimensions much larger than the penetration depth δ of light into metal (conventional coax), but is significant in the nanocoax. Apart from this renormalization of the mode velocity, the "TEM-like" mode dispersion relation (both for real and imaginary wave vector) in the acoustic section is identical to that for the classical TEM mode of the conventional coax.

From Fig. 4.2, one can also see that in the low frequency range (roughly from 0 to 2 eV), the damping constant $\mathrm{Im}(k_z)$ is small, below $0.0001nm^{-1}$. This translates into long propagation length of ~ 10 μm. Similar phenomena were observed in nanostrip line [Dionne et al, 2006]. On the other hand, in the plasmonic regime, i.e. when the frequencies approaching the surface Plasmon frequency ~ 3.5 eV, the propagation length quickly reduces to ~ 1 μm.

4.2.2 Numerical approach

To further develop this problem, we have performed computational simulations of the fields inside the nanocoax using the FDTD method, described in detail in the first chapter. This method allows us to calculate the mode structure of all modes for real k_z. Our results are consistent with the results obtained Baida et al (2006). The circles in Fig. 4.1 show the dispersion of the "TEM-like" mode obtained in our simulation, in perfect agreement with the solution of Eq. 4.1. In addition, a branch of a higher, surface plasmon guided (gapped) mode [Baida et al, 2006] is also shown as solid circles in Fig. 4.1.

Figure 4.3 shows color maps representing radial components of the electric field (E_ρ) inside the nanocoax for the two modes of Fig. 4.1. On the left is for the "TEM-like" mode, and right for the gapped mode. In each plot the color intensity is proportional to the field amplitude, and color change represents the field sign (direction) change. Both maps are obtained for $k_z = 0.005 nm^{-1}$, so that according to Fig. 4.1, the "TEM-like" mode has frequency $0.98 ev/\hbar$, and the gapped mode $3.4 ev/\hbar$. The gapped mode is in the plasmonic domain, which results in a lot of penetration of fields into metal, clearly visible in Fig. 4.3. In contrast, the fields of the low frequency "TEM-like" mode have a marginal penetration into metal. The plot in Fig. 4.3 shows E_ρ (solid line) and ρE_ρ (dashed line) vs ρ. Since ρE_ρ is essentially constant, it must be that $E_\rho \sim 1/\rho$, which is precisely the form for the classical TEM mode for conventional coax [Pozar 2005].

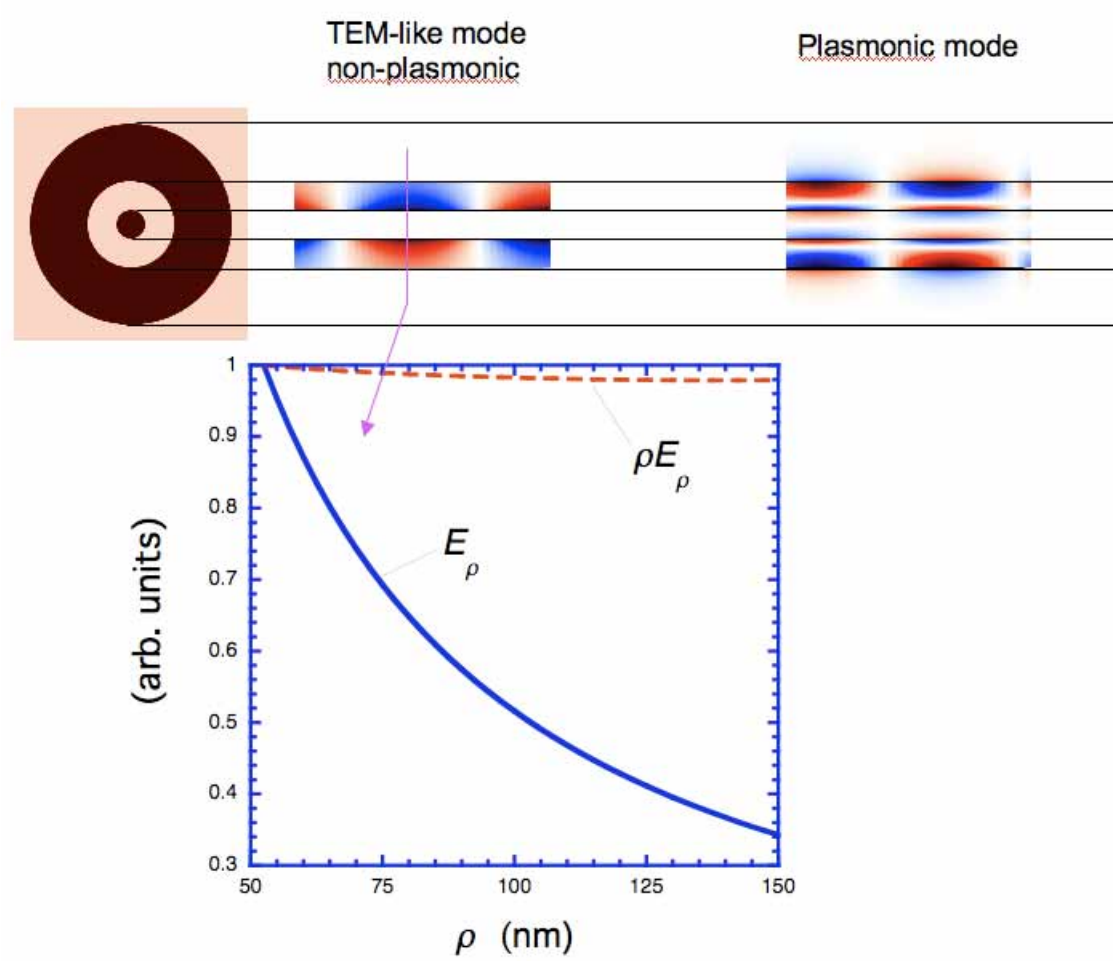

Fig. 4.3 Distribution of the electric field E_ρ inside the nanocoax for the two modes of Fig. 4.1. The left distribution is for the "TEM-like" mode, and the right for the plasmonic gapped mode. The color intensity is proportional to the field amplitude, and color represents the sign (field direction). $k_z = 0.005nm^{-1}$. The inset shows E_ρ vs. ρ (solid line), and ρE_ρ vs. ρ (dashed line).

4.3 Conclusion

In conclusion, we have investigated the propagation of electromagnetic waves in a coaxial nanowaveguide made of silver. We show, that for frequencies sufficiently lower than the surface plasmon frequency, but still in the infrared or visible ranges, the waveguide supports a plasmon polariton mode, the "TEM-like" mode, that resembles and indeed reduces to the conventional TEM mode of the conventional, macroscopic coaxial transmission line, known in the radio technology. This gapless mode is capable of transmitting electromagnetic waves with wavelengths far exceeding the coax diameter, and therefore allows for truly nanoscopic dimensions of the nanocoax transmitting light waves. For light of lower energy (under ~3eV), the propagation length is on the micrometer scale, long enough for nanowires to be used in nanophotonic applications such as nanoplasmonic circuits. Existence of this TEM-like mode was demonstrated experimentally in the work of Rybczynski et al (2007). The nanocoax operating with the "TEM-like" mode will enable numerous potential applications in the nanooptics.

Chapter 5

Plasmonics of thin film quasi-triangular nanoparticles

In this chapter, we investigate optical responses of arrays of flat, quasi-triangular nanoparticles. Our simulationed optical absorption spectra show strong, particle-size dependent resonances, in excellent agreement with the experimental results. We identify those resonances as due to standing surface/edge plasmon-polariton waves. Some of the work presented in this chapter is published [Yun et al, 2010].

5.1 Introduction

Arrays of flat, quasi-triangular gold nano particles can be made by self-assembly sphere lithography (SSL) on a 20 nm thick gold film. Our German collaborators (Patoka, P., Hilgendorff, M., and Giersig, M.) made these arrays, and the measured optical absorption spectra show strong, particle size dependent resonances. In this chapter, we investigate and simulate the optical responses of these nano particle arrays and find that our simulation results in excellent agreement with the measured results. We show that these structures have the characteristics of resonant electromagnetic spectra due to surface/edge plasmon resonances.

5.2 Experiment

The details of the SSL process can be found in our publication [Peng et al, 2010]. This technique employs a hexagonal array of removable polystyrene spheres (PS) self-assembled on a sapphire substrate. These spheres, in turn, act as a shadow mask for the subsequent metal evaporation [Kandulski, 2007; Koisirek et al 2004]. The resulting pattern is that of a honeycomb array of quasi-triangular thin film gold nanoparticles. The

sphere diameters, and thus the dimensions of the nanoparticles can be controlled over a wide range. The top panel of Fig. 5.1 are the SEM pictures, done by Dr. Ren's group, showing SEM images of the substrate deposited with PS (left) and the quasi-triangles after deposition of metal and removel of PS (right). The bottom panel of Fig. 5.1 is an atomic force microscope (AFM) image of such an array, with the colored scanning electron microscope (SEM) image of single ring of nanoparticles in the inset. By using different PS diameters the overall planar scale of the array can be changed, including sizes of the individual nanoparticle.

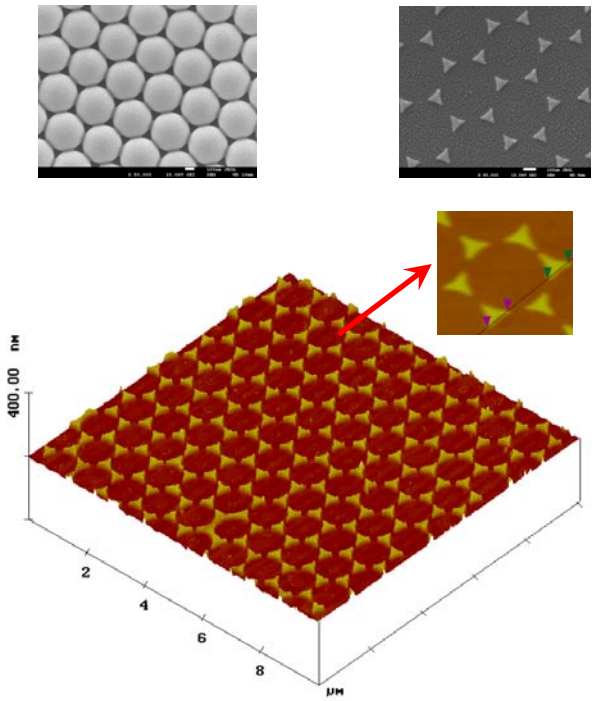

Fig. 5.1 The top panel shows the SEM image of the substrate deposited with PS (left) and the quasi-triangles after deposition of metal and removel of PS (right). The bottom image is an AFM image of an array of gold quasi-triangles, obtained by using SSL. The inset shows SEM of a single ring of nanoparticles.

The experimental results, obtained by our German collaborators, of the absorbance over the spectra are shown in the top panel of Fig. 5.2. The results are for structures obtained with sphere diameters a = 380, 540, 980, and 1710 nm (peaks from left to right, correspondingly). The absorbance is in arbitrary units. As we can see, each spectrum is dominated by a pronounced resonance peak, the position of which strongly depends on *a*. In addition to the main peaks, smaller peaks are also visible.

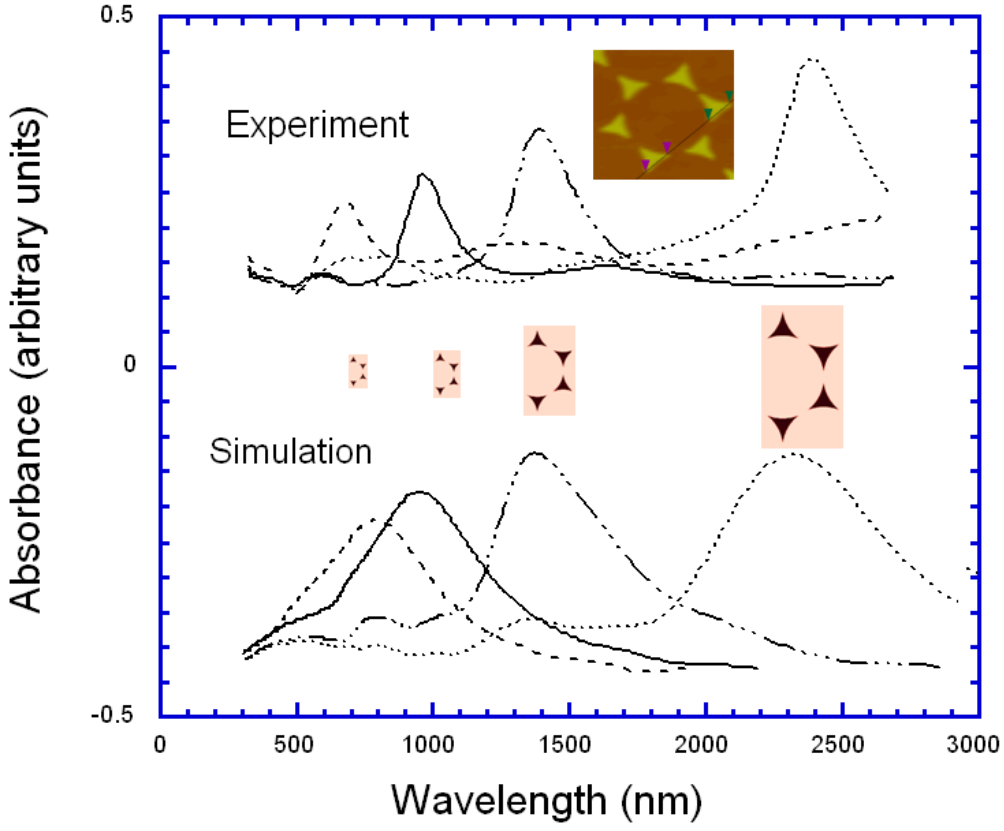

Fig. 5.2 Absorbance (in arbitrary units) of quasi-triangle arrays measured (top), and simulated (bottom), for the SSL sphere diameters *a* = 380, 540, 980, and 1710 nm: peaks from left to right respectively. Inset shows the FDTD unit cells of the array.

5.3 Simulations

The simulation methods and tools we use are similar to the ones described in previous chapters. To make a model of the nanostructure, we simulate making air holes on a thin gold film. By controlling the diameter of the holes, we are able to control the size of these quasi-triangular nanoparticles. We have tried the holes, corresponding to those removable PS in the experiments, of diameters a = 380, 540, 980, and 1710 nm. Since the diameter is, in the cases of this chapter, also defined as the distance from the center of one hole to that of the other, we basically achieve a set of quasi-triangles that are geometrically the same yet proportional in size. Fig. 5.3 illustrates how the modeled structures look.

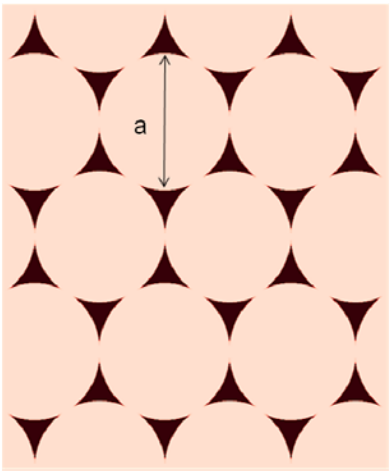

Fig. 5.3 Illustration of the gold quasi-triangle structures used in the simulations, with hole diameters a = 380, 540, 980, and 1710 nm.

We simulate the absorbance of the structures illustrated in Fig. 5.3. The results are show in the bottom panel of Fig. 5.2. As one can see, the experiment and simulation results are in good agreement.

According to Mie theory [Kempa, 2006], the surface plasmon of spherical metal nanoparticles is circumferentially quantized. The electromagnetic response of metallic clusters of any shape can be viewed as due to circumferentially quantized surface plasmon waves, which requires that an integer multiple of the wavelength of the wave equals the nanoparticle circumference [Kolwas, 1998; Brechignac & Connerade, 1994]. Fig. 1.4 in chapter 1 illustrates an easy way to understand this concept. It is expected that the resonances we observed are also from a highly dispersive plasmon-polaritonic mode that is very similar to the resonances in the metallic clusters.

To investigate further, we assume that these resonances (as well as the higher order resonances that are also visible in Fig. 5.2) can be viewed as circumferentially quantized surface plasmon waves. We ignore for the moment particle-particle interactions. Since each side of the quasi-triangular particle equals approximately 1/6 of the sphere circumference πa, so the circumference of the particle is $\sim \pi a/2$. Thus the circumferential quantization condition requires that this circumference be equal to an integer multiple of the wavelengths of the resonating surface/edge plasmon wave (λ_p), so we have

$$l\lambda_p \approx \frac{\pi a}{2} \approx 1.5a\,, \qquad (1)$$

where $l = 1,2,3$ are for first (main peak), second, and third order resonances, respectively. This relation gives straight line as shown in Fig. 5.4. The absorbance peaks, shown in Fig. 5.2, seem to be quantized. For a quantitative study, we plot, for each hole size, positions of the peaks $\lambda_{\max}$ as a function of a. The results are shown in Fig. 5.4. squares represent the main peaks (black for experiment, and white for the simulations, both from Fig. 5.2). White circles represent simulation of the main peak position for a single quasi-triangle. Correspondingly the secondary peaks maxima locations are shown in Fig. 5.4 as identical, but subsequently smaller symbols.

The fact that the single quasi-triangle (circles) dependency is essentially identical to that for the array of triangles, shows that the inter-particle interactions play a secondary role (we will return to this point later). For large a, all the data asymptotically approach straight lines $\lambda_{\max} = 1.5a/l$ (l = 1, 2, 3). In fact, the main peak data follow this dependency for $l = 1$ rather well in the whole range of a.

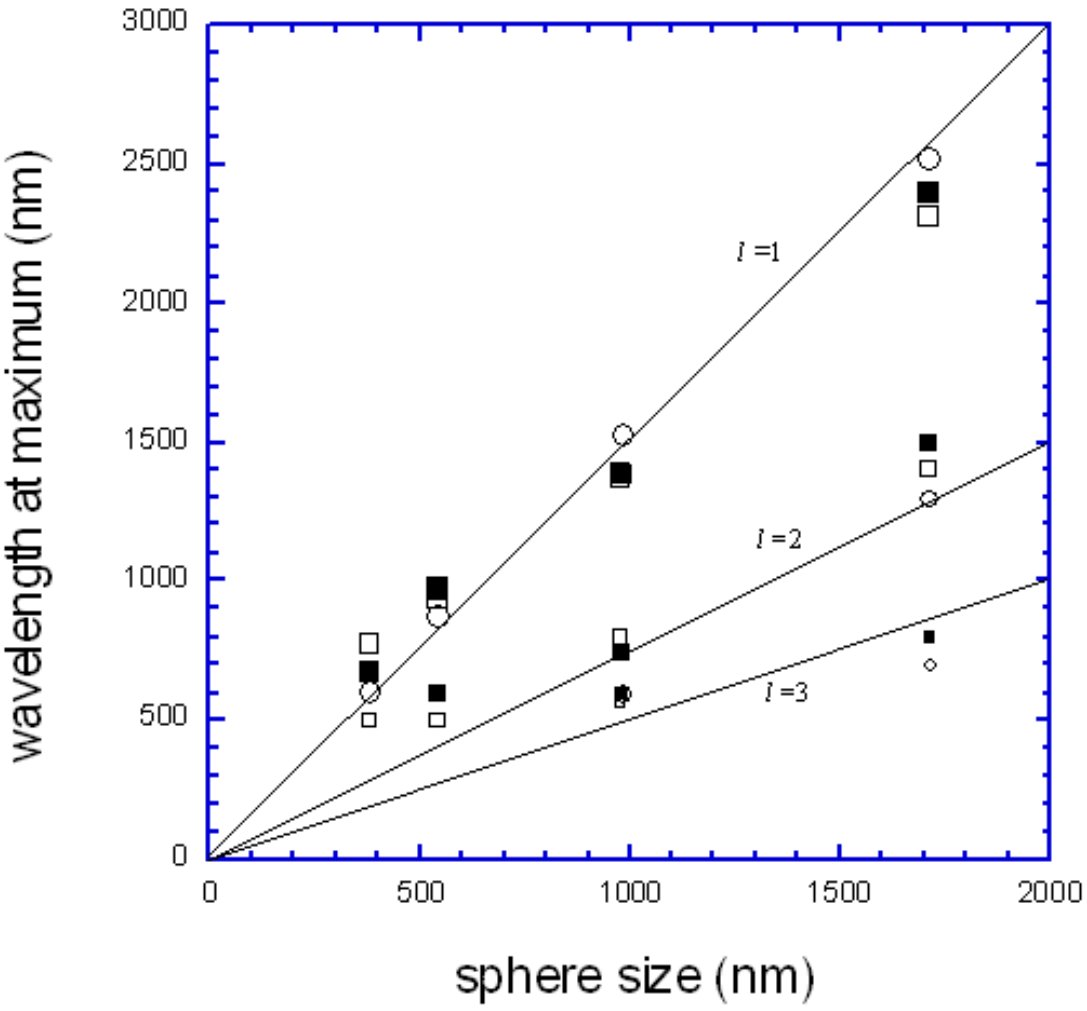

Fig. 5.4 Absorbance peak positions λ_{max} as a function of a. Squares represent the main peaks (black for experiment, and white for the simulations). White circles represent simulation of the main peak position for a single quasi-triangle. For $l = 2,3$ the same symbols, except correspondingly smaller, are used. Solid lines are generated by using $\lambda_{max} = 1.5a/l$ ($l = 1,2,3$).

To get a better understanding of the physics, we plot the data another way as shown in Fig. 5.5. It shows the resonating mode dispersion, plotted as $\omega n/2\pi = 1/\lambda_{\max}$ versus $q/2\pi = 1/\lambda_p$, obtained by using Eq. (1) to define λ_p and the data shown in the inset to define $\lambda_{\max}$ (wavelength at a peak), for the corresponding a and l. Here we use n for the effective refractive index of the medium surrounding the nanoparticles (of order 1).

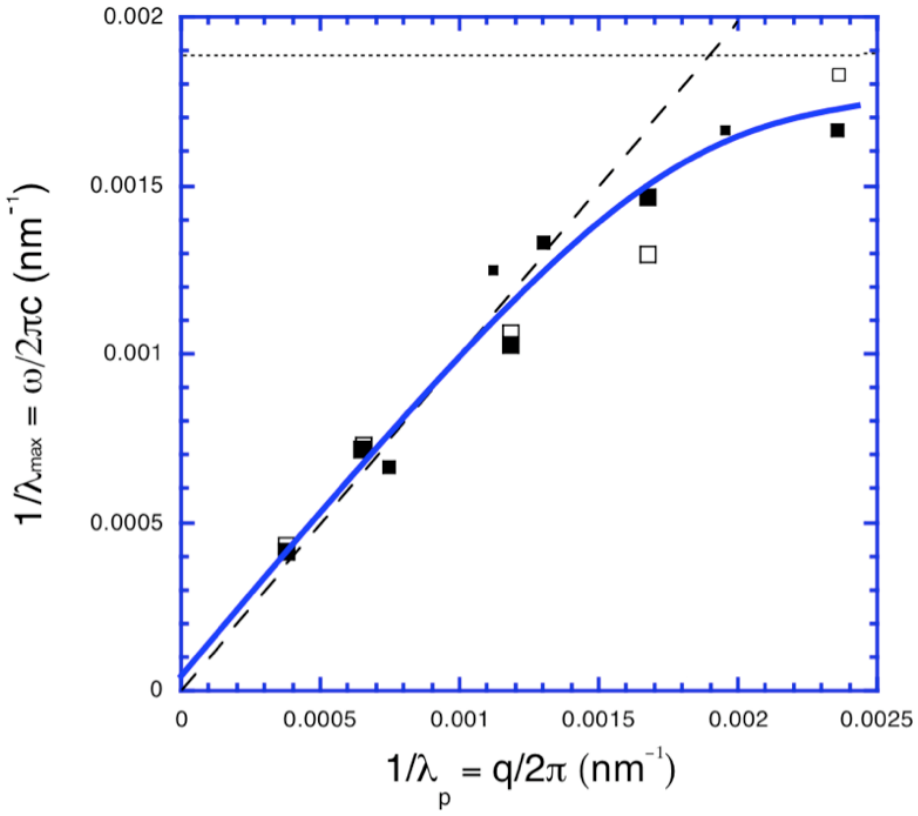

Fig. 5.5 Dispersion of the resonating surface/edge plasmon in an array of quasi-triangle nanoparticles. Black squares represent the experiment (all orders), and white squares the simulation. The square sizes decrease for $l = 1,2,3$, respectively. The dashed line is the light line, and the solid line is a fit to the data. The horizontal dashed line represents the Mie resonance for nanoparticles.

All data, for three orders (encoded as white squares of diminishing sizes for $l = 1,2,3$, correspondingly), congregate around a single line (solid blue line), drawn here as a guide to the eye, confirming that all the resonances belong to a single mode. In addition to the simulations that we have performed, based on the FDTD computational scheme, we also show the experimental data in the plot as black squares. The agreement between simulations and experiment is clearly good, in particular regarding the peak maxima locations, most of which overlap, or at least fall within the standard deviation of the same order as that for the experimental results. Even the line shape of the simulated spectra (the bottom panel in Fig. 5.2), the most difficult feature of the spectral response to reproduce, compares well to the corresponding experimental results (the top panel in Fig. 5.2), except for the peak width, which for purely numerical reasons is larger for the simulated spectra [Note 1]. The dashed line in Fig. 5.5 represents the corresponding light line (photon dispersion): $\omega = qc / n\,\omega$, or simply $1/\lambda_{\max} = 1/\lambda_p$. Clearly, the surface/edge plasmon mode in our nanoparticles follows the light line for wavevectors $q < 0.008 nm^{-1}$. This is the retarded, or polaritonic regime, in which the mode is a photon-plasmon hybrid (plasmon polariton) [Wang & Kempa, 2005].

For large wavevectors $q > 0.008 nm^{-1}$ (non-retarded regime), the dispersion deviates from the light line. This is due to the presence of the Mie resonance [Mie, 1965; Vandenbem & Vigneron, 2005; Scharte et al, 2001], which results from the center of mass (collective motion of the electron gas) oscillating in the confining potential of the positive ions. To

lowest order, this potential is parabolic, with the single electron eigenfrequency ω_0. It has been shown [Brey et al, 1989; Bakshi et al 1990], that in such circumstances the long wavelength, non-retarded response of the system, is dominated by a single resonance at $\omega_s = \omega_0$, regardless of the electron-electron interactions (generalized Kohn's theorem [Kohn, 1961; Kempa, 2006]). For a spherical nanoparticle made of a simple metal with bulk plasmon frequency ω_p, the Mie resonance is $\omega_s = \omega_p / n\sqrt{3}$ [Kempa, 2006]. For complex metals, such as Au or Ag, the resonant condition is modified and leads to $n\omega$ much closer to the corresponding bulk plasmon frequency [Brechignac & Connerade, 1994]. The dotted horizontal line in Fig. 5.5 is the measured Mie resonance for ultra-small Au particles [Note 2], in an environment with a refractive index that is similar to the one in our structures [Scaffardi & Tocho, 2006]. The saturation frequency for our quasi-triangles is of the same order.

Now, we will go back to the discussion about the difference between quasi-triangle arrays and a single quasi-triangle. Fig. 5.6 compares the dispersion for the arrays to that from a single quasi-triangle. In the retarded range, both dispersions follow closely the light line, showing that the inter-particle interaction is negligible in this range. In the non-retarded range, in contrast to the array dispersion, the dispersion for a single quasi-triangle follows the light line for all q's available here. This shows that the Mie resonance frequency for an array is lower than that for a single particle from this array. This inter-particle effect has been predicted in Ref. [Kempa, 2006], and is the result of the Coulomb contribution

of ions in the neighboring nanoparticles, which softens the parabolic confinement inside a particle, and thus reduces ω_0 and consequently ω_s, for arrays of nanoparticles.

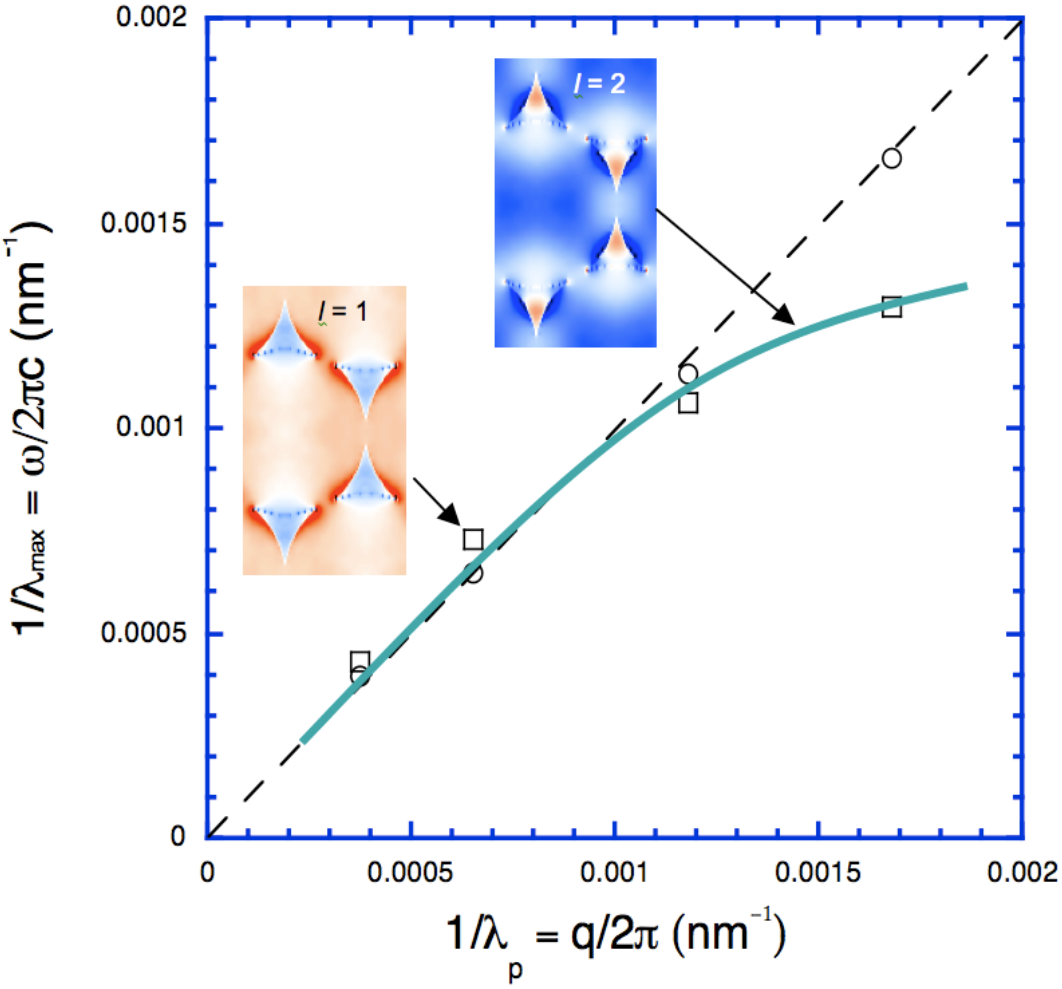

Fig. 5.6 Comparison of the simulated dispersions for arrays (white squares), and for a single quasi-triangle (white circles). The dashed line is the light line, and the solid line is a fit to the array data. The simulated color maps of the field distribution in the arrays, for $l = 1,2$ resonances, are also shown as insets.

Finally, we show the simulated electric field distributions in the nanoparticles. The maps of the in-plane, horizontal electric field component for the main peak ($l = 1$), and a higher order resonance ($l = 2$), are shown as insets in Fig. 5.6. These field patterns are generated by a planar, horizontally polarized electromagnetic wave propagating in the direction perpendicular to the substrate surface. These field patterns are in good agreement with those observed experimentally in the Ag triangular nanoparticles in the work of Nelayah et al [2009], including tip localization of the electric field for the first order peak (the lightning rod effect), and a second order pattern (right) involving maxima located at the edges of the triangle between tips [Kirkland et al, 1990; Wang et al , 1999; Johnson et al, 2002; Jin et al, 2003; Chen et al, 2005; Lofton & Sigmund, 2005; Sanchez-Iglesias et al, 2006] [footnote: Note, that Au is similar to Ag.].

5.4 Conclusion

In conclusion, we have investigated the optical response of arrays of quasi-triangular gold nanoparticles, with different sizes, made by the self-assembly sphere lithography. Our simulated results are in excellent agreement with the experiment, and show that the physics is due to a surface/edge plasmon polariton resonating in the nanoparticles.

Chapter 6

Plasmonics of a perforated metallic film

In the previous chapter, I have studied how the optical responses of the quasi-triangle arrays change, with the holes' diameter and the "center to center" distance changing at the same time. Here we study how the optical response changes when we change the holes' diameter while fixing the "center to center distance" distance. The structure changes from a solid film to an array of holes, to an array of islands (as shown in Fig.

6.1). This transition resembles a percolation problem. The work in this chapter is partially published [Yun et al, 2010].

6.1 Introduction

In this chapter, we study interaction of the electromagnetic radiation with a series of thin film periodic nanostructures evolving from holes to islands. We provide such a study based on a series of nanostructures, in the plasmonic frequency range. We show, through model calculations and simulations, together with experimental results, that the responses (polaritonic effects) of these structures evolve accordingly, with two topologically distinct spectral types for holes and islands. We find also, that the response at the transitional pattern is singular. We show that the corresponding effective dielectric function follows the critical behavior predicted by the percolation theory, and thus the hole-to-island structural evolution in this series is a topological analog of the percolation problem, with the percolation threshold at the transitional pattern.

Percolation theory studies the connected clusters in a random graph. Percolation theory was first introduced into a physics problem by Broadbent and Hammerskey (1957) as below: Imagine some liquid is being poured on top a piece of amorphous material, the question is will the liquid make its way from the top and drip out of the bottom? The

main idea of percolation theory is to find a percolation threshold, often being defined as the critical probability of the "degree of connectivity" [Zalen, 1983] or a parameter value at which the phase transition takes place [Kesten, 2006]. Below the threshold, the system is viewed as isolated holes; and above it, the system becomes "connected". The "global behavior" is very different on either side [Kesten, 2006]; the percolation threshold is the point where the phase transition or critical phenomenon happens.

Percolation theory has been used to explain the physical behavior in heterogeneous systems, such as forest fires [Drossel & Schwabl, 1992], the refill of an oil well [King et al, 2001; Stauffer, 2001], and electric resistance of a mixture of conductor and resister [Grimmet, 1999]. In this chapter, we study the optical response of nanostructure transitions and find it helpful to use percolation theory.

6.2 Simulations

Let us consider making a series of hexagonal arrays of circular air holes in a thin metallic film. The hole diameter d changes from 0 to a, and beyond, while the lattice constant (nearest neighbor inter-hole distance) remains fixed at a throughout the series. The unit cells of the arrays are shown in Fig. 6.1. The pattern changes gradually from the solid

film, to hexagonal arrays of circular holes of increasing diameter, to honeycomb arrays of disconnected quasi-triangular metallic islands (nanoparticles). Beginning from pattern 1 (solid film), the density of holes within the continuous metallic film grows until, at the transitional pattern 8 ($d = a$), the continuity of the film is interrupted.

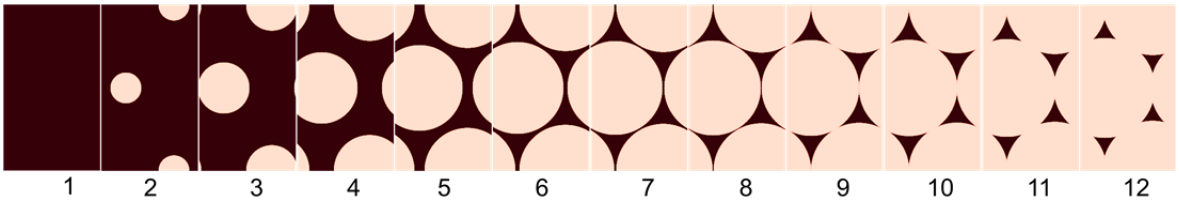

Fig. 6.1 The simulated structure: 20nm Au deposited on Sapphire. The unit cell is 470 nm x 814nm. Air holes are drilled in HCP symmetry. The lattice constant (the distance between two adjacent holes) of the hexagonal array of spheres a = 470 nm. Hole diameters are d = 0, 150, 250, 350, 420, 450, 460, 465, 470, 472, 480, 490 nm for patterns 1-12 respectively.

We chose Au as the metal, and the Lorentzian expansion of the Au dielectric function used in the simulations was fitted to the experimental data given in Ref. [Johnson & Christy, 1972]. The film thickness is chosen to be 20 nm, and the lattice period a = 470 nm. The substrate is glass. We begin with simulations of the electromagnetic response of these nanostructures based on the finite difference time domain (FDTD) computational scheme described in previous chapters. The transmittance spectra of each structure is calculated and shown below in Fig. 6.2. The number (1 to 12) identifies the

corresponding unit cells of the nanostructures shown in Fig. 6.1, and also attached next to the spectra for convenience.

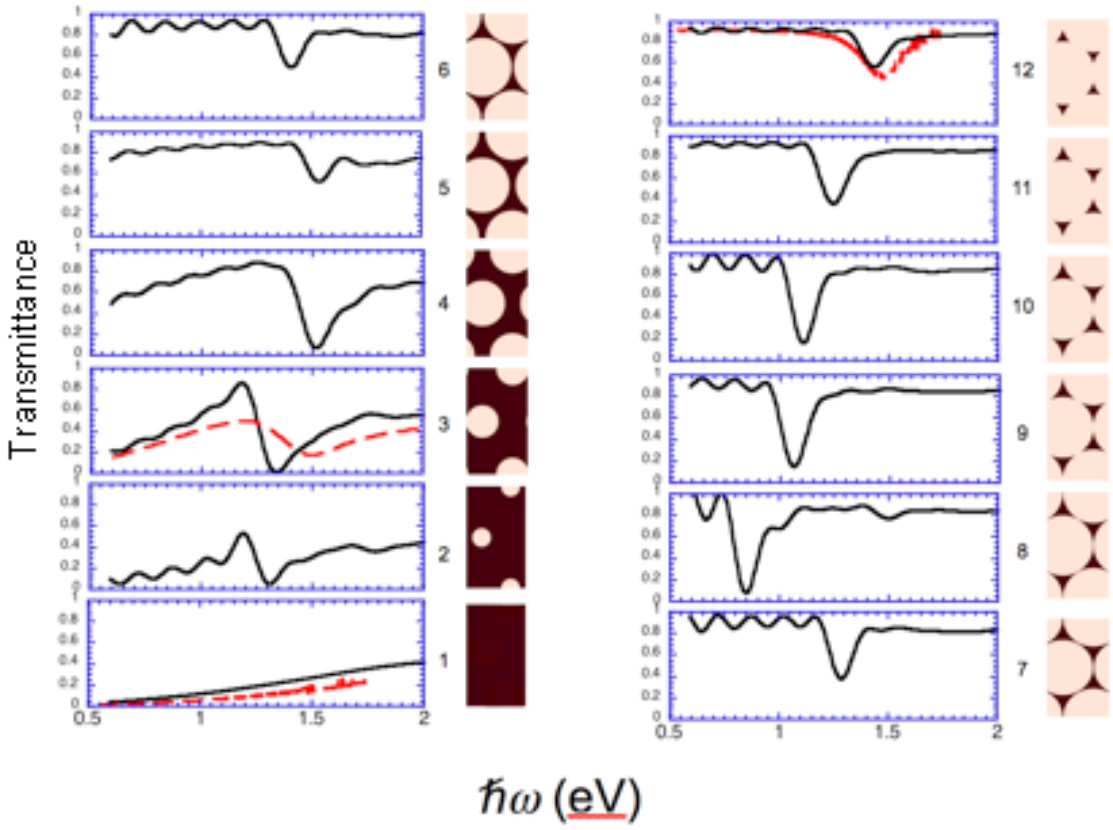

Fig. 6.2 FDTD simulated transmittance spectra (*Transmittance* vs $\hbar\omega$) for the twelve nanostructures. Pattern numbers (1 to12), and the unit cells of the corresponding pattern arrays are shown next to each corresponding spectrum. The unit cell for each pattern (from 1 to 12) is shown next to its transmittance spectra respectively.

In addition to the simulation, the collaborating team member has made and took measurements with selected structures from our series: the solid film (pattern 1), an array of holes (pattern 3), and array of nanoparticles (pattern 12). To make the structures self-assembly lithography was employed; the details were described in previous chapter. Fig. 5.1, also the inset of Fig. 6.3, shows SEM images of an array of polystyrene spheres (a), and the resulting quasi-triangle metallic island array (b). All patterns in the series can be made by thermal processing and reactive ion etching [Ctistis et al, 2007]. The experimental results for the selected patterns 12, 3 and 1 are shown as red dashed lines in Fig. 6.2, with their simulation counterparts, respectively. The results for the structure corresponding to pattern 3 have been published earlier [Ctistis et al, 2007].

These experimental results are also compared directly to the corresponding FDTD simulations, shown as solid lines in Figs. 6.3 (a), (b), and (c). The agreement between the experimental results and simulations (no adjustable parameters) is clearly good. The right panel, the plots (d), (e) and (f) in Fig. 6.3, are the results of theoretical calculation. The unit is arbitrary chosen for the theoretical model, and the shapes and key figures of the plots are to be compared with experimental and simulation results. The details of the theoretical calculation will be given in the following context.

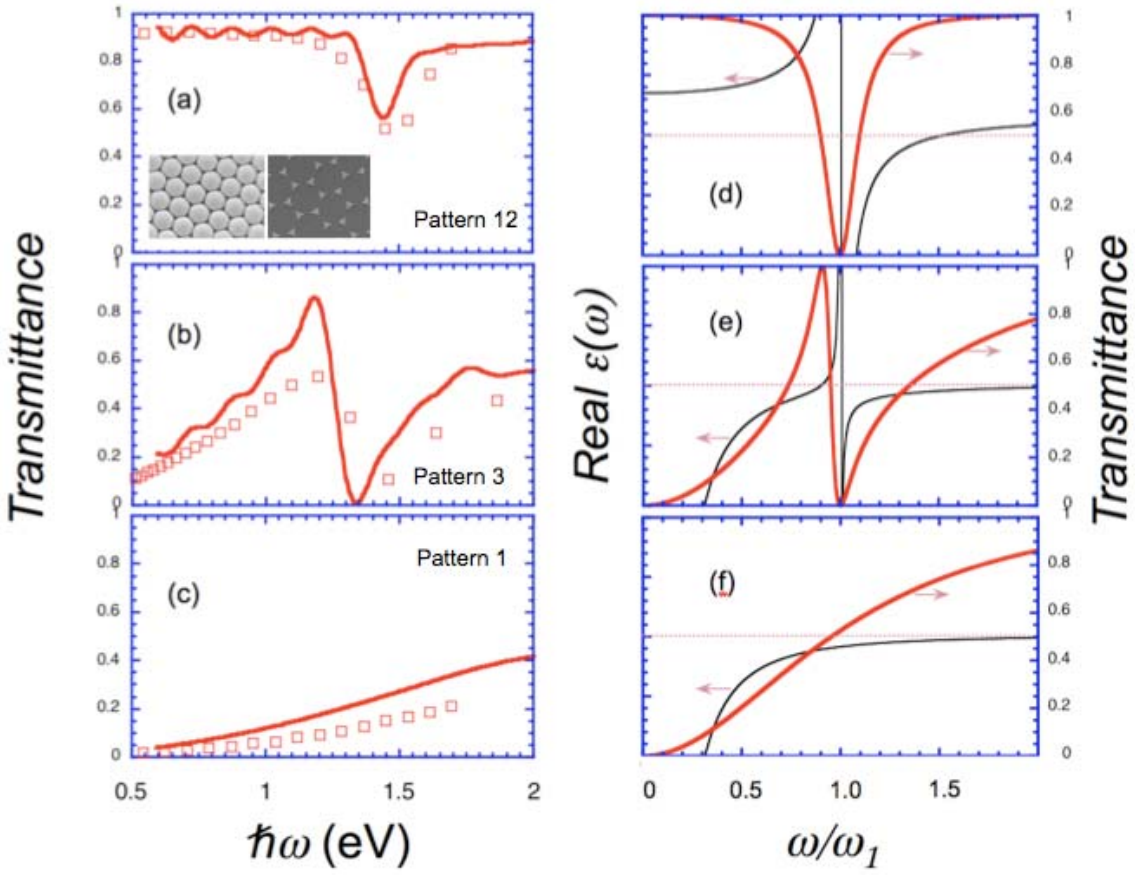

Fig. 6.3 (Color online) Left panel: FDTD simulated (solid line) and measured (open squares) transmittance spectra for selected patterns: (a), (b), and (c) for patterns 12, 3, and 1, respectively. Right panel: calculated ε [from Eqs. (1) and (2), thin black lines] and the corresponding transmittance *T* [from Eq. (4), bold red line] vs ω, for patterns 12 (d), 3 (e), and 1 (f). Real ε (ω) in (d), (e), (f) scales from −2 ε_b to 2 ε_b. Inset in Fig. 6.3 (a): SEM images of an hcp polystyrene sphere array (left image), and the resulting honeycomb island array (right image), bigger pictures are shown as Fig. 5.1.

6.3 Theory

The characteristics of these spectra can be easily understood by employing a simple, effective medium model [Kempa, 2006], based on the generalized Kohn's Theorem [Kohn, 1961]. The theory shows that an effective dielectric function of a system of isolated nanostructures is given by a sum of Lorentzian terms, each controlled by the single electron confinement in a specific nanostructure, produced by a uniform positive ionic charge. In the simplest case one obtains

$$\varepsilon(\omega) = \varepsilon_b + \frac{\omega_{p1}^2}{\omega_1^2 - \omega(\omega + i\gamma_l)} \ , \qquad (6.1)$$

where ε_b is the background dielectric constant; γ_l the losses; ω the frequency of the electromagnetic radiation; and ω_1 is the eigenfrequency of the confining potential (Mie resonance) [Kempa, 2006]. The corresponding dielectric function for holes is

$$\varepsilon(\omega) = \varepsilon_b - \frac{\omega_{p0}^2}{\omega(\omega + i\gamma_l)} + \frac{\omega_{p2}^2}{\omega_2^2 - \omega(\omega + i\gamma_l)} \ . \qquad (6.2)$$

The derivation is done by following the formalism in the work of Kempa (2006), and after noticing that the problem can be reduced to that of an array of complementary negatively charged islands, which attract positive effective carriers ("holes") instead electrons. This leads to the third term in Eq. 6.2, with ω_{p2} and ω_2 of the same order as ω_{p1} and ω_1, respectively. The second term in Eq. 6.2 (the Drude term), reflects existence

of unconfined electrons, which move freely along the structure (nonzero effective static conductivity σ_{eff}). A simple analysis shows that $\omega_{p0}^2 = 4\pi\sigma_{eff}\gamma_l$, with the effective static conductivity

$$\sigma_{eff} \sim (a - d) \ , \tag{6.3}$$

which vanishes at the transitional pattern ($d = a$). Equations 6.1 and 6.2, which can be justified by a variety of other methods, are consistent with the extracted dielectric functions for various heterogeneous metal-dielectric systems, including composites [Kempa et al, 2005], and meta-materials [Zentgraf et al, 2007; Chen et al, 2007].

With the dielectric functions defined, the transmittance formula [Heavens, 1965] for the effective thin film (assuming for simplicity $\gamma_l = 0$) is

$$T = \frac{1}{1 + \alpha^2\omega^2[1 - \varepsilon(\omega)]^2} \ , \tag{6.4}$$

where $\alpha = d/2c$ ($\alpha^2\omega^2 << 1$), and c is the speed of light.

The dielectric functions (given by Equations 6.1 and 6.2, with arbitrarily chosen parameters), and the corresponding transmittances for the selected patterns are shown on the right panel in Fig. 6.3. There are two, topologically distinct spectral forms: first for islands Fig. 6.3 (d), and the second one for the holes Fig. 6.3 (e). The solid film form of Fig. 6.3 (f) belongs to the second type, but without the resonance. For the second type structures $T \sim \omega^2$ for $\omega \to 0$, according to Eq. 6.4. This is in full qualitative agreement

with spectral features seen in the simulations and experiment in the corresponding Fig. 6.3 (a), (b) and (c).

Simulations for all patterns reveal the critical behavior of the response, and of the dielectric function, at the transitional pattern. This is clearly demonstrated in Fig. 6.4, which shows positions of the minima of transmittance for different d. The inset in Fig. 6.4 shows the data at the transitional pattern (for $d < a^*$), plotted as $\ln(\omega_2)$ vs $\ln(1 - d/a^*)$, where $a^* = 464.5\text{nm} \approx a$ [14]. From the fit we find that

$$\omega_2 \sim (a^* - d)^{0.071} \quad . \tag{6.5}$$

This is not surprising, since the evolution of the structures in the series indeed resembles that of the evolution of heterogeneous phases (e.g. conducting and dielectric) in the percolation problem, where critical phenomena are expected at the percolation threshold [Bergman & Imry, 1977].

To demonstrate this further, we calculate the low frequency limit of Eq. 6.2

$$\varepsilon(\omega \to 0) = \varepsilon_{eff} + i\frac{4\pi\sigma_{eff}}{\omega} \quad , \tag{6.6}$$

where the effective dielectric constant is

$$\varepsilon_{eff} = \varepsilon_b + \frac{\omega_{p2}^2}{\omega_2^2} \sim \omega_2^{-2} \quad . \tag{6.7}$$

It has been shown in Ref. [Bergman & Imry, 1977] that $\varepsilon_{eff} \sim | p - p_c |^{\gamma(\beta-1)}$, where p is the conducting phase fraction, and $p_c < p$ is the conducting phase fraction at the

percolation threshold. Combining this with Eq. 6.7, and noticing that $p_c \sim a^*$ and $p \sim d$, yields

$$\omega_2 \sim | a^* - d |^{-\gamma(\beta-1)/2}, \qquad (6.8)$$

which is in agreement with Eq. 6.5, provided that $-\gamma(\beta-1)/2 = 0.071$. Furthermore, the theory of Bergman & Imry [1977] shows that $\sigma_{eff} \sim | p_c - p |^{\gamma\beta}$, and therefore because of Eq. 6.3 $\gamma\beta = 1$, which leads to $\beta = 0.88$, and $\gamma = 1.14$. These values are in the range of the critical exponents observed in the systems with random percolation. For example, parameters obtained from the recent experiments with the Ti_3SiC_2 / Al_2O_3 hybrids are $\beta = 0.919$, and $\gamma = 1$ [Wu et al, 2007]. Thus, we show that the evolution of structures not only resembles, but in fact is a topological analog of the percolation problem, with the transitional pattern representing the percolation threshold. Similar effects have been studied in the Babinet series by Kempa [2010].

The hypersensitivity of response at the transitional pattern can lead to other exotic optical effects, as was already envisioned in ref [Bergman & Imry, 1977], as well as it can be exploited in applications. A slight modification of d at the percolation threshold (transitional pattern), for example by compression, temperature variation, defect formation due to adsorbed biological molecules, etc., will drastically change the transparency of the structure at the frequency corresponding to the transmission minimum. Thus, various sensors and switches can be based on this effect.

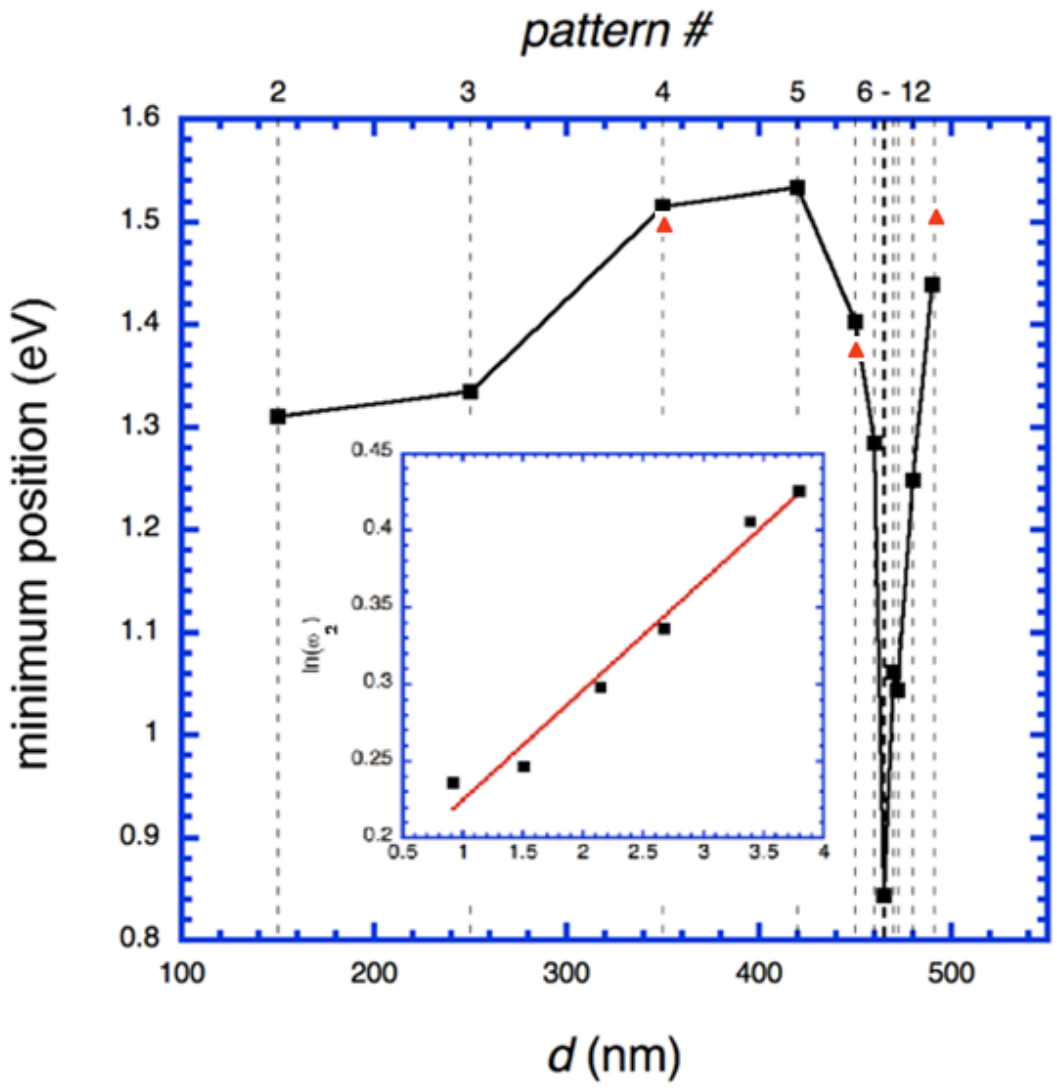

Fig. 6.4 (Color online) Simulated positions (black squares connected by solid lines) of the Transmittance minima positions vs. the diameter of the holes *d*. Red triangles are the experimental results of Transmittance minima positions. Inset: $\ln(\omega_2)$ vs. $\ln(1-d/a^*)$ below the threshold (for $d < a^*$). The extracted slope is 0.071.

6.4 Conclusion

In conclusion, using model calculations and simulations, together with experimental results, we show that an electromagnetic response of a series of thin film periodic nanostructures, which evolve from small diameter holes into island arrays, follows the geometric evolution. Two topologically distinct spectral types have been identified; one for holes and one for islands. We demonstrate that the critical behavior of the effective dielectric function agrees with that predicted by the percolation theory, and thus conclude that the hole-to-island structural evolution in this series is a topological analog of the percolation problem, with the percolation threshold at the transitional pattern. These percolation transitions based on structural changes can help in designing light switches, light filters and other optical devices.

Chapter 7

Multicore nanocoax and its solar cell application

In the previous chapter, we have shown that electromagnetic waves can propagate in the dielectric cladding of a coax cable as a TEM mode, which is low loss and broadband (i.e. no cut-off frequency). Light can also propagate along a multicore coax configuration (details described below), and in this chapter, we will show how this can be used in a new generation of solar cell. Some of the work is published [Naughton et al., 2010; Paudel et al., 2010]

7.1 Introduction

As shown in Chapter 4, light can propagate, via a TEM-like mode, multi-wavelength distances along a thin nanocoaxial cable with radial dimensions much shorter than the wavelength. Such a TEM mode can also propagate in a so-called multicore coax configuration, in which more than one coaxial core is present [Pozar, 2005].

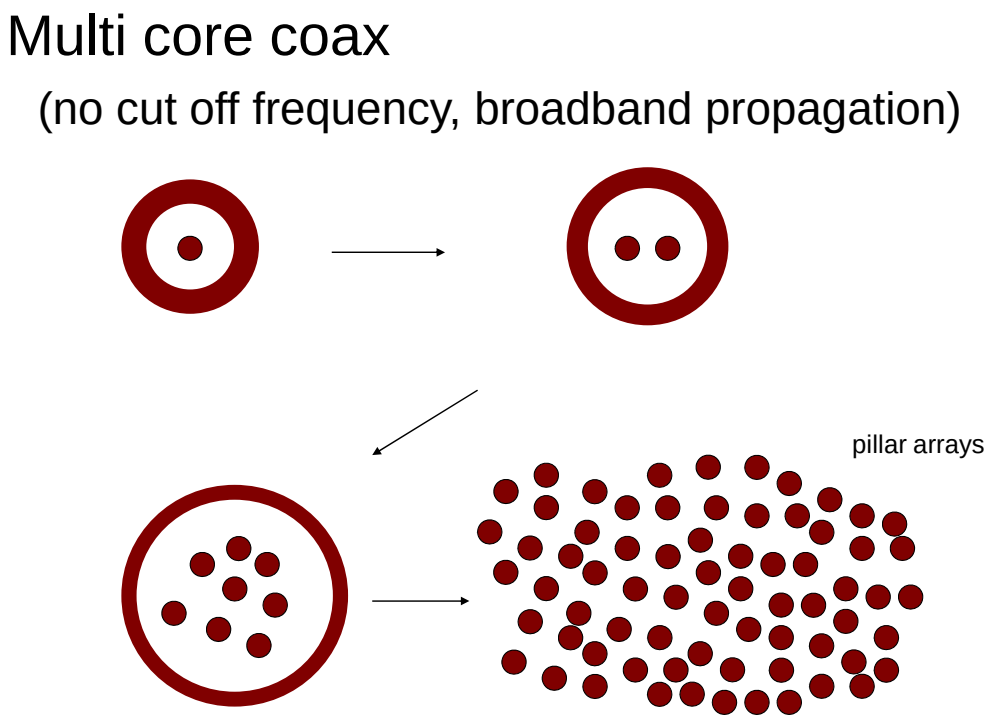

Fig. 7.1 Illustration of the transition from one nanocoaxial cable to the multicore coax configuration.

As the number of pillars in an array goes to infinity, i.e. the area of the cross section becomes very big (> wavelength), a conventional outer coax electrode is not fornally needed. Fig. 7.1 illustrates the transition of this configuration design. With the long pillars standing closely parallel to each other, even without an outer electrode, the structure can still allow a TEM mode to propagate long distance into the pillars.

7.2 Light Propagation

The main reason for us to study the multi-core coax configuration is the fact that it is proposed as a basis for novel solar cells. A photovoltaic absorber material was proposed to be deposited on the surface of the pillars, and the multi-core coax would expose this absorber to light along the pillars. The remaining part of this Chapter presents the improvement processes attempting to maximize this absorption.

We use MEEP to confirm light propagation and observe the detailed field distribution in and around a structure, to optimize light penetration in the array geometry such as pillar length, spacing, etc. The parameters are defined as described earlier, and various dimension parameters have been simulated. Some initial parameters were used as a start, and Fig. 7.2 is an example.

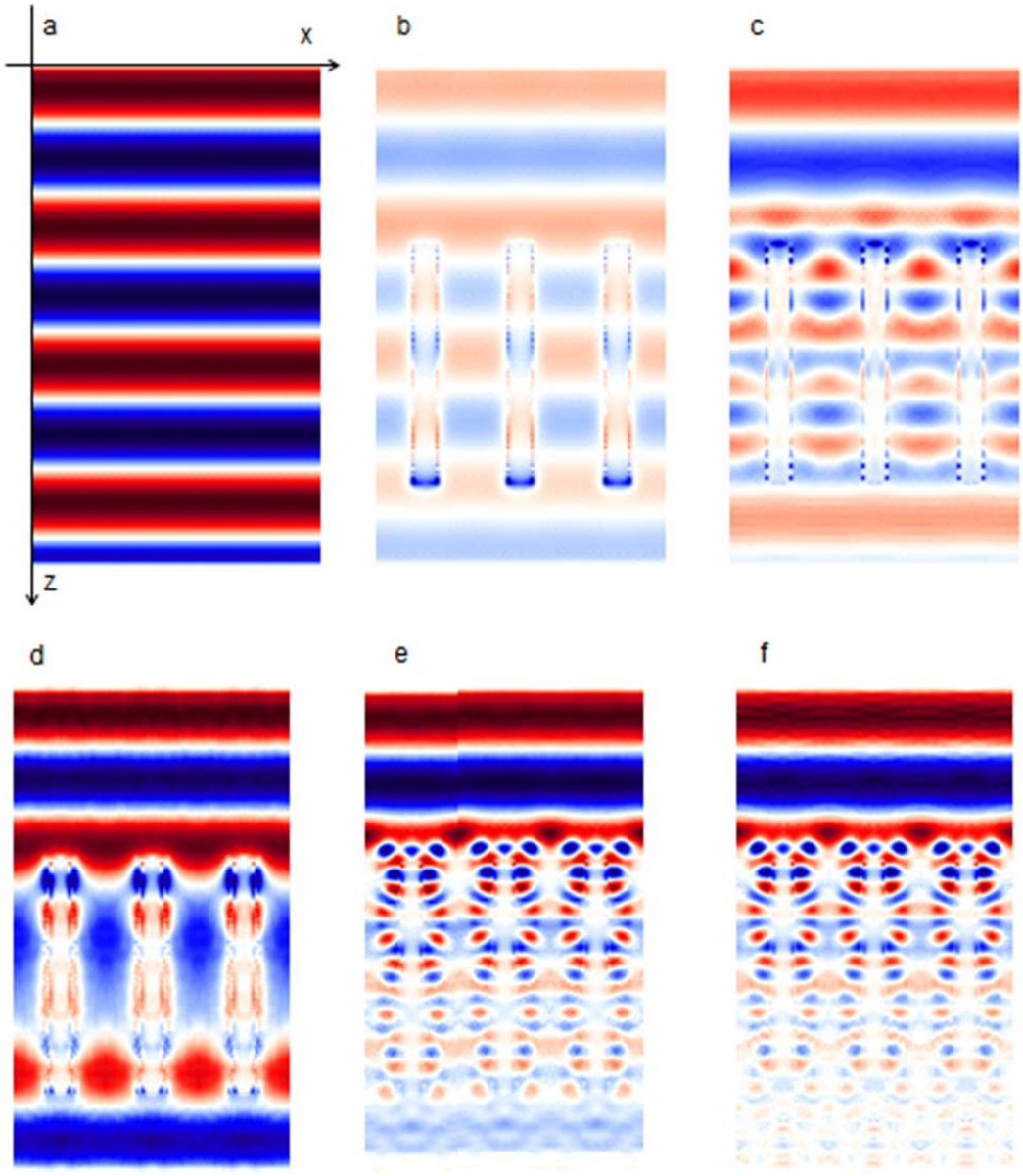

Fig. 7.2 Electric field x-component (Ex) in and around a simple square array of Ag nanopillars (shown are three unit cells of the array). The color intensity is proportional to the field amplitude, and color represents the sign (field direction).

Fig. 7.2 shows a series of simulations of the electric field in a single unit cell of a simple square array of Ag nanopillars, in various circumstances of medium, coating and substrate. The different field maps give us a basic sense of where the light goes and how the energy (field) is distributed inside the nanostructures. The incident light source is a plane wave excited from a plane located on the top of the structure. The incident light is of 500 nm wavelength and Ex-polarized. The light propagates along the z-direction down through the nanopillars, and the field map shows the detected Ex field in the given plane cut though the center of the pillars. (a) shows the field distribution in air. (b) has nanopillars in a square array made with Ag, each of 1 μm length and 100 nm diameter. In (c), the Ag pillars are embedded in ITO. In (d), the Ag pillars are coated with 20 nm Si on their surfaces. Then (e) shows that the nanopillars are coated with 20 nm Si first and then imbedded in ITO; and finally in (f), another layer of Si substrate is added to the bottom of the structure in (e). The color code and intensities are consistent and relative within each individual nanostructure.

In Fig. 7.2 (a), one sees how a plane wave propagates in the vacuum. In Fig 7.2 (b), despite the formation of some SPs on the surface of the Ag pillars, the light propagates through the nanopillar array without field distortions or much decrease in intensity. Light essentially just goes right through these nanopillars. This information tells us that even though this nanostructure may not be ideal for high absorbance, it can serve as a good transmission line. Then in Fig. 7.2 (c), when the nanopillar array is embedded in ITO, there are SPs formed and some Ex field distortion but only inside the array. There is also

some reduction in the transmitted light. In Fig. 7.2 (d), when the nanopillars are each coated with 20 nm Si on the surface, but not embedded in ITO, the Ex field is shown with different SPs forming in the Si coating, and significantly damped along the pillars in the Si coating. While some of the field still manages to propagate through the nanopillar array. Then in Fig. 7.2 (e), the nanopillars are each coated with 20 nm Si on the surface first and then embedded in ITO. We can see that still different SPs are forming, and the distortion of the Ex field is pronounced and the Ex field pattern is quite complicated. Some, yet less than in (d), light propagates through the array. Lastly, Fig. 7.2 (f) shows the field map for the same structure as in Fig. 7.2 (e) except it has a Si substrate at the bottom of the nanopillars. The field maps are similar for the last two, but in Fig. 7.2 (f), the distortion of the Ex field seems to continue outside the array, and very little light propagates though the array because of the Si substrate at the bottom. We can conclude that the structure in Fig 7.2 (f) has high absorbance and may be a good candidate for the solar cell design.

After we get basic information about how the field is distributed in the nanopillar array, we started to investigate more complicated structures: the ones that can be experimentally made and are inspected to be used in the experimental nanostructure design. Fig. 7.3 shows the Ex field around amorphous silicon (a-Si) coated Ag nanopillars in a honeycomb array. Various directional cuts through the unit cell are used to illustrate the field variation.

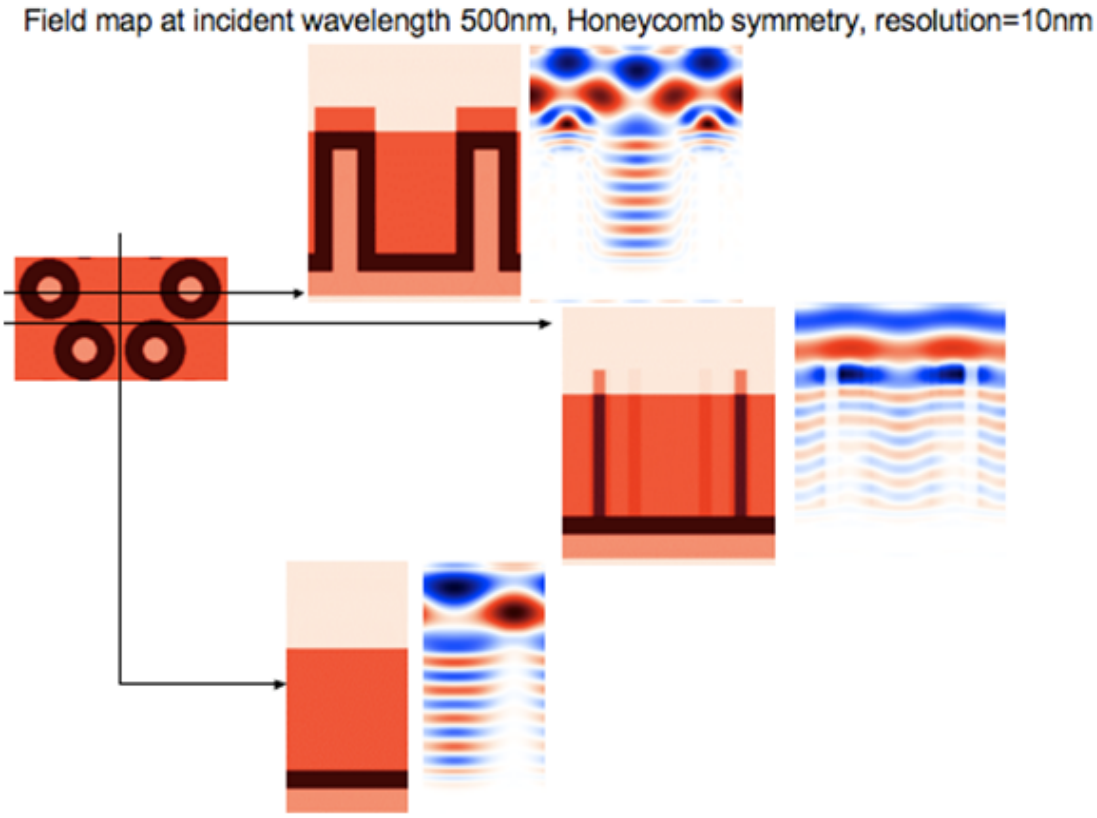

Fig. 7.3 Radial component of the electric field around a-Si-coated Ag nanopillars in a honeycomb array; shown is only one unit cell of the array. The color intensity is proportional to the field amplitude, and color represents the sign (field direction).

As one can see in the field map, this simulation shows that the honeycomb geometry has a large back reflection of light from the flat bottom sections of the structure; this causes an undesired, relatively large reflectance from the structure. Similar simulation for an HCP structure (also denoted as triangle symmetry in the figures) is shown in Fig. 7.4 and shows a much more efficient light distribution and attenuation in the absorber.

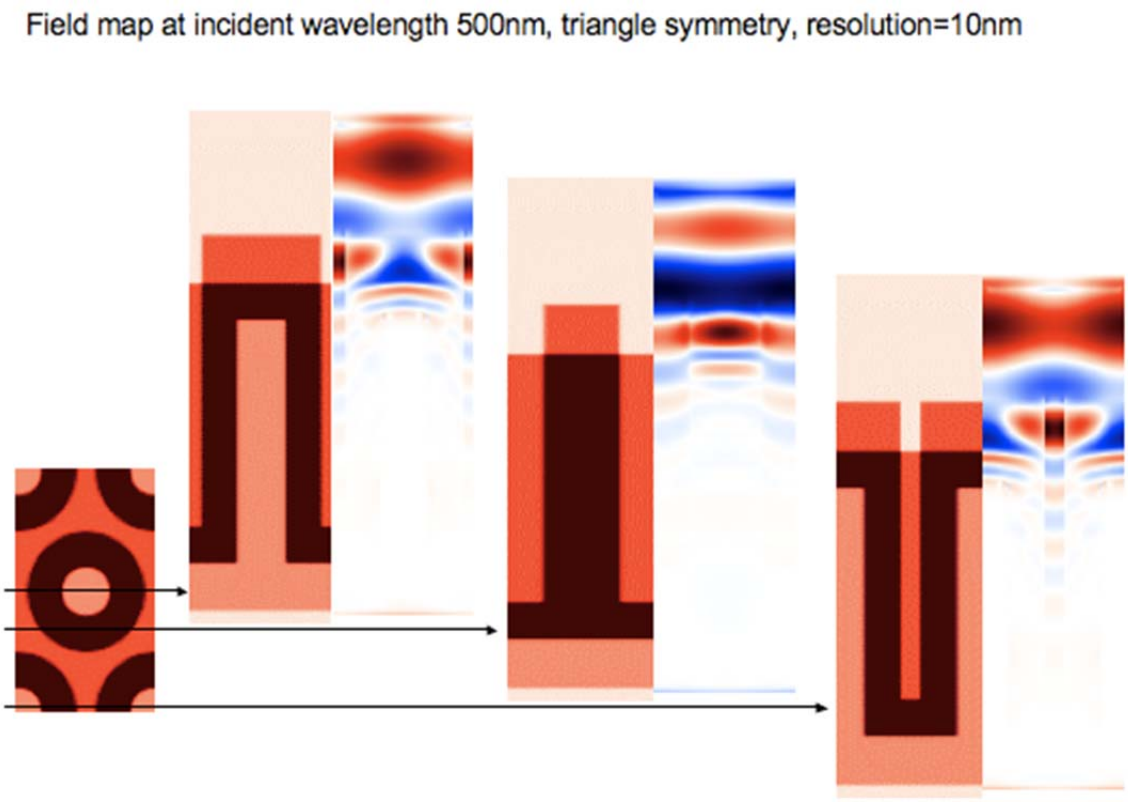

Fig. 7.4 Radial component of the electric field around aSi-coated nanopillars in an HCP array; shown is only one unit cell of the array. The color intensity is proportional to the field amplitude, and color represents the sign (field direction).

In addition to the vertical field analysis, we have also performed the horizontal field mapping. Fig. 7.5 shows an example of electric field maps at three vertical heights relative to pillar tips: 500 nm above, at, and 500 nm below, for a honeycomb array. The incident light has wavelength of 500 nm.

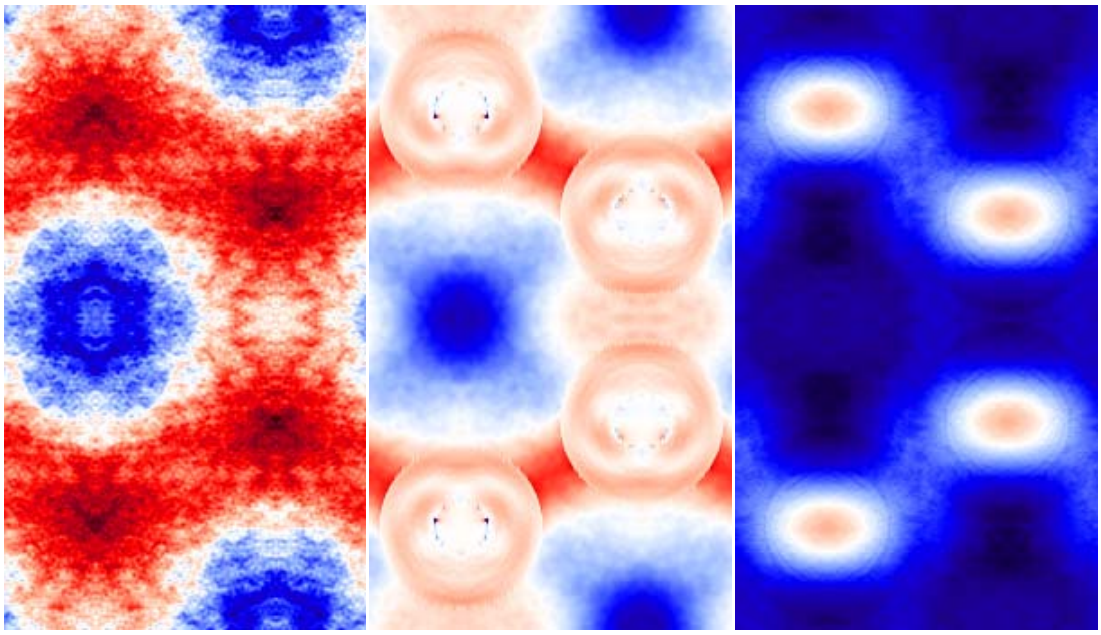

Fig. 7.5 Horizontal maps of the electric field at three heights relative to nanopillar tips: 500 nm above (left), at the tips (middle), and 500 nm below the tips. The color intensity is proportional to the field amplitude, and color represents the sign (field direction).

From reading the field maps, we have been able to achieve basic information about how good each structure is at absorbing the electromagnetic waves. A series of simulations were then performed to select the best array structure, thicknesses of all relevant layers of metals, transparent conducting oxide (TCO) and the absorber. Additionally, anti-reflection schemes, phase and space randomization, pillar shape modifications, etc. were also studied. We have determined that the optimal structure is the HCP array of Ag nanopillars. In the array, each pillar should be ~2 μm long, and have diameter of at most 200 nm. In the normal configuration, pillar length of 1 μm is sufficient, but efficient pillar arrangements are needed (e.g. HCP is better than honeycomb). Fig. 7.5 shows,

that the nanopillar array structure traps light well, in spite of the thin absorber. This shows the potential of the nanopillar array architecture, which can be used as an ultimate light trapping scheme.

Other metals or metallic materials can also be used in place of Ag at the core of the coaxial cable. Multi-walled carbon nanotubes have been used in simulations, and the results are published [Paudel, 2011] and also shown below in Fig. 7.6. A plane wave of 500 nm wavelength propagates from vacuum toward the array (from the top), with the electric field polarized in the horizontal direction. The area structure is honeycomb, the nanopillars length is set at 1500 nm, and the closest inter-pillar distance is 870 nm. Color maps show the in-plane component of the electric field in the vicinity of neighboring coaxial wires, with top and side views. Propagation of the waves, transverse electromagnetic (TEM)-like mode (as discussed in Chapter 4), along the coax is clearly visible. Simulations for other frequencies show similar patterns. The action of the a-Si absorber is clearly visible, with electric field strongly damped toward the base of the coaxes inside the absorber and in between the closely spaced coaxes; this demonstrates the efficiency of the absorption along the long optical direction. However, it is also clear that a large fraction of the light energy propagates in the voids of the honeycomb structure (left and right sides of lower image), and escapes absorption.

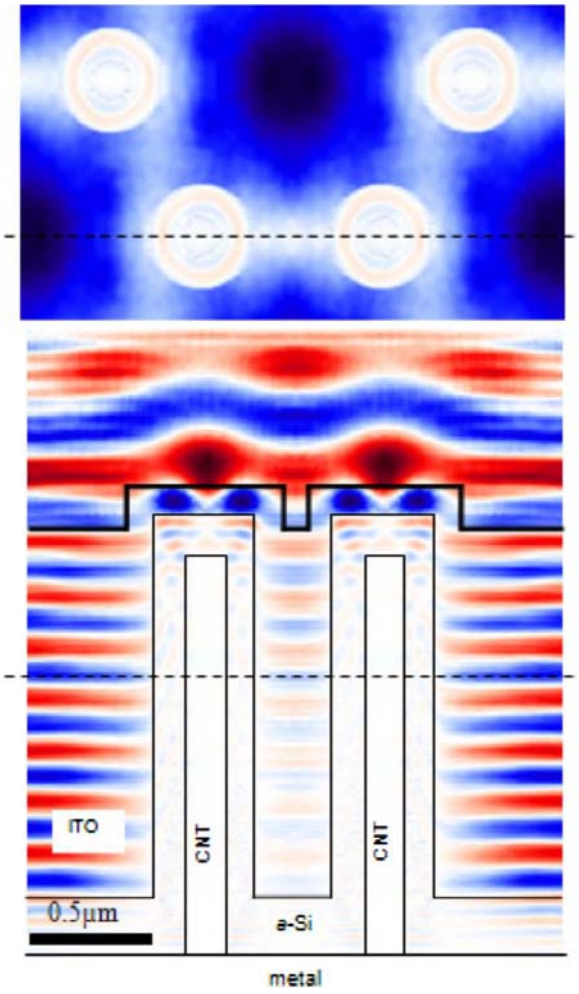

Fig. 7.6 simulation of light penetration into nanopillar array, with top and side views. The dotted lines are the places to cut to get the views of the other plot. Plotted is the horizontal component of the electric field strength with vacuum wavelength of λ=500 nm. The color intensity is proportional to the field amplitude, and color represents the sign (field direction). The nanopillar length is 1.5 mm, and the closest inter-pillar distance is 0.87 mm.

7.3 Total absorbance of model solar cells

Absorbance is an important parameter of a nanodevice. The top panel of Fig. 7.7 compares the experimental results of the total absorbance of three nanostructural a-Si absorber samples [Courtesy of Solasta, Inc.]. The black thin line is the planar sample, with 300 nm thick a-Si grown on a Ag coated Si wafer. The blue thick line is 300 nm thick a-Si grown on a Ag coated textured-ZnO substrate. The red line is the hexagonal closed packed (HCP) Si nanopillar array. The array was subsequently coated with an 50 nm conformal film of metal (Ti+Au+Ag) and a-Si (~200nm on pillar tops and in between pillars; ~150 nm on the pillar walls). SEM image of a typical HCP array with L = 900nm is shown in the bottom panel of Fig. 7.7.

By calculating the flux, we conduct the flux analysis to simulate the nanopillar array absorbance. We have designed nanopillar arrays with lattice constant (center of a pillar to center of the adjacent one), denoted as L, ranging from 900 to 1500 nm. We have started with making gradual adjustments to the film thickness and the computational model of the dielectric functions of a-Si so that the simulated result for the planar structure is within 5% of the measured values (black line in Fig. 7.7) at each frequency. The details can be referred to the parameter section in Chapter 2.

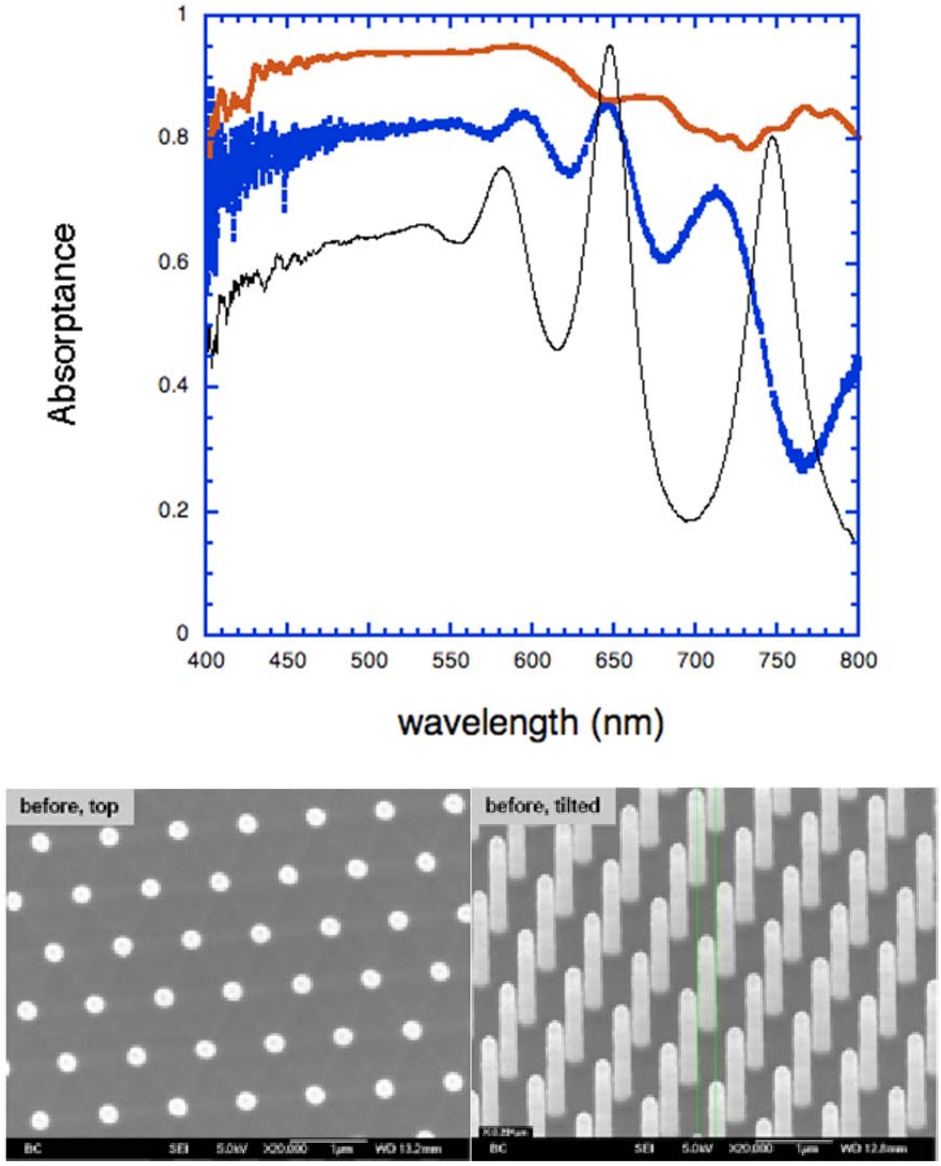

Fig. 7.7 Top: Experimental total absorbance of planar (black line), textured planar (blue line) and nanopillar (red line) samples. Bottom: SEM image of an HCP array of a Si nanopillar array.

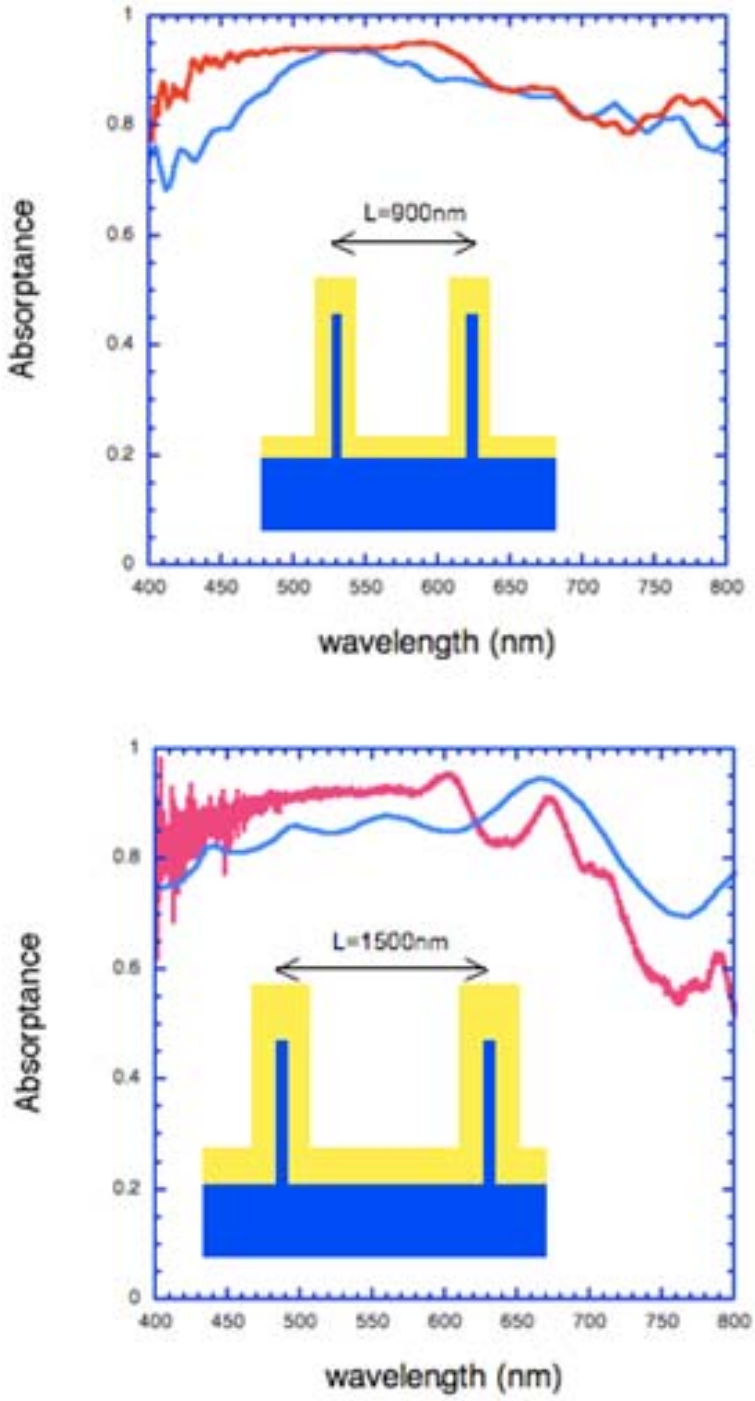

Fig. 7.8 Measured (red) and simulated (blue) total absorbances of the nanopillar arrays with L = 900 nm (top) and L= 1500 nm (bottom).

The total absorbance is the absorbance of the light into the total structures, accounting for light energy loss into a-Si and Ag. Measured and simulated total absorbance of nanopillar arrays with L = 900 nm and L = 1500 nm are plotted in Fig. 7.8. Note, that while the thickness of the a-Si (i) film for the array with L = 900 nm is about 200 nm (on pillar tops, and in between nanopillars), and about 150 nm on the pillar walls; It is much thicker for the L = 1500 nm array: ~ 300 nm (on pillar tops, and in between nanopillars), ~ 200 nm on the pillar walls. The agreement between the first principle simulations and experiment is very good. The simulated integrated absorbance is well within 10% of the measured one, in the frequency range of interest.

7.4 More examples

A nanopillar array is a transmission line for light, and if properly designed, light will propagate vertically until absorbed by the absorber (or maybe on the way of returning after reflecting from the bottom). In order to improve the total absorbance, we have tried different ways. In addition to trying different parameters to find an optimal geometric structure, we also simulate the application of an anti-reflection coating (ARC) on top of the whole structure. Indeed, this concept works very well, as shown in Fig. 7.9. It shows the simulated structure of the L= 900 nm pillar array and the computed absorbance, without and with the anti-reflection coating. We choose ITO to be the ARC material to

put on the outer-layer of Si. We calculate the total absorbance for the nanostructure with ARC coating, and we try the ARC coating with different thickness, layering places (on Ag or Si) and with a thin Au layer. We found significant improvement of the absorbance with the ARC (ITO) coating of 70 nm on top of the Si of the whole structure.

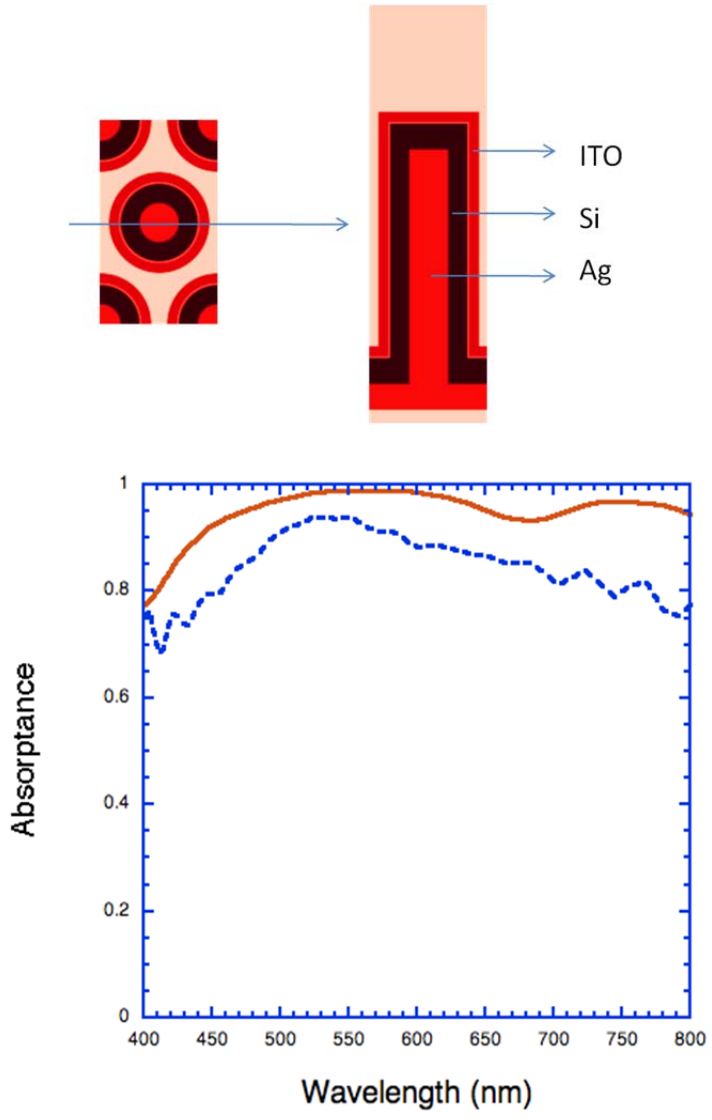

Fig. 7.9 Simulated total absorbance of the nanopillar array (top) with L = 900 nm: with ARC (red), and without ARC (blue).

There are technological difficulties with the conformal deposition of films on high aspect structures, in particular with vertical surfaces. One of the potential problems is cavity formation, when a top TCO film is deposited on long nanopillar structures. Fig. 7.10 shows the FIB image of such cavities forming in between the nanopillars.

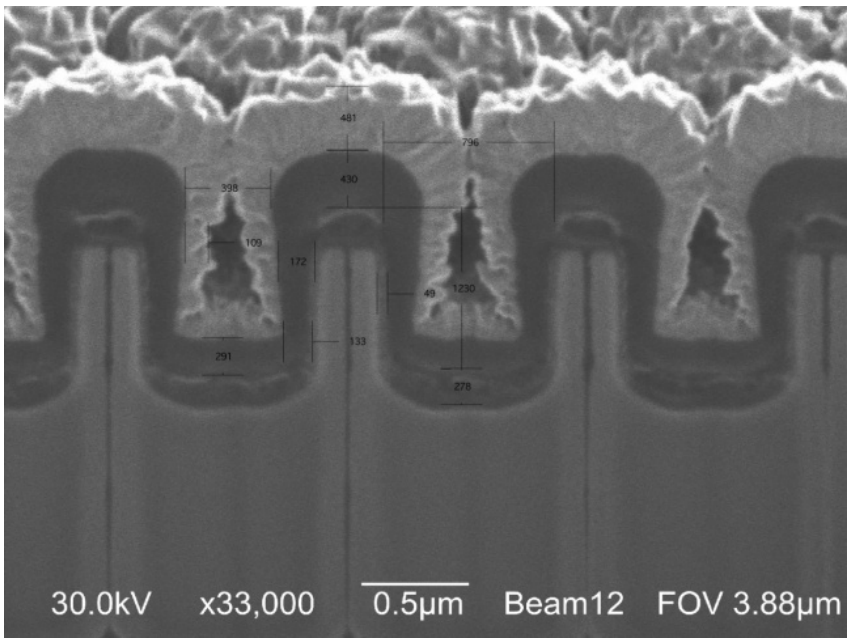

Fig. 7.10 FIB image of the nanopillar array showing formation of micro-cavities in between the nanopillars after deposition of the top TCO (ZnO) layer. (Courtesy of Solasta, Inc., and G. McMahon, Boston College)

We simulate the electric field distribution in such a cavity area as shown in Fig. 7.11. Micro cavities do not prevent light from entering the $_a$-Si film, and thus they are only an

electrical contact problem, not optical. This is further confirmed by flux simulations (not shown), which show only minor modifications on the absorbance spectrum.

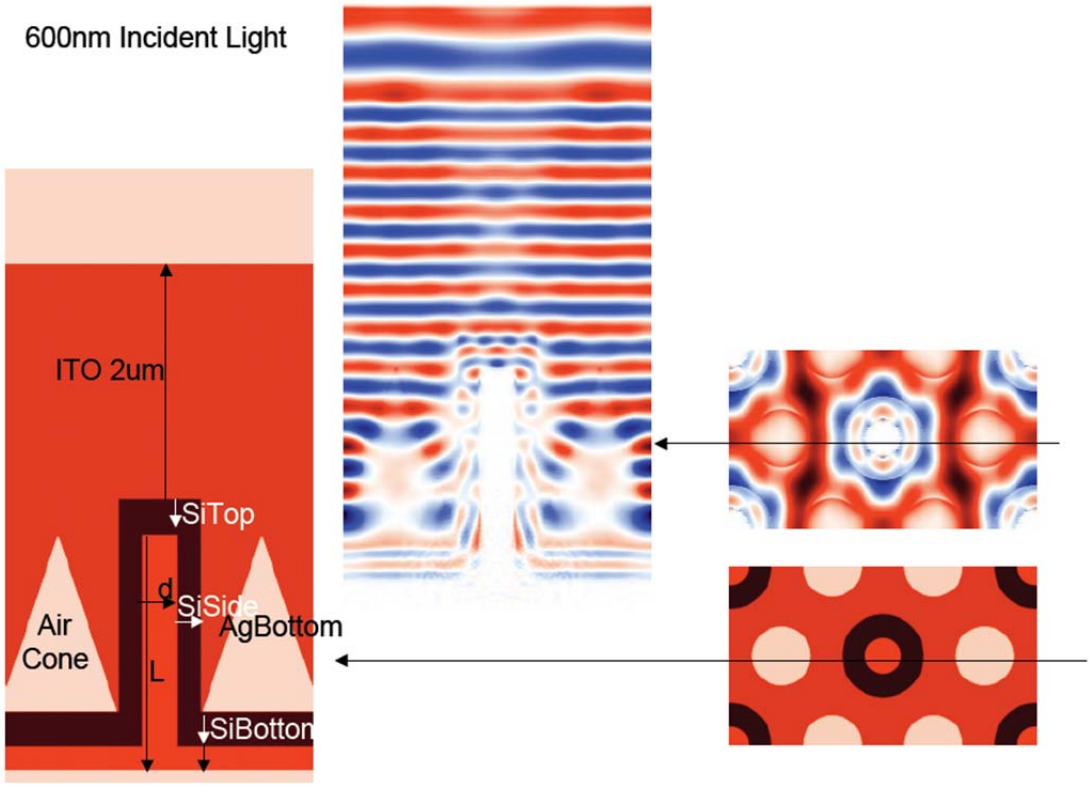

Fig. 7.11 Simulation of the electric field in the micro-cavities. The color intensity is proportional to the field amplitude, and color represents the sign (field direction).

We have also investigated the possibility of changing the pillar shape into a conical one, which is much easier to deposit films on. Fig. 7.12 shows that such a shape not only does not prevent the coax action, but in fact somewhat enhances it. Both of these simulations should have provided guideline for the future design of solar cells.

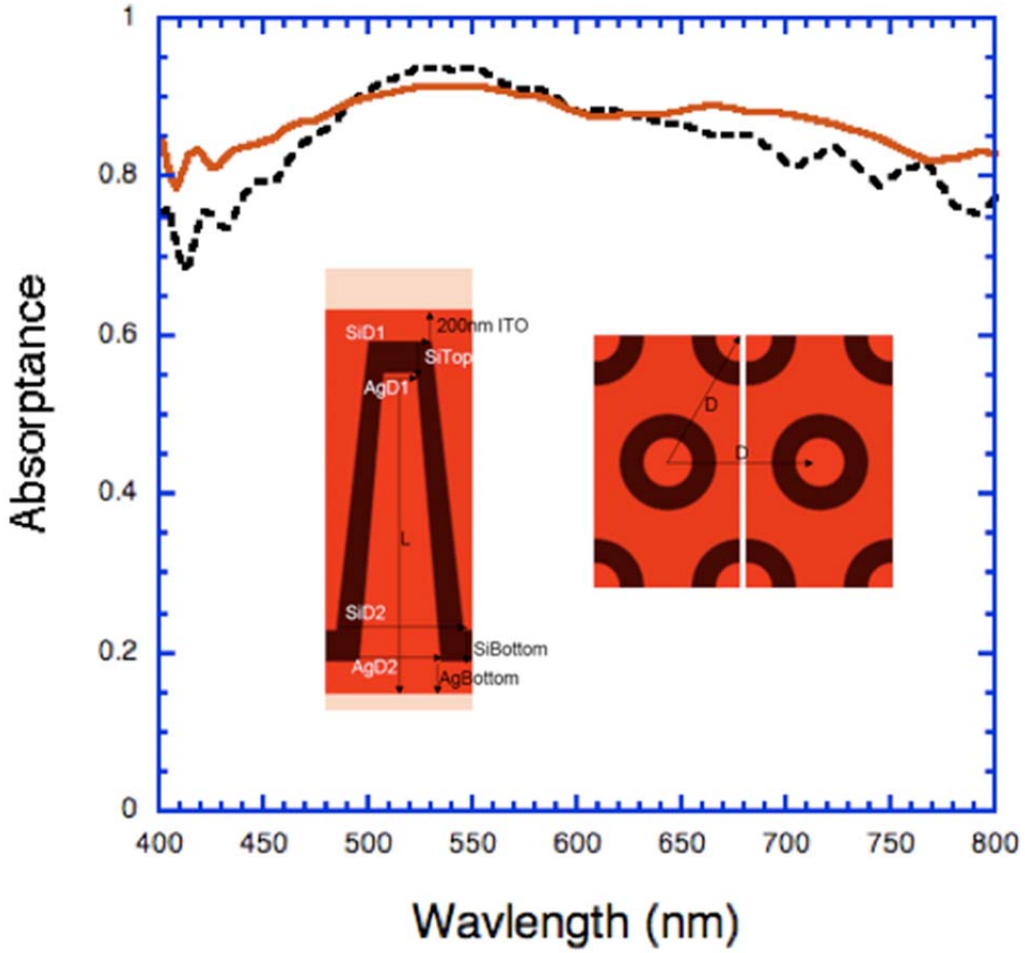

Fig. 7.12 Simulation of absorbance (red line) in the conical pillar array, with pitch of 900 nm. Pillar height 2 μm, a-Si thickness on the top and bottom (200 nm), on the wall (100 nm on top, 150 nm on the bottom). Black line is for the corresponding cylindrical pillar array. The color intensity is proportional to the field amplitude, and color represents the sign (field direction).

7.5 Conclusions

We have simulated the optical characteristics, mainly the absorbance, of many nanostructures starting from nanopillars. We started with known experimental structures and results, and employed accurate parameters and dielectric functions are used in the simulations. We were able to find an optimal structure to give similar results as the measured ones, as shown in Fig 7.8. Then after numerous trials, we proposed a nanostructure (as shown in Fig. 7.9) with certain ARC coating, to be used in the next version of solar cell design. We believe this new scheme is going to help improve the total efficiency of the solar cells. We also simulated a major structural imperfection caused by technology constraints, and proved that it does not affect the ability to absorb the light. Another possible structure, which is easier to make experimentally, is simulated and proven to give a more even and high absorbance.

Chapter 8

Summary and Final remarks

This dissertation studied a few new and interesting projects in the area of plasmonics, a field to study the optical effects of nanostructures based on surface plasmons.

We studied the wire transmission line, and we obtained the plasmon dispersion relation of silver nanowire from the simulations, confirming that nanowires can be treated as Fabry-Perot resonators of SPs. Some preliminary research on the interaction/coupling between silver nanowire and other nanostructures were also done.

We investigated in detail a silver coaxial nanowaveguide and show that the waveguide supports a plasmon polariton mode, the “TEM-like” mode, at low frequency. This gapless mode show promises of being capable of transmitting sub-wavelength electromagnetic waves for long distances.

We simulated the optical characteristics of the multi-core coaxial cable, which can be used as a basis for novel solar cells. These studies determined configurations that maximize cell performance.

We investigated the optical response of arrays of quasi-triangular gold nanoparticles of different sizes, and show that the physics was due to a surface/edge plasmon resonance in these nanoparticles.

We also investigated the electromagnetic responses of a series of thin film periodic nanostructures, which evolve from small diameter holes into island arrays, and showed that the critical behavior of the effective dielectric function agreed with that predicted by percolation theory.

All the work in this dissertation provides important information of the plasmonics in nanostructures, and guides future research on numerous potential applications in the nano-optics.

Bibliography

Agrawal, G.P., “Optical Waveguides (OPT568)”, Institute of Optics, University of Rochester (2007).

Akimov, A. V., Mukherjee1, A. Yu, C. L., Chang1, D. E., Zibrov1, A. S., Hemmer.P. R., Park, H., and Lukin, M. D., “Generation of single optical plasmons in metallic nanowires coupled to quantum dots”, Vol 450, 402-406 (2007).

Al-Bader, S. J., and Jamid, H.A., “Diffraction of surface plasmon modes on abruptly terminated metallic nanowires”, Phys. Rev. B 76, 235410 (2007).

Ancey, S., Décanini, Y., Folacci, A., and Gabrielli1, P., “Surface polaritons on metallic and semiconducting cylinders: A complex angular momentum analysis”, Phys. Rev. B 70, 245406 (2004).

Anderson, U., “Time-Domain Methods for the Maxwell Equations”, Ph. D. Thesis, Royal Institute of Technology (2001).

Ashcroft, N. W., and Mermin, N. D., “Solid State Physics”. Philadelphia: Saunders (1976)

Assefa, S., Xia, F., and Vlasov, Y. A., “Reinventing germanium avalanche photodetector for nanophotonic on-chip optical interconnects”, Nature 464, 80 (2010).

Bakshi, P., Broido, D. A., and Kempa, K., “Electromagnetic response of quantum dots”, Phys. Rev. B 42, 7416 (1990).

Baida, F. I., Belkhir, A., Van Labeke, D., and Lamrous, O., “Subwavelength metallic coaxial waveguides in the optical range: Role of the plasmonic modes,” Phys. Rev. B 74, 205419 (2006).

Barnes, W. L., Dereux, A., and Ebbesen, T. W., “Surface plasmon subwavelength optics,” Nature 424, 824- 830 (2003).

Berenger, J. “A perfectly Matched Layer for the Absorption of Electromagnetic Waves” J. Comput. Phys. 114, 185 (1994)

Bergman, D. J., and Imry, Y., “Critical Behavior of the Complex Dielectric Constant near the Percolation Threshold of a Heterogeneous Material”, Phys. Rev. Letters 39, 1222 (1977).

Birnbaum, K. M., Boca, A., Miller, R., Boozer, A. D., Northup T. E., and Kimble H. J., “Photon blockade in an optical cavity with one trapped atom”. Nature 436, 87–90 (2005).

Booker, H.G., "Slot aerials and their relation to complementary wire aerials (Babinet's principle), " Proc. IEE(London) Vol. 93, Pt. 3A, pp. 620-626 (1946).
Bohm D. and Pines, D. “A Collective Description of Electron Interactions: III. Coulomb Interactions in a Degenerate Electron Gas”, Phys. Rev. 92, 609 (1953).

Bohren, C. F., and Huffman, D. R., “Absorption and Scattering of Light by Small Particles”, Wiley, New York, 1983.

Boyd, G. T., Yu, Z. H., and Shen, Y. R.. “Photoinduced luminescence from the noble metals and its enhancement on roughened surfaces”, Phys. Re**v**. B, 33, 7923 (1986).

Bozhevolnyi, S. I., and Lozovski. V. Z., “Second-harmonic scanning optical microscopy of individual nanostructures”, Physical Review B, 65, 23 (2002).

Bozhevolnyi, S. I., Volkov, V. S., Devaux, E., Laluet, J.-Y., and Ebbesen, T. W., “Channel Plasmon subwavelength waveguide components including interferometers and ring resonators,” Nature 440, 508-511 (2006).

Bréchignac, C., Connerade, J. P., “Giant resonances in free atoms and in clusters”, J. Phys. B 27, 3795 (1994).

Brey, L., Johnson, N. F., and Halperin, B. I., “Optical and magneto-optical absorption in parabolic quantum wells”, Phys. Rev. B 40, 10647 (1989).

Broadbent, S., Hammersley, J., "Percolation processes I. Crystals and mazes", Proceedings of the Cambridge Philosophical Society 53: 629–641, (1957).

Brongersma, M. L., and Kik, P. G., “Surface Plasmon Nanophotonics”, Springer, (2007).

Carlos, U., “Analytical solutions to Maxwell's equations in homogeneous media”, Master of Science thesis, San Jose State University, (2005).

Caviglia, G., and Morro, A., “Wave propagation in multilayered anisotropic solids”, International Journal of Engineering Science, 38, 8, 847-863 (2000).

Chang, D. E., Sorensen, A. S., Demler, E. A. & Lukin, M. D. “A single-photon transistor using nanoscale surface plasmons”, Nature Physics 3, 807-812 (2007).

Chen, H.T., O'Hara, J. F., Taylor, A. J., Averitt, R. D., Highstrete, C., Lee, M., Padilla, W. J., “Complementary planar terahertz metamaterials", *Opt. Exp.* 15, 1084 (2007).

Chen, H., Wang, J., Yu, H., Yang, H., Xie, S., Li, J., “Transmission Electron Microscopy Study of Pseudoperiodically Twinned Zn_2SnO_4 Nanowires”, J. Phys. Chem. B 109, 2573 (2005).

Choi, D. H. and Hoefer, W. J., "The finite-difference time-domain method and its application to eigenvalue problems". IEEE Transactions on Microwave Theory and Techniques 34, 1464–1470 (1986).

Ctistis, G., Patoka, P., Wang, X., Kempa, K., and Giersig, M., “Optical Transmission through Hexagonal Arrays of Subwavelength Holes in Thin Metal Films”, NanoLetters 7, 2926 (2007).

Cunningham, S. L., Maradudin, A. A., and Wallis, R. F., “Effect of a charge layer on the surface-plasmon-polariton dispersion curve”, Phys. Rev. B 10, 3342 (1974).

Dickson, R. M.; Lyon, L. A., “Unidirectional Plasmon Propagation in Metallic Nanowires”, J. Phys. Chem. B, 104, 6095-6098 (2000).

Dionne, J. A., Lezec, H. J., and Atwater, H. A., “Highly confined photon transport in subwavelength metallic slot waveguides” *NanoLetters* 6, 1928 (2006).

Ditlbacher, H., Hohenau, A., Wagner, D., Kreibig, U., Rogers, M., Hofer, F., Aussenegg, F. R., and Krenn, J. R., “Silver Nanowires as Surface Plasmon Resonators”, Phys. Rev. Lett. 95, 257403 (2005).

Ditlbacher, H., Krenn, J. R., Schider, G., Leitner, A., and Aussenegg, F. R., “Two-dimensional optics with surface plasmon polaritons,” Appl. Phys. Lett. 81, 1762-1764 (2002).

Drossel, B., and Schwabl, F., “Self-organized critical forest-fire model”, Phys. Rev. Lett. 69, 1629 (1992).

Drude, P., “Zur Elektronentheorie der Metalle”, Annalen der Physik, vol. 306, 3, 566 (1900).

Drude, P., “Zur Elektronentheorie der Metalle; II. Teil. Galvanomagnetische und thermomagnetische Effecte”, Annalen der Physik, vol. 308, 11, 369 (1900).

Ebbesen, T. W., Lezec, H. J., Ghaemi, H. F., Thio, T., and Wolff, P. A., “Extraordinary optical transmission through sub-wavelength hole arrays,”, Nature 391, 667 (1998).

Englund, D.. Fattal, D., Waks, E., Solomon,G., Zhang, B., Nakaoka, T., Arakawa, Y., Yamamoto, Y., and Vuckovic, J., “Controlling the spontaneous emission rate of single quantum in a two-dimensional photonic crystal”, Phys. Rev. Lett. 95, 013904 (2005).

Etchegoin, P.G., Ru, E.C.L., Meyer, M., “An analytic model for the optical properties of gold”, J. Chem. Phys. 125, 164705 (2006).

Etchegoin, P.G., Ru, E.C.L., Meyer, M., “Erratum: “An analytic model for the optical properties of gold” [J. Chem. Phys. 125, 164705 (2006)]”, J. Chem. Phys. 127, 189901 (2007).

Fang, Y., Li, Zh., Huang, Y., Zhang, S., Nordlander, P., Halas, N. J., and Xu,H., “Branched Silver Nanowires as Controllable Plasmon Routers”, *Nano. Lett.* 10, 1950-1954 (2010).

Farjadpour, A., Roundy, D., Rodriguez, A., Ibanescu, M., Bermel, P., Joannopoulos, J. D., Johnson, S. D., and Burr, G., "Improving accuracy by subpixel smoothing in FDTD," Optics Letters 31 (20), 2972–2974 (2006).

Forstmann, F., and Gerhardts, R., “Metal Optics Near the Plasma Frequency”, Springer Tracts in Modern Physics, Vol. 109 (1986).

Fuchs, R., and Halevi, P., “Basic Concepts and Formalism of Spatial Dispersion”, in “Spatial Dispersion in Solids and Plasmas”, edited by Halevi, P., (1992) .

Garcia, N., and Bai, M., “Theory of transmission of light by sub-wavelength cylindrical holes in metallic films,” Opt. Express 14, 10028 (2006).

Garcia de Abajo, F.J., “*Colloquium*: Light scattering by particle and hole arrays”, Reviews of Modern Physics, Vol. 79, 1267 (2007)

Garcia-Vidal, F.J., Martin-Moreno, L., Ebbesen, T. W., and Kuipers, L., “Light passing through subwavelength apertures**”**, Reviews of Modern Physics, Vol. 82, No. 1 (2010)

Garnett. J. C. M, “Colours in metal glasses and in metallic films”, Philosophical Transactions of the Royal Society of London, series A, 203, 385 (1904).

Graff, A.; Wagner, D.; Ditlbacher, H.; Kreibig, “Silver Nanowires”, U. Eur. Phys. J. D 34, 263-269 (2005).

Grimmet, G., “Percolation”, Springer-Verlag (1999).

Hafner, Ch. “The Generalized Multipole Technique for Computational Electromagnetics”, Artech House, Boston, (1990).

Hafner, Ch., “Post-modern Electromagnetics Using Intelligent MaXwell Solvers,” John Wiley & Sons, (1999).

Hafner, Ch., Smajic, J., Agio, M., “Nanoclusters and Nanostructured Surfaces, Chapter 12. Numerical Methods for the Electrodynamic Analysis of Nanostructures, Nanoclusters and nanostructured surfaces,” American Scientific Publishers, CA, USA. (2010)

Hao, F., Nordlander, P., “Efficient dielectric function for FDTD simulation of the optical properties of silver and gold nanoparticles”, Chem. Phys. Lett. 446, 115 (2007).

Heavens, O. S., “The optical properties of thin solid films”, Dover Publications Inc., (1965).

Howard, S. T., “Waves in Plasma”, Springer, (1992).

Imamoglu, A. D., Awschalom, D., Burkard, G., DiVincenzo, D. P., Loss D., Sherwin, M., and Small, A., “Quantum information processing using quantum dot spins and cavity QED”, Phys. Rev. Lett. 83, 4204-4207 (1999).

Jackson, J. D., “Classical Electrodynamics”, 3rd ed. Wiley, (1999).

Jin, R., Cao, C. Y., Hao, E., Métraux, G., Schatz, G. C., Mirkin, C. A., “Controlling anisotropic nanoparticle growth through plasmon excitation”, Nature 425, 487 (2003)

Joannopoulos, J. D., Johnson, S. D., Winn, J. N., Meade, R. D., “Photonic Crystals, Modeling the Flow of Light”, Princeton University Express (2008).

Johnson, C. J., Dujardin, E., Davis, S. A., Murphy, C. J., Mann, S., “Growth and form of gold nanorods prepared by seed mediated, surfactant-directed synthesis”, J. Mater. Chem. 12, 1765,(2002)

Johnson P. B., and Christy, R. W., “Optical constants of the noble metals”, Phys. Rev. B 6, 4370 (1972).

Kandulski, W., “Shadow nanosphere lithography”, PhD-Thesis, Bonn University, (2007)

Karchevsky, A. L., “A frequency-domain analytical solution of Maxwell's equations for layered anisotropic media”, Russian Geology and Geophysics, Volume 48, Issue 8, Pages 689-695 (2007).

Karkashadze, D., Zaridze, R., Bijamov, A., Hafner, Ch., Smajic, J., Erni, D., “MAS and MMP Simulations of Photonic Crystal Devices”, Progress in Electromagnetics Research Symposium (PIERS), Pisa, March (2004).

Kelly, K. L., Coronado, E., Zhao, L. L., and Schatz, G. C., “The Optical Properties of Metal Nanoparticles: The Influence of Size, Shape, and Dielectric Environment”, J. Phys. Chem. B 107, 668 (2003)

Kelly, K. L., Lazarides, A. A., and Schatz, G. C., “Computational Electromagnetics of Metal Nanoparticles and Nanoparticle Aggregates”, Comput. Sci. Eng. 3, 67 (2001)

Kempa, K., “Dielectric function of media based on conductive particles”, Phys. Rev. B 74, 033411 (2006).

Kempa, K, “Percolation effects in the checkerboard Babinet series of metamaterial structures”, Phys, Status Solidi (RRL) 4, No. 8-9, 218-220 (2010).

Kempa, T., Carnahan, D., Olek, M., Correa, M., Giersig, M., Cross, M., Benham, G., Sennett, M., Ren Z. F., and Kempa, K., “Dielectric media based on isolated metallic nanostructures”, Journal of Applied Physics 98, 034310 (2005).

Kesten, H., “What is Percolation”, Notice of the AMS, 53, 5, 572, (2006).

King, P. R., Buldyrev, S. V., Dokholyan, N. V., Havlin, S., Lee, Y., Paul, G., Stanley, H. E., and Vandesteeg , N., “Predicting oil recovery using percolation theory”, Petroleum Geoscience, 7, S105 (2001).

Kirkland, A. I., Edwards, P. P., Jefferson, D. A., Duff, D. G., “Chapter 8. The structure, characterization, and evolution of colloidal metals”**,** Annu. Rep. Prog. Chem. Sect. C 87, 247 (1990).

Kiyan, R., Reinhardt, C., Passinger, S., Stepanov, A. L., Hohenau, A., Krenn, J. R., and Chichkov, B. N., “ Rapid prototyping of optical components for surface plasmn polaritons”, Optics Express, 15, 7, 4205, (2007).

Kohn, W., “Cyclotron Resonance and de Haas-van Alphen Oscillations of an Interacting Electron Gas”, Phys. Rev. 123, 1242 (1961).

Kolwas, K., “Plasmon resonances in a spherical sodium cluster and in a flat surface with a soft optical edge.” Appl. Phys. B 66, 467 (1998).

Kosiorek, A., Kandulski, W., Glaczynska, H., and Giersig, M., “Fabrication of nanoscale rings, dots, and rods by combining shadow nanosphere lithography and annealed polystyrene nanosphere masks”, Small, 1, 439–444 (2005).

Kreibig, U., Zacharias, P., “Surface plasma resonances in small spherical silver and gold particles”, Z. Physik 231, 128 (1970).

Kreibig, U., and Vollmer, M., “Optical Properties of Metal Clusters”, Springer-Verlag, Berlin, (1995).

Kunz, K. S., Luebbers, R. J., “The Finite Difference Time Domain Method for Electromagnetics”, Pennsylvania State University, University Park, USA, 1993

Kushwaha1, M. S., and Djafari-Rouhani, B.,“Green-function theory of confined plasmons in coaxialcylindrical geometries: Zero magnetic field,” Phys. Rev. B 67, 245320 (2003).

Kushwaha1, M. S., and Djafari-Rouhani, B., “Plasma excitations in multicoaxial cables,” Phys. Rev. B 71, 153316 (2005).

Krenn, J. R., Lamprecht, B., Ditlbacher, H., Schider, G., Salerno, M., Leitner, A., and Aussenegg, F. R., “Non diffraction limited light transport by gold nanowires”, Europhys. Lett. 60, 663 (2000).

Kretschmann, E., and Raether. H., “Radiative decay of non-radiative surface plasmons excited by light.” Zeitschrift fur Naturforschung, 23A, (1968).

Lacroche, T., and Girard, Ch., “ Near-fild optical properties of single plasmonic nanowires”, Appl. Phys. Lett. 89, 233119 (2006).

Lacroche, T., and Vial, A., “ Crystalline Structure’s influence on the near-field optical properties of single plasmonic nanowires”, Appl. Phys. Lett. 91, 123101 (2007).

Lamprecht, B., Krenn, J. R., Schider, G., Ditlbacher, H., Salerno, M., Felidj, N., Leitner, A., Aussenegg, F.R., and Weeber, J.C., “Surface plasmon propagation in microscale metal stripes”, Appl. Phys. Lett. 79, 51 (2001).

Langmuir, I., "Oscillations in ionized gases", Proc. Nat. Acad. Sci. U.S., 14, 628 (1928).

Lee, T.-W., Gray, S.K., “Subwavelength light bending by metal slit structures”, Opt. Express 13, 9652, (2005).

Lee, K. K., Lim, D. R., Luan, H.-C., Agarwal, A., Foresi, J., Kimerling, L. C., “Effect of size and roughness on light transmission in a Si/SiO2 waveguide: Experiments and model”, Appl. Phys. Lett., 77, 11, 1617 (2000).

Lezec, H.J., Degiron, A., Devaux, E., Linke, R. A., Martin- Moreno, L., Garcia-Vidal, F. J., and Ebbesen, T. W., “Beaming Light from a Subwavelength Aperture”, Science 297, 820 (2002).

Liu, M., Guyot-Sionnest, P., Lee, T. –W., Gray, S. K., “Optical properties of rodlike and bipyramidal gold nanoparticles from three-dimensional computations”, Phys. Rev. B 76, 235428 (2007).

Liu, S., Cheng, M.-T., Yang, Z.-J., and Wang, Q.-Q., “Surface plasmon propagation in a pair of metal nanowires coupled to a nanosized optical emitter”, Opt. Lett. 33, 8 (2008).

Lofton, C.; Sigmund, W. “ Mechanisms Controlling crystal Habits of Gold and Silver Colloids,” Adv. Funct. Mater. 15, 1197-1208 (2005).

Ma, Y., Li, X., Y, H., Tong, L., Gu, Y., and Gong, Q., “Direct measurement of propagation losses in silver nanowires”, Optical Letters 35, 8 (2010).

Maier, S. A., “Plasmonics: Fundamentals and Applications”, Springer, (2007).

Maier, S.A., Brongersma, M.L., Kik, P.G., and Atwater H.A., “Observation of near-field coupling in metal nanoparticle chains using far-field polarization spectroscopy”, Phys. Rev. B 65, 193408 (2002).

McKenzie, D.R., Savvides, N., McPhedran, R.C., Botten, L.C., and Netterfield, R.P., “Optical properties of a-Si and a-Si:H prepared by DC magnetron techniques”, J. Phys. C: Solid State Phys. 16, 4933 (1983).

Midwinter, J. E., “On the use of optical waveguide techniques for internal reflection spectroscopy”, IEEE J. Quantum Electron. QE-7, 339–344 (1971).

Mie, G., “Beiträge zur Optik trüber Medien, speziell kolloidaler Metallösungen,” Leipzig, Annalen der Physik 330, 377–445 (1908). Translated by Newman, P., “Contributions on the optics of turbid media, particularly colloidal metal solutions”, Technical Translation Service, Sandia Laboratories, Albuquerque, New Mexico, (1978).

Monro, T. M., Belardi, W., Furusawa, K., Baggett, J. C., Broderick, N. G. R., and Richardson, D. J., “Sensing with Microstructured optical Fibres”, Meas. Sci. Technol. 12, 854–858 (2001)

Muhlschlegel, P., Eisler, H. J., Martin, O. J. F., Hecht, B., and Pohl, D. W. Resonant Optical Antennas. Science 308, 1607-1609 (2005).

Nah, S., Li, L., Liu, R., Hao, J., Lee,S. B., and Fourkas, J. T., “Metal-Enhanced Multiphoton Absorption Polymerization with Gold Nanowires”, *J. Phys. Chem. C* 114, 7774-7779 (2010).

Nah, S., **Peng, Y.**, Ropp, Ch., Fourkas, J. T., Kempa, K., and Waks, E., "Photochemistry at a distance with guided, nonlinearly-generated emission in metal nanowires: A new paradigm for precision optical nanoassembly," submitted

Naughton, M. J., Kempa, K., Ren, Z. F., Argenti, N., Gao, Y., Rybczynski, J., Wang, Y., Gao, W., Shepard, A., Naughton, J. R., **Peng, Y.**, T. Paudel, T., Lan, Y., McMahon, G., Burns, M. J., Clary, M., Ballif, C., Haug, F-J., Söderström, T., Cubero, O., and Eminian, C., "Nanocoax: A New Platform for Low Cost, High Efficiency Solar Power," Phys. Status Solidi RRL 4, No. 7, 181-183 (2010).

Nelayah, J., Gu, L., Sigle, W., Koch, C. T., Pastoriza-Santos, I., Liz-Marzán, L. M., and Aken, P. A. van, "Direct imaging of surface plasmon resonances on single triangular silver nanoprisms at optical wavelength using low-loss EFTEM imaging", Optics Letters 34, 1003 (2009).

Novikov, I.V. and Maradudin, A.A., "Channel Polaritons". Phys. Rev. B 66, 035403 (2002).

Novotny, L., and Hecht, B., "Principles of Nano-Optics", Cambridge University Press, Cambridge, (2006).

Ordal, M. A., Bell, R. J., Alexander, R. W. Jr., Long, L. L., and Querry, M. R., "Optical properties of fourteen metals in the infrared and far infrared: Al, Co, Cu, Au, Fe, Pb, Mo, Ni, Pd, Pt, Ag, Ti, V, and W", Applied Optics, Vol. 24, Issue 24, pp. 4493-4499 (1985)

Okamoto, T., Yamamoto, M., and Yamaguchi, I., "Optical waveguide absorption sensor using a single coupling prism", JOSA A, Vol. 17, Issue 10, 1880-1886 (2000).

Oskooi, A. F., Kottke, C., and Johnson, S. G., "Accurate finite-difference time-domain simulation of anisotropic media by subpixel smoothing," Optics Letters 34, 2778–2780 (2009).

Oskooi, A. F., Roundy, D., Ibanescu, M., Bermel, P., Joannopoulos, J. D., and Johnson, S. D., "MEEP: A flexible free-software package for electromagnetic simulations by the FDTD method," Computer Physics Communications 181, 687–702 (2010).

Otto, A., "Excitation of nonradiative surface plasma waves in silver by the method of frustrated total reflection", Zeitschrift fur Physik A Hadrons and Nuclei, 216, 398 (1968).

Paudel, T., Rybczynski, J., Gao, Y.T., Lan, Y.C., Peng, Y., Kempa, K., Naughton, M.J., Ren, Z.F., "Nanocoax solar cells based on aligned multi-walled carbon nanotube arrays", Phys. Status Solidi A, 1- 4 (2011).

Pendry, J.. “Negative Refraction makes a perfect lens”, Phys. Rev. Lett. 85, 396 (2000).

Peng, **Y.,** Wang, X., and Kempa, K., "TEM - like optical mode of a coaxial nanowaveguide", Opt. Express 16, 1758-1763 (2008).

Peng, **Y.,** Marcoux, C., Kempa, K., Patoka, P., Hilgendorff, M., Giersig, M., “Plasmonics of thin film quasi-triangular nanoparticles”, Applied Physics Letters 96, 133104 (2010).

Peng, **Y.,** Paudel, T., Chen, W., Padilla, W.J., Ren, Z.F., and Kempa, K., “Percolation and polaritonic effects in periodic planar nanostructures evolving from holes to islands”, Applied Physics Letters 90, 041901 (2010)

Pernice, W.H.P., Payne, F.P., Gallagher, D.F.G., “An FDTD method for the simulation of dispersive metallic structures”, Opt. Quantum Electron. 38, 843 (2006)

Peters, M., Rüdiger, M., Hermle, M., Bläsi, B., “Photonic Crystals in Solar Cells – a Simulation Approach”, Photonics for Solar Energy Systems III, Proc. of SPIE, Vol. 7725, 772514 (2010).

Pile, D. F. P., and Gramotnev, D. K., “Channel plasmon-polariton in a triangular groove on a metal surface”, Optics Letters, Vol. 29, Issue 10, 1069-1071 (2004)

Pines, D., “Collective Energy Losses in Solids”, Rev. Mod. Phys. 28, 184 (1956).

Pitarke, J.M., Silkin, V.M., Chulkov, E.V., and Echenique, P.M., “Theory of surface plasmons and surface-plasmon polaritons”. Rep. Prog. Phys. 70, 1 (2007).

Powell C J and Swan J B., “Origin of the Characteristic Electron Energy Losses in Aluminum”, Phys. Rev. 115, 869 (1959).

Powell C J and Swan J B., “Origin of the Characteristic Electron Energy Losses in Magnesium”, Phys. Rev. 116, 81 (1959).

Pozar, D. M., “Microwave Engineering”, 3rd edition, John Wiley & Sons, Inc. (2005).

Quinn, J.J., “Bulk and surface plasmons in solids”, Nuclear Instruments and Methods in Physics Research B, 96, 460 (1995).

Quinten, M., Leitner, A., Krenn, J.R., and Aussenegg, F.R., “Electromagnetic energy transport via linear chains of silver nanoparticles”, Opt. Lett. 23, 1331 (1998).

Raether, H., “Surface Plasmons on Smooth and Rough Surfaces and on Gratings”, Springer-Verlag, (1988).

Rakic, A.D., Djurisic, A. B., Elazar, J. M., Majewski, M. L., "Optical Properties of Metallic Films for Vertical-Cavity Optoelectronic Devices", Appl. Opt. 37, 5271 (1998).

Ren, Z. F., Huang, Z. P., Xu, J. W., Wang, J. H., Bush, P., Siegal, M. P., Provencio, P. N., "Synthesis of Large Arrays of Well-Aligned Carbon Nanotubes on Glass", Science 282, 1105 (1998).

Ritchie, R.H., " Plasma losses by fast electron in thin films", Phys. Rev. 106, 874 (1957).

Ritchie, R. H., and Eldridge, H. B., "Optical Emission from Irradiated Foils. I", Phys. Rev. 126, 1935 (1962).

Ritchie, R. H., Arakawa, E. T., Cowan, J. J., and Hamm, R. N., "Surface-plasmon resonance effect in grating diffraction", Phys. Rev. Lett. 21, 1530 (1968).

Rodrigo, S.G., Garcia-Vidal, F.J., Martin-Moreno, L., "Influence of material properties on extraordinary optical transmission through hole arrays", Phys. Rev. B77, 075401 (2008).

Ropp, C. Probst, R., Cummins, Z., Kumar, R., Berglund, A. J., Raghavan, S. R., Waks, E., and Shapiro, B., "Manipulating Quantum Dots to Nanometer Precision by Control of Flow", *Nano. Lett.* 10, 2525-2530, (2010).

Ropp, C., Cummins, Z., Probst, R., Qin, S., Fourkas, J. T., Shapiro, B., and Edo Waks,*E.*, "Positioning and Immobilization of Individual Quantum Dots with Nanoscale Precision", *Nano. Lett.*, 10, 4673-4679 (2010).

Rybczynski, J., Kempa, K., Herczynski, A., Wang, Y., Naughton, M. J., Ren, Z. F., Huang, Z. P., Cai, D., and Giersig, M., "Subwavelength waveguide for visible light," Appl. Phys. Lett. 90, 021104 (2007).

Sanchez-Iglesias, A., Pastoriza-Santos, I., Pérez-Juste, J., Rodríguez-González, B., García de Abajo, F. J., and Liz-Marzán, L. M., "Synthesis and Optical Properties of Gold Nanodecahedra with Size Control", Adv. Mater. 18, 2529 (2006).

Sanders, A. W., Routenberg, D. A., Wiley, B. J., Xia, Y., Dufresne, E. R., and Reed, M. A., "Observation of Plasmon Propagation, Redirection, and Fan-Out in Silver Nanowires", Nano Lett., 6, pp 1822-1826 (2006).

Scaffardi L. B., and Tocho, J O., "Size dependence of refractive index of gold nanoparticles", Nanotechnology 17, 1309 (2006)

Scharte, M., Porath, R., Ohms, T., Aeschlimann, M., Krenn, J. R., Ditlbacher, H., Aussenegg, F. R., and Liebsch, A., "Do Mie plasmons have a longer lifetime on resonance than off resonance?", Appl. Phys. B 73, 305 (2001).

Schwartzberg, A.M., and Zhang, J. Z., "Novel Optical Properties and Emerging Applications of Metal Nanostructures", Journal of Phys. Chem. C 112, 10323 (2008).

Schider, G., Krenn, J. R., Hohenau, A., Ditlbacher, H., Leitner, A., Aussenegg., F. R., Schaich, W. L., Puscasu, I., Monacelli, B., and Boreman, G., "Plasmon dispersion relation of Au and Ag nanowires", Phys. Rev. B. 68, 155427 (2003).

Scott, C., "Introduction to Optics and Optical Imaging". Wiley, (1998).

Skinner, N.G., Byrne, D.M., "Finite-difference time-domain analysis of frequency-selective surfaces in the mid-infrared", Appl. Opt. 45, 1943 (2006).

Shalaev, V. M., and Kawata, S., "Nanophotonics with Surface Plasmons", Elsevier, (2007).

Shen, S., Kuang, Zh.-B., and Hu, S., "Wave propagation in multilayered anisotropic media", Mechanics Research Communications, 25, 5, 503-507 (1998).

Smolyaninov, I. I., Mazzoni, D. L., and Davis, C. C., "Imaging of Surface Plasmon Scattering by Lithographically Created Individual Surface Defects," Phys. Rev. Lett. 77, 3877 - 3880 (1996).

Smolyaninov, I. I., Mazzoni, D. L., Mait, J., and Davis, C. C., "Experimental study of surface-plasmon scattering by individual surface defects," Phys. Rev. B 56, 1601-1611 (1997).

Siemens & Halske, "Neuerung in dem verfahren zur herstellung isolirter leitungen," Kaiserliches Patentamt, Berlin, Patentschrift No. 28978 (1884).

Stauffer, D., Arahony, A., "Introduction to Percolation Theory", Taylor & Francis (2001).

Stepanov, A. L., Krenn, J. R., Ditlbacher, H., Hohenau, A., Drezet ,A., Steinberger, B., Leitner, A., and Aussenegg, F. R., "Quantitative analysis of surface plasmon interaction with silver nanoparticles," Opt. Lett. 30, 1524-1526 (2005).

Stern E A and Ferrell R A., "Surface Plasma Oscillations of a Degenerate Electron Gas", Phys. Rev. 120 130 (1960).

Sun, Y. G., Yin, Y. D., Mayers, B. T., Herricks, T. & Xia, Y. N. “Uniform Silver Nanowires Synthesis by reducing AgNO3 with Ethylene Glycol in the Presence of Seeds and Poly(vinyl pyrrolidone)”. Chem. Mater. 14, 4736- 4745, (2002).

Sun, Y., Mayers, B., Herricks, T. & Xia, Y. Polyol Synthesis of Uniform Silver Nanowires: “A Plausible Growth Mechanism and the Supporting Evidence”. Nano. Lett. 3, 955-960, (2003).

Swanson, D.G., “Plasma Waves”, (Series in Plasma Physics), 2nd edition. Taylor & Francis (2003).

Sweatlock, L. A., Maier, S. A. and Atwater, H. A. “Microwave analogue to a subwavelength plasmon switch”, In: Electronic Components and Technology Conference, 53rd (ECTC '03), New Orleans, LA, 27-30 May (2003).

Sweatlock, L. A., “Plasmonics: Numerical Methods and Device Applications”, phd thesis, Cal tech, (2008).

Takahara, J., Yamagishi, S., Taki, H., Morimoto, A., and Kobayashi, T., “Guiding of a one-dimensional optical beam with nanometer diameter,” Opt. Lett. 22, 475 (1997).

Taflove, A., “Computational Electrodynamics—The Finite-Difference Time-Domain Method”, Artech House, Norwood, MA, (1995).

Taflove, A., Brodwin, M.E. "Numerical solution of steady-state electromagnetic scattering problems using the time-dependent Maxwell's equations". IEEE Transactions on Microwave Theory and Techniques 23: 623–630 (1975).

Taflove, A., Brodwin, M.E. “"Computation of the electromagnetic fields and induced temperatures within a model of the microwave-irradiated human eye". IEEE Transactions on Microwave Theory and Techniques 23: 888–896 (1975).

Taflove A., and Hagness, S. C., “Computational Electrodynamics: The Finite-Difference Time-Domain Method”, 3rd edition, Artech: Norwood, MA, (2005).

Tao, A. R., and Yang, P., “Polarized Surface-Enhanced Raman Spectroscopy on Coupled Metallic Nanowires”. J. Phys. Chem. B 109, 15687-15690 (2005).

Tesla, N., “Electrical conductor,” U.S. Patent No. 514167, Feb 6 (1894).

Thio T., Ghaemi, H. F., Lezec, H. J., Wolff, P. A., and Ebbesen, T. W., "Surface-plasmon-enhanced transmission through hole arrays in Cr films," J. Opt. Soc. Am. B 16, 1743-1748 (1999).

Vandenbem, C., and Vigneron, J. P., “Mie Resonances of dielectric spheres in face-centered cubic photonic crystals”, J., Optical Society of America, A 22, 1042 (2005).

Vial, A., Grimault, A.-S., Macías, D. Barchiesi, D., Lamy de la Chapelle, M., “Improved analytical fit of gold dispersion: Application to the modeling of extinction spectra with a finite-difference time-domain method”, Phys. Rev. B 71, 085416 (2005).

Vial, A., Laroche, T., “Comparison of gold and silver dispersion laws suitable for FDTD Simulations”, Appl Phys B, 93: 139–143 (2008).

Wang X., and Kempa, K., “Plasmon polaritons in slot waveguides: Simple model calculations and a full nonlocal quantum mechanical treatment,” Phys. Rev. B 75, 245426 (2007).

Wang X., and Kempa, K., “Negative Refraction and Subwavelength Lensing in a Polaritonic Crystal”, Phys. Rev. B 71, 233101 (2005).

Wang, Y., Wang X., Rybczynski, J., Wang, D. Z., Kempa, K., and Ren, Z. F., “Triangular lattice of carbon nanotube arrays for negative index of refraction and subwavelength lensing effect”, Appl. Phys. Lett. 85, 4741 (2004).

Wang, Y., Plummer, E. W., and K. Kempa. K., “Foundations of Plasmonics”, submitted.

Wang Y., Kempa, K., Kimball, B., Carlson, J. B., Benham, G., Li, W. Z., Kempa, T., Rybczynski, J., Herczynski, A., and Ren, Z. F., “Receiving and transmitting light like radio waves: antenna effect in arrays of aligned carbon nanotubes”, Appl. Phys. Lett. 85, 2607-2609 (2004). *Reported in Nature and Science News, AIP, CNN and ABC and more.*

Wang, Z. L., Mohamed, M. B., S. Link, M. A. El-Sayed, “Crystallographic facets and shapes of gold nanorods of different aspect ratios”, Surf. Sci. 440, L809 (1999).

Waterman, P. C., “Symmetry, unitarity, and geometry in electromagnetic scattering”, Phys. Rev. D, 3, 825 (1971).

Willardson, R.K., Pankove, J. I., and Beer, A. C., “Hydrogenated Amorphous Silicon: Optical properties”, Academic Press, (1984).

Wilk, T., Webster, S. C., Kuhn, A. & Rempe, G. “Single-atom single-photon quantum interface”, Science 317, 488-490 (2007).

Wood, R. W., “On a remarkable case of uneven distribution of light in a diffraction grating spectrum”, Phil. Mag. 4, 396 (1902).

Wu, R.F., Pan, W., Shi, S.L., and Han, R. B., “Critical behaviors of the conductivity and dielectric constant of Ti_3SiC_2/Al_2O_3 hybrids”, Journal of Applied Physics 102, 056104 (2007).

Yee, K. S., “Numerical solution of initial boundary value problems involving Maxwell’s equations in isotropic media”, IEEE Transactions on Antennas Propagation. 14, 302 (1966).

Yang, W. H., Schatz, G. C., and Van Duyne, R. P., “Discrete dipole approximation for calculating extinction and Raman intensities for small particles with arbitrary shapes”, J. Phys. Chem. 103, 869 (1995)

Yablonovitch, E., Gmitter, T. J., and Leung, K. M., "Photonic band structure: The face-centered-cubic case employing nonspherical atoms," Phys. Rev. Lett. 67, 2295-2298 (1991).

Yariv, A., and Yeh, P., “Optical Waves in Crystals: Propagation and Control of Laser Radiation”, (Wiley Series in Pure and Applied Optics), John Wiley and Sons, (1984).

Yuan, H., E, W., and Palffy-Muhoray, P., “Analytical solution of Maxwell’s equations in lossy and optically active crystals”, Phys. Rev. E 61, 3264–3266 (2000).

Zallen, R., “The Physics of Amorphous Solids”, J. Wiley and Sons, New York, (1983).

Zentgraf, T., Meyrath, T. P., Seidel, A., Kaiser, S., Giessen, H., Rockstuhl C., and Lederer, F., “ Negative-index metamaterials from nanoapertures”, Phys. Rev. B 76, 125426 (2007).

Notes:

Note 1: The Lorentzian expansion of the Au dielectric function used in the simulations was fitted to the experimental data given in P. B. Johnson and R. W. Christy, Phys. Rev. B 6, 4370 (1972). However to aid the code convergence, the imaginary part was increased, which leads to broader resonance peaks (inset in Fig. 3), as compared to those from the experiment (inset in Fig. 2). This purely numerical adjustment did not affect significantly the peak maxima locations, the main feature studied in this work.

Note 2: This assures the non-retarded limit at the frequencies of interest.

Note 3: This small threshold adjustment is numerical and due to the finite size of the mesh (5 nm) used in the FDTD simulations.

Appendix:

- The file code for the 4th figure is attached as below as an example, among hundrends of MEEP control files that have been run for this dissertation.

```
;square symmetry
;carbon nanotube coaxial

(define-param fcen 0.2)
(define-param sx 4)
(define-param sy 4)
(define-param sz 21)
(define-param lz 10)
(define-param dpml 0.5)
(set-param! resolution 20)

(define force-complex-fields? false)
(set! ensure-periodicity true)

(define eps-averaging? false)

; angle in degrees.
(define-param theta_deg 30)

(define-param mat (make dielectric (epsilon 1)
        (polarizations
         (make polarizability
           (omega 1e-20) (gamma 0.001) (delta-epsilon 0.3e40))
        )))
```

```
(define-param subs (make dielectric (epsilon 25)
        (polarizations
         (make polarizability
           (omega 0.2) (gamma 0.2) (delta-epsilon 1))
        )))

(define-param buff (make dielectric (epsilon 5)
))

(define-param glass (make dielectric (epsilon 2)
))

(set! geometry-lattice (make lattice (size sx sy sz)))

(set! geometry
         (append
          (list
           (make block (center 0 0 1.5) (size sx  sy  11)
                (material buff))
           (make block (center 0 0 -4.28) (size sx sy 0.56)
                (material buff))
           (make cylinder (center 0 0 1.5) (radius 1.5) (height 11)
                (material subs))
           (make cylinder (center 0 0 2) (radius 0.5) (height lz)
                (material mat))
             (make block (center 0 0 8.5) (size sx sy 3)
                (material subs))
)))

(set! pml-layers (list (make pml (direction Z) (thickness dpml))))
```

```
    ;;;;;;;;;;;;;;;make the incident wave be tilted certain degrees
    (define ((pw-amp k x0) x)
      (exp (* 0+1i (vector3-dot k (vector3+ x x0)))))

    (define theta_rad (/ (* pi theta_deg) 180))

    ; direction of k (length is irrelevant)
    (define-param kdir (vector3 (sin theta_rad) 0 (cos theta_rad)))

    (set! k-point (vector3-scale fcen (unit-vector3 kdir)))

    ; k with correct length
    (define k (vector3-scale (* 2 pi fcen) (unit-vector3 kdir)))
    ;;;;;;;;;;;;;;;;

    (define-param source-component Ex)

    (set! sources (list
           (make source
            (src (make continuous-src (frequency fcen)))
            (component source-component)
           (center 0 0 (+ dpml (* -0.5 sz)))
           (size sx sy 0)
            (amp-func (pw-amp k (vector3 0 0 (* -0.5 sx)))))
    ))

    (run-until 120
       ;    (at-every 10 (output-png source-component "-y 0x0 -Zc dkbluered"))
             (to-appended "ex" (at-every 20 output-efield-x))
    )
;end
```

- More nanowire analysis

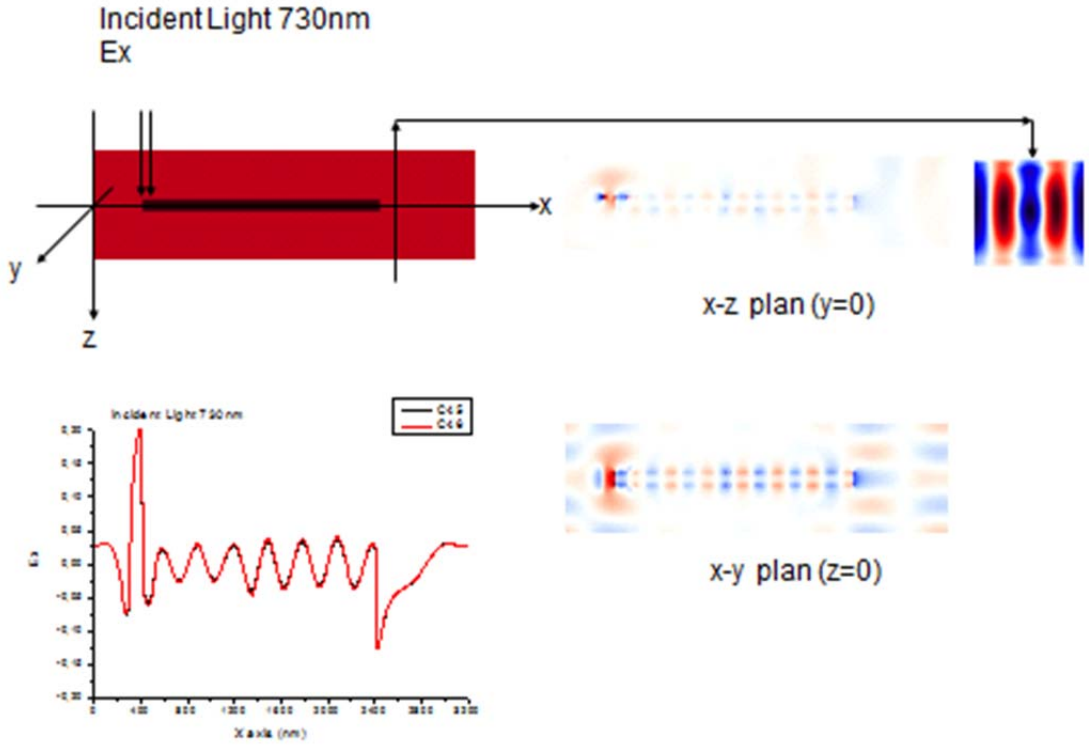

Above figure is part of an analysis of light propagation along Ag nanowire of 2um length and 100nm diameter. Ex polarized light of 730nm is incident as shown onto one end of the Ag nanowire, and the electric field maps at different cross sections are labeled and shown on the right. The field maps along x-direction (both x-z plane and x-y plane) show clearly the propagation of the SPPs. Bottom left is a plot of the Ex field along x-axis, showing the field enhancement on the ends of the nanowires.

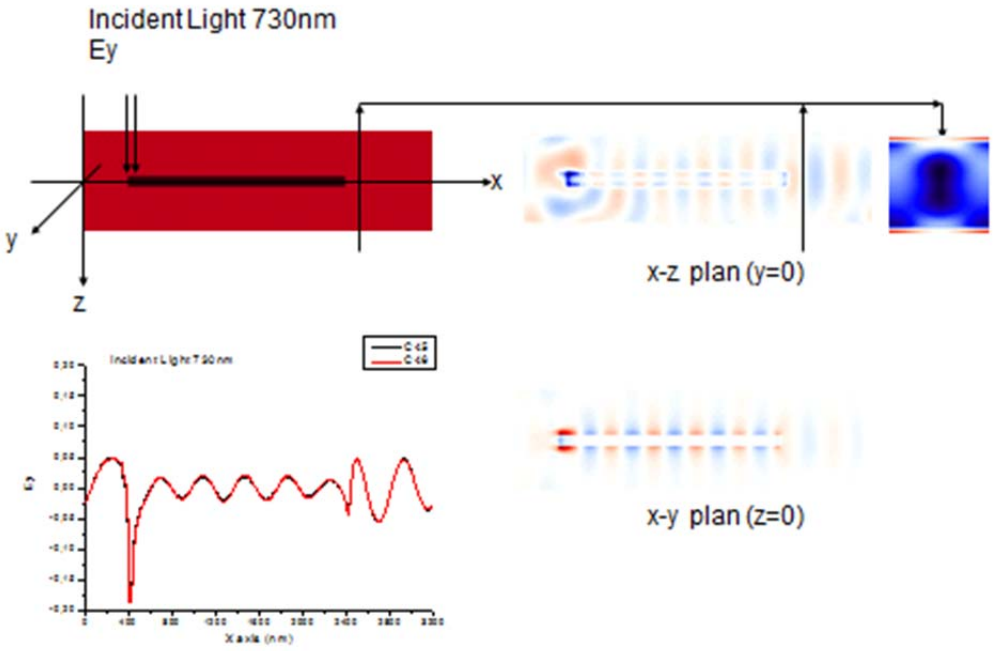
Incident Light 730nm
Ey
x
y
z
x-z plan (y=0)
x-y plan (z=0)

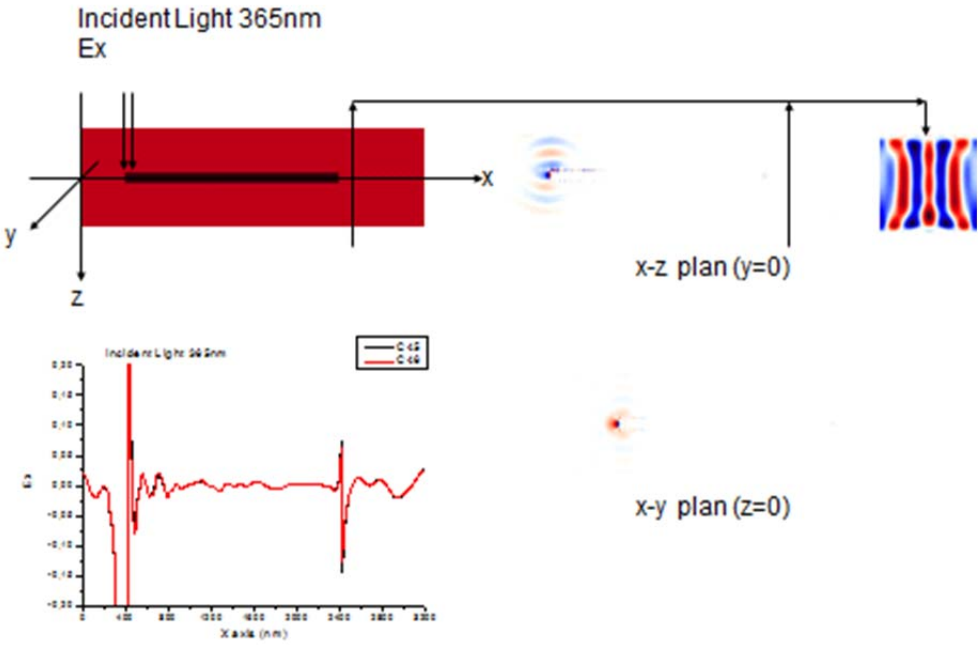
Incident Light 365nm
Ex
x
y
z
x-z plan (y=0)
x-y plan (z=0)

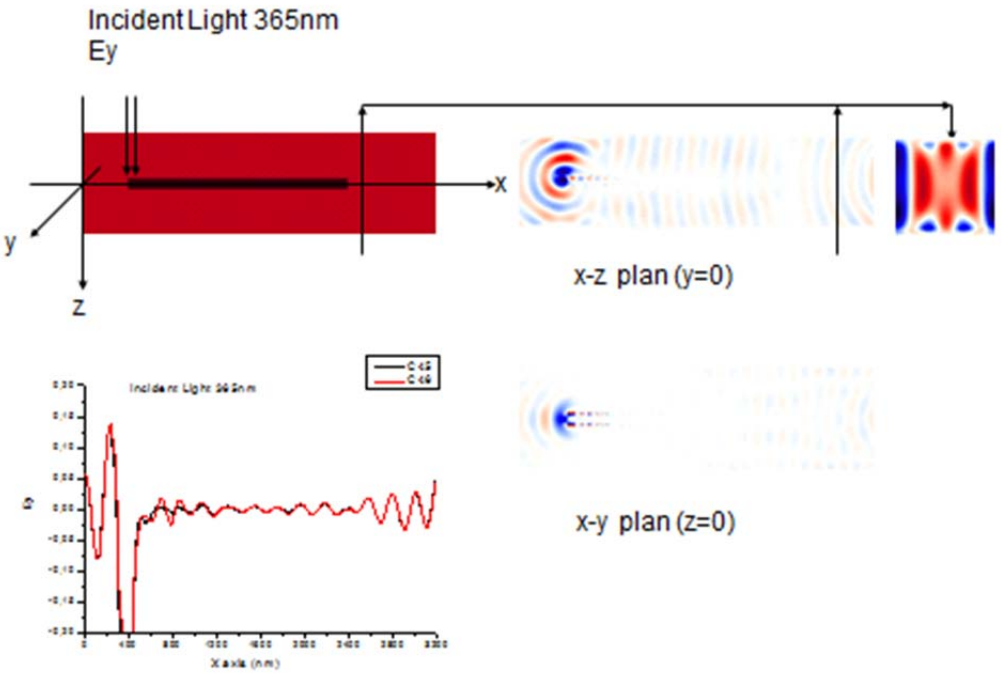

Above three figures are the same as the first one, except that the incident light is Ey polarized light of 73n0m wavelength; Ex polarized light of 365nm wavelength; Ey polarized light of 365nm wavelength respectively.

- Series of pictures of the electric field distribution evolving over time illustrate that propagation of SPPs along the silver nanowire.

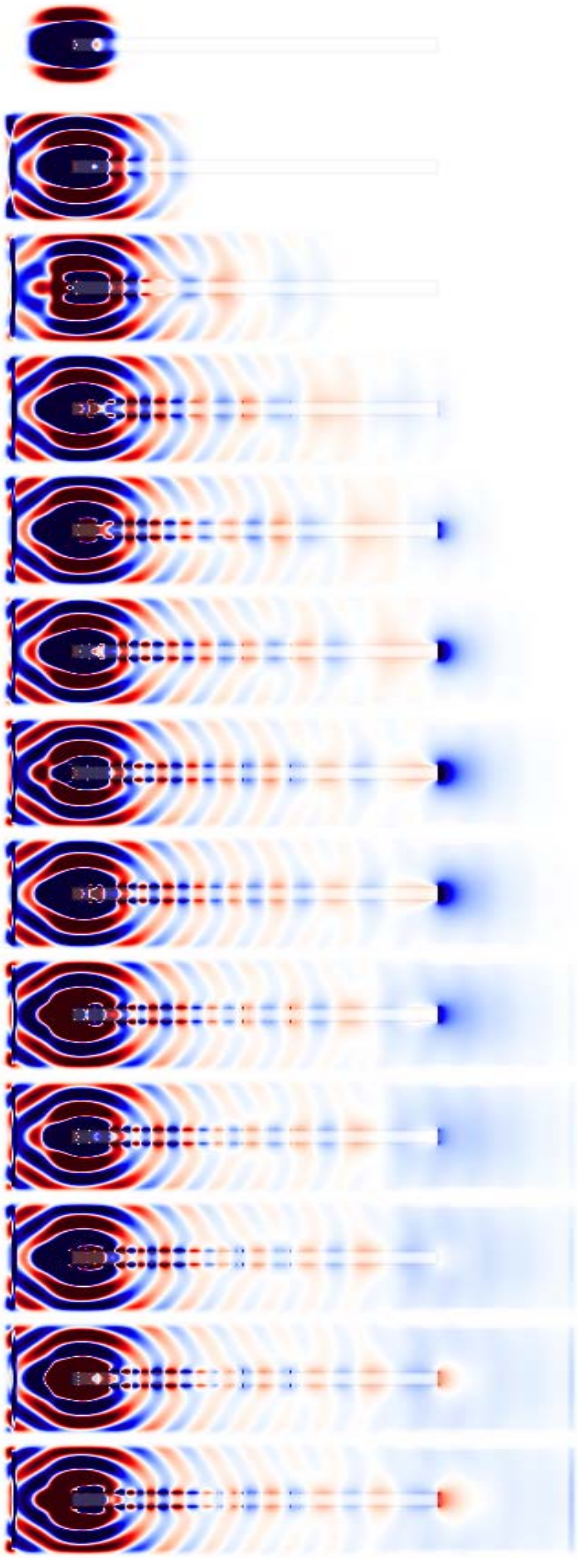

- Convergence analysis at different resolutions

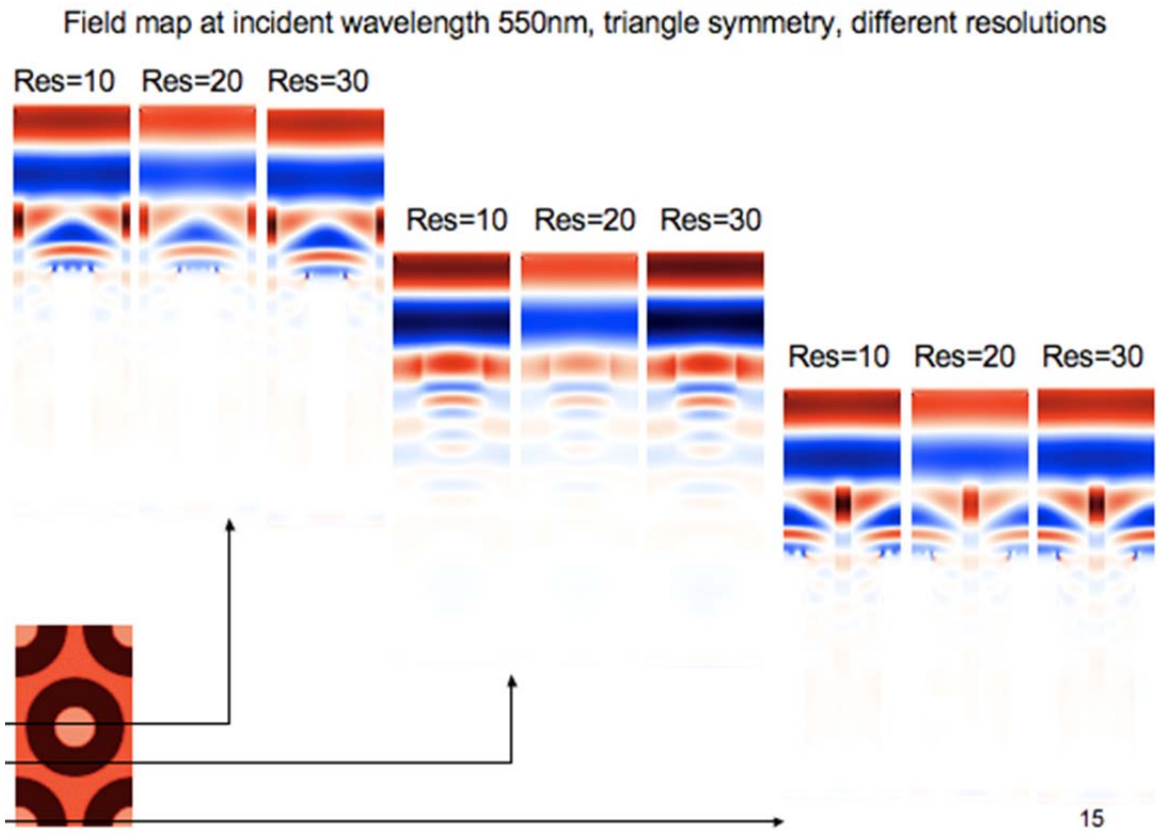

Above figure shows the one set of the results for convergence analysis of the simulation. The same simulation as in above figure is a convergence analysis: field maps of the same cross sections of HCP structure and at different resolutions. The color intensity is proportional to the field amplitude, and color represents the sign (field direction). Fig. 7.4 was conducted, with changing the resolution level. The numbers (10, 20 and 30) mean how many grids are there in one unit (100nm) defined in MEEP. The field maps were plotted through the same three cross sections, and put together as below. It demonstrates the high quality of the simulations, insensitive to the changing resolution level (10, 20 or 30).

- Many simulations are done to observe the field distribution in different nano structures to study how light is propagating in nanostructures. Here are limited selected examples of the nano pillar array structure and the field maps at different cross sections and different times.

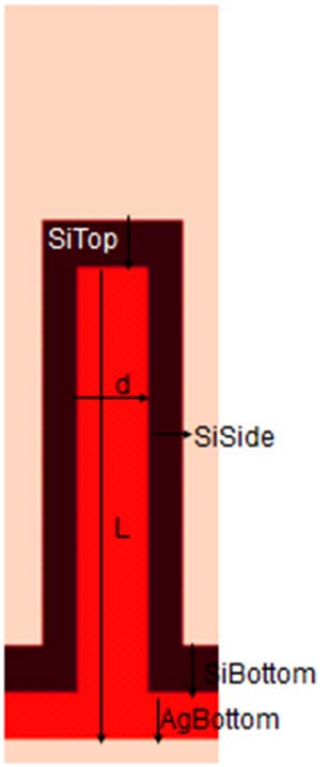

SiHCP9001

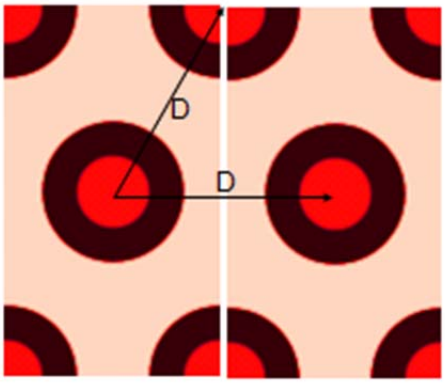

D=900nm

SiTop=200nm
SiSide=150nm
SiBottom=200nm
d=300nm (r=150nm)
L=2000nm
AgBottom=200nm

Field map at incident wavelength 700nm, HCP symmetry, resolution=10nm

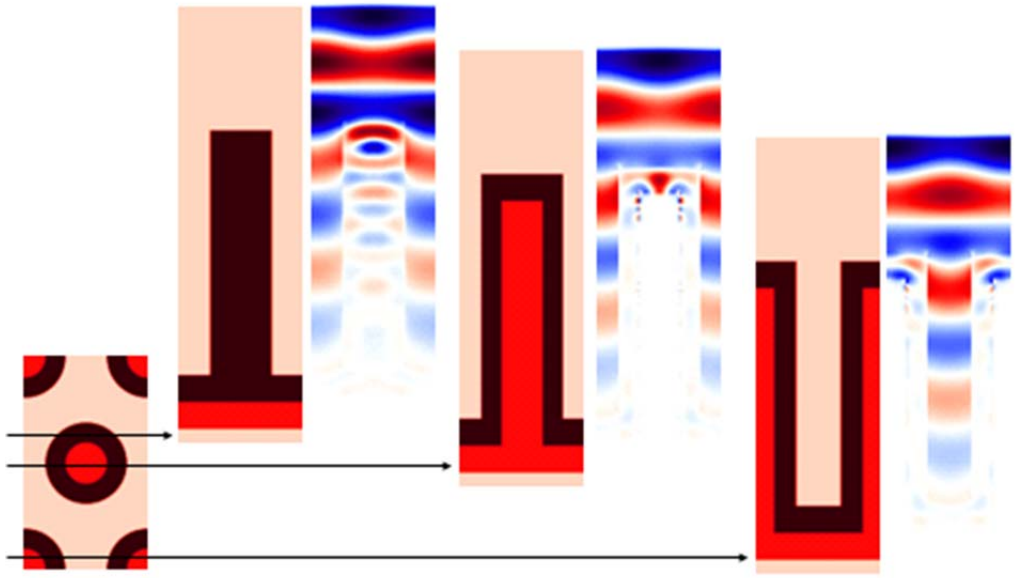

Field map at incident wavelength 700nm, HCP symmetry, resolution=10nm

Time increases →

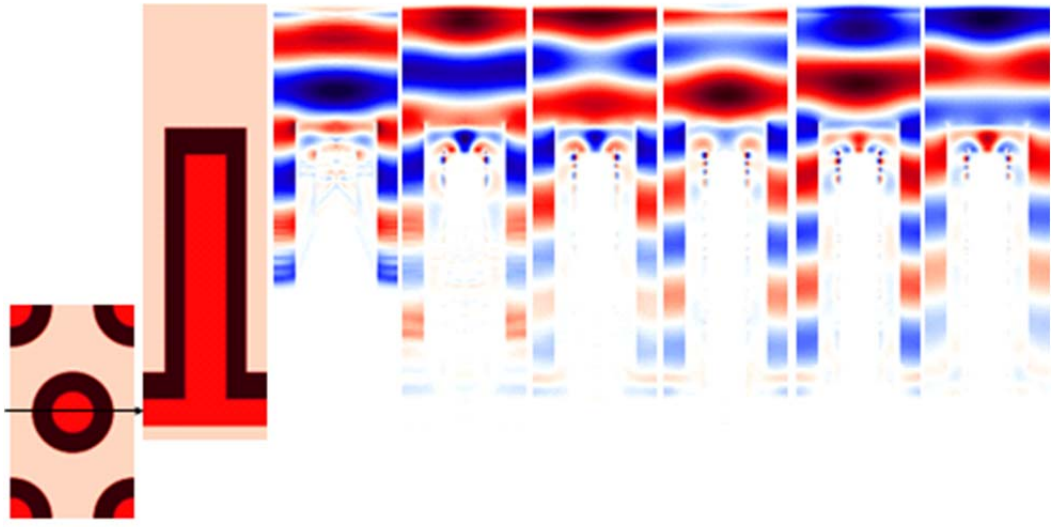

- Numerous simulations are also done when I am trying to optimize the absorbance. Here are limited selected examples of structures and corresponding absorbance.

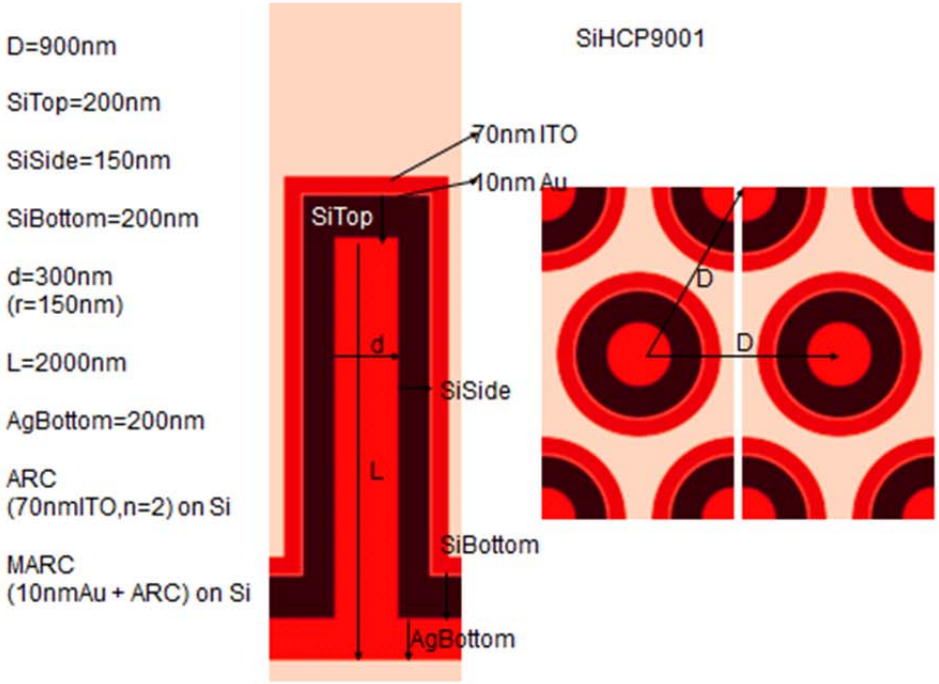

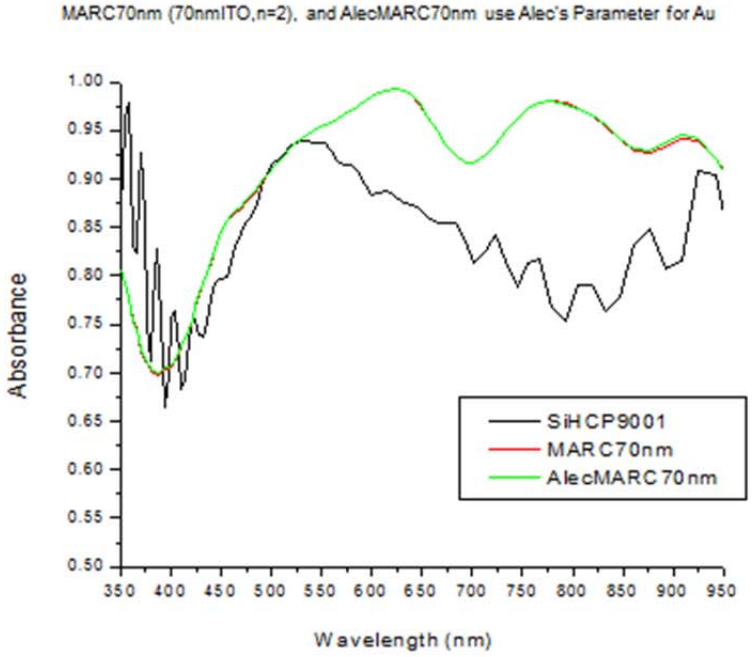

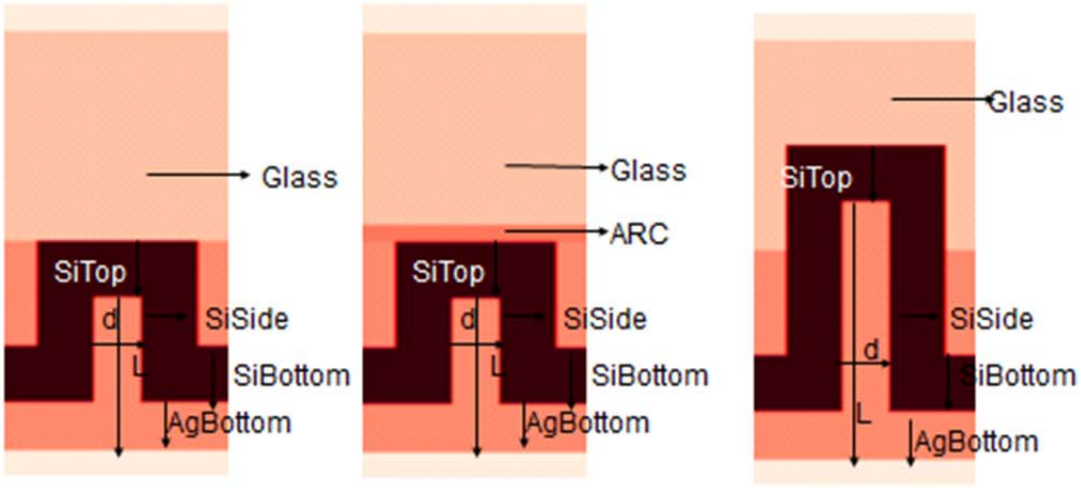

FatCylinder

SiTop=230nm
SiSide=230nm
SiBottom=230nm
d=194nm (r=97nm)
L=630nm
AgBottom=200nm

FatCylinderWithARC

SiTop=230nm
SiSide=230nm
SiBottom=230nm
d=194nm (r=97nm)
L=630nm
AgBottom=200nm

FatCylinderLonger

SiTop=230nm
SiSide=230nm
SiBottom=230nm
d=194nm (r=97nm)
L=1060nm
AgBottom=200nm

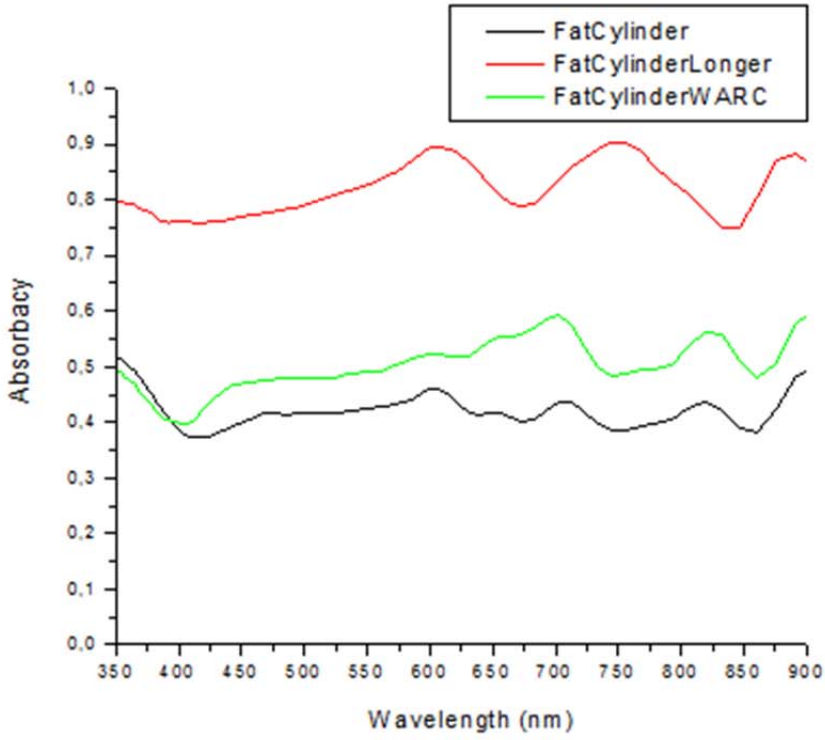

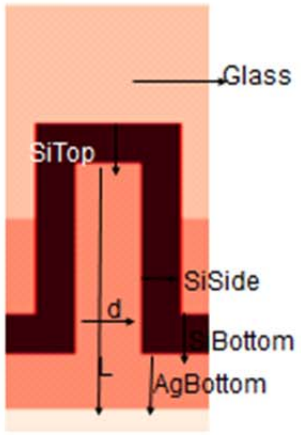

FatCylinderLonger Thinner1

SiTop=180nm
SiSide=180nm
SiBottom=180nm
d=294nm (r=147nm)
L=1110nm
AgBottom=250nm

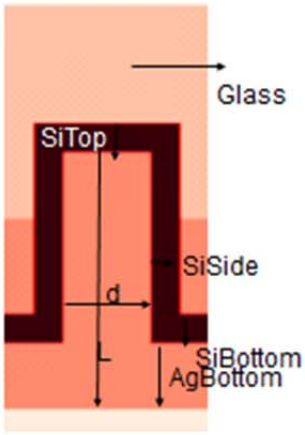

FatCylinderLonger Thinner2

SiTop=130nm
SiSide=130nm
SiBottom=130nm
d=394nm (r=197nm)
L=1160nm
AgBottom=300nm

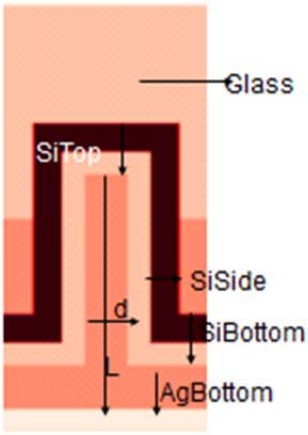

FatCylinderLonger Thinner2SiZnO

SiTop=130nm
SiSide=130nm
SiBottom=130nm
100nmZnO around Si
d=194nm (r=97nm)
L=1060nm
AgBottom=200nm

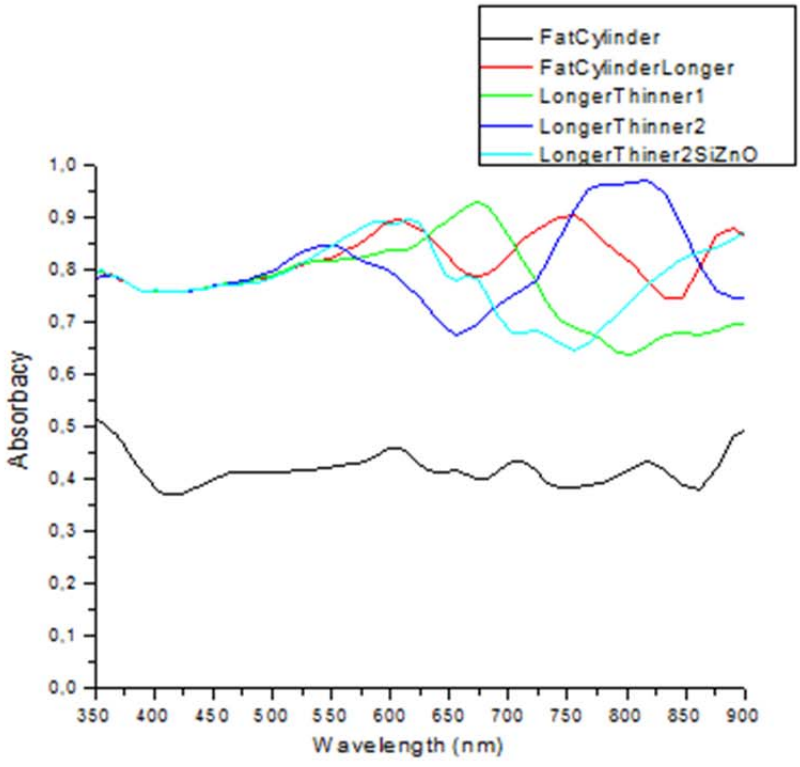

- Plasmonics of Nano particles of other shapes are also simulate

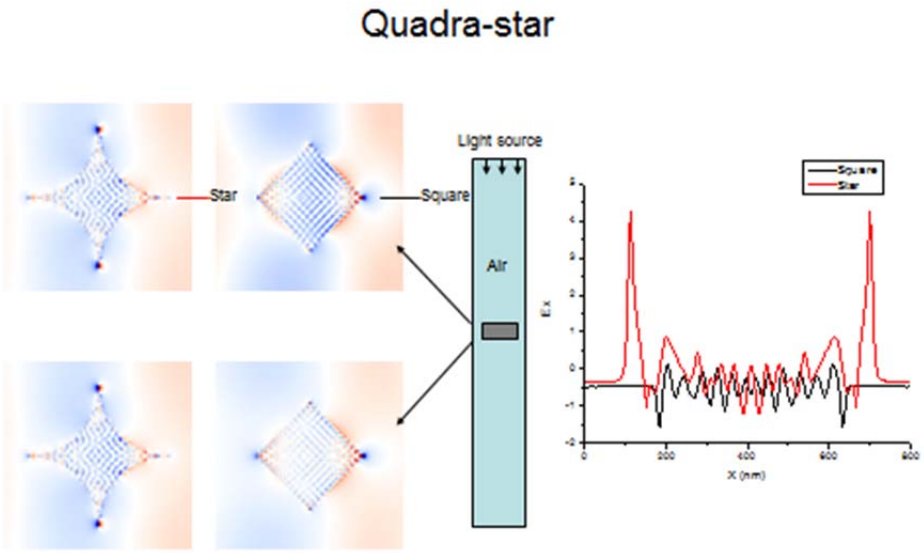

Above figure shows the field maps on top and bottom of the thin Ag square. The incident light is 500nm x-polarized plane wave incident from the top of the structure and propagates along z-direction. The Ag square is of 20nm thickness and 300nm on each side, and another shape (Quadro-star) that is made by cutting out part of the material from Ag square by using a circle of given diameter (1000nm in this case) on each of the four sides. The top two field maps are at the tops of the particle, and the bottom two correspond to the bottoms of the particle. The field is enhanced on the edges/sides of the triangle, and there are SPPs on the surface. The plot on the right shows the Ex field along the center (shown in figure) for both shapes.

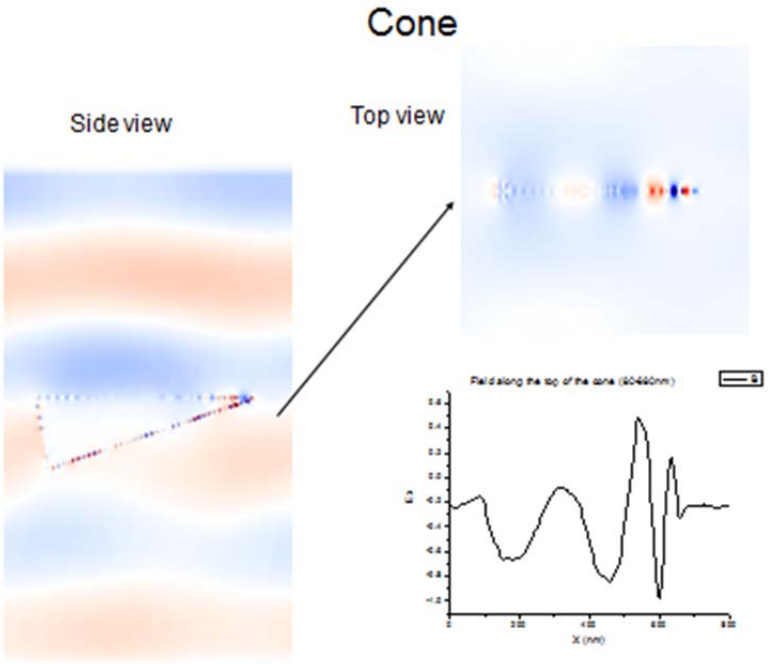

Same as last figure, except this is only for a cone showing the SPPs and Ex field.

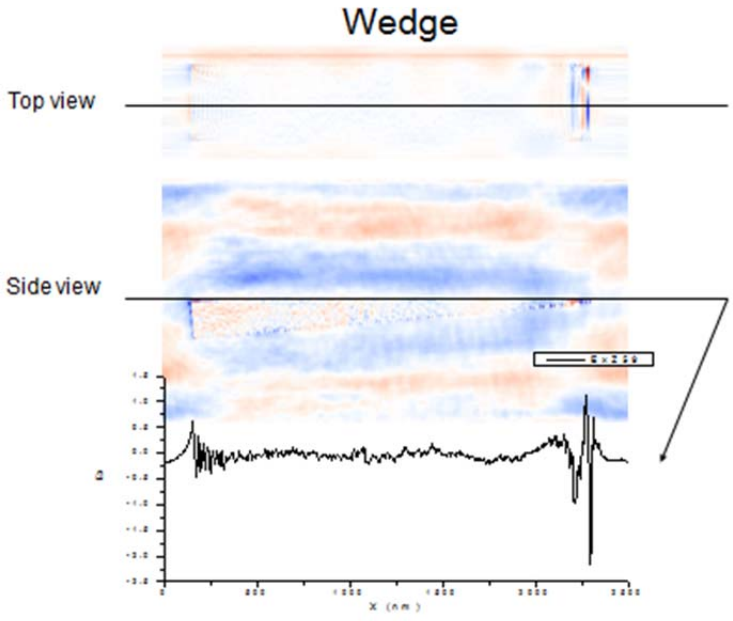

Same as last figure, except this is for a wedge showing the SPPs and Ex field.

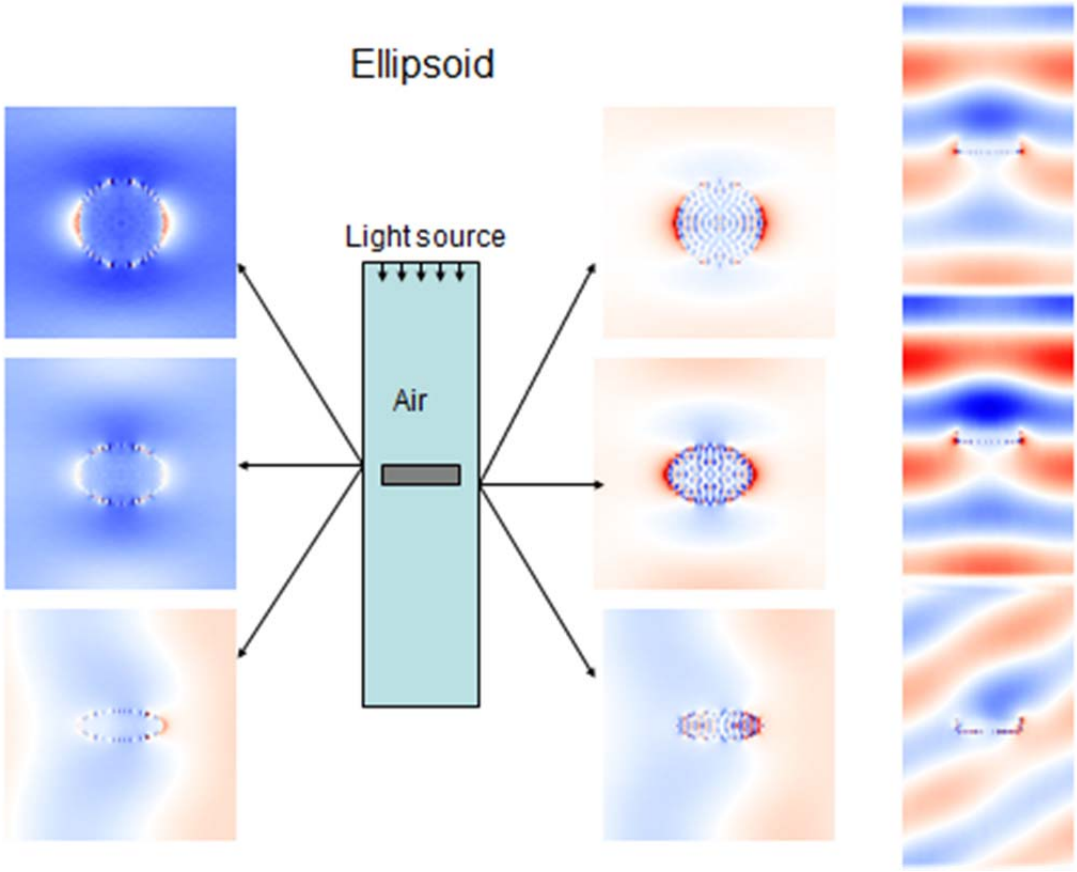

Above figure shows the field maps at three moments on top and bottom of a thin metal of Ellipsoid shape. The SPPs are visible, and the field in the whole space are on the right.

- Antenna Effect (EZNEC)

At the beginning of my phd work, I started by using a commercially available software EZ NEC to do simulations. Below is part of the study I did then. It provided some interesting information on how the parasitic antennas couple to a source, based on their lengths, and alignment directions etc. For all the configurations, the source antenna is

located at the origin of the reference frame. For each configuration, the plot on the right shows how the parasite antennas are located and aligned, and the plot on the left shows how the corresponding field is radiated in space.

I. Half wavelength parasite antennas

1. Random orientation of the parasites.

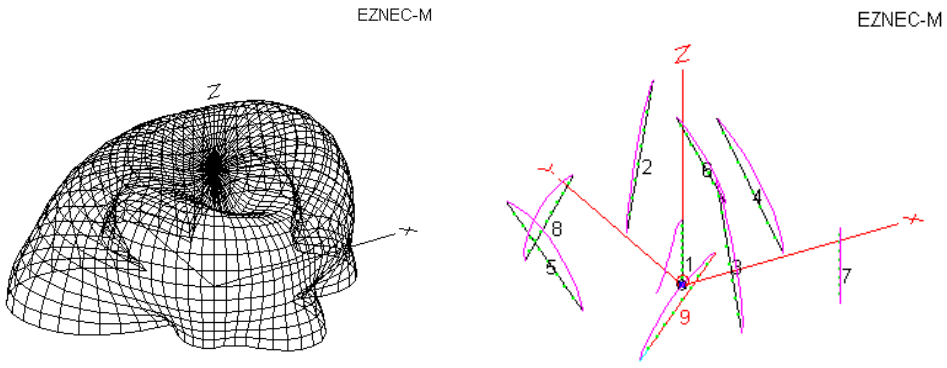

2. Some parasites are tilted 30 degrees.

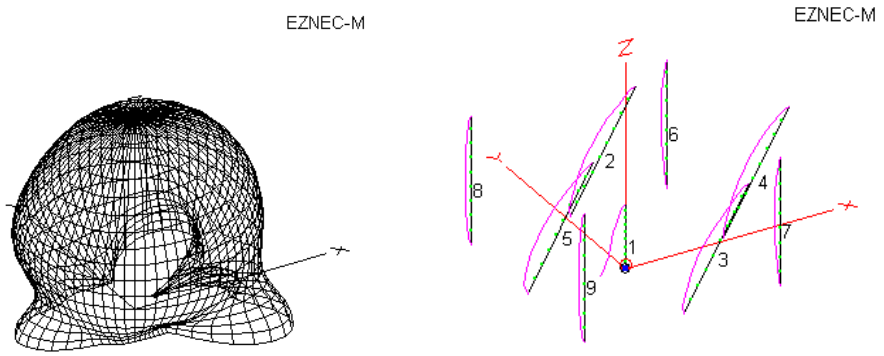

3. Different some of parasites tilted 30 degrees in one direction.

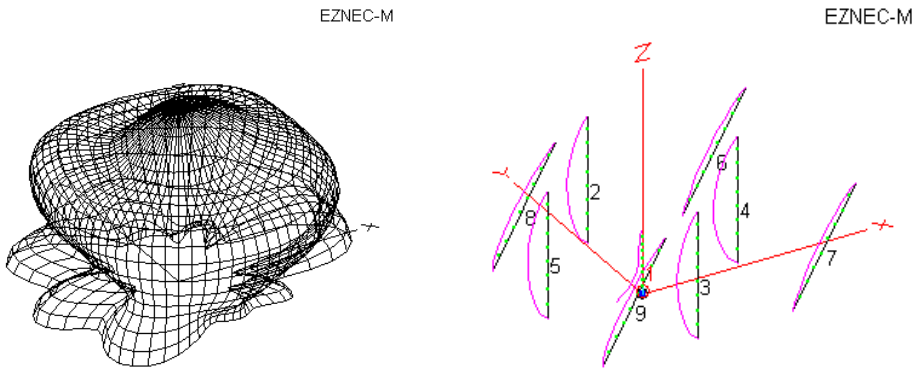

4. All parasites are tilted 30 degrees in one direction.

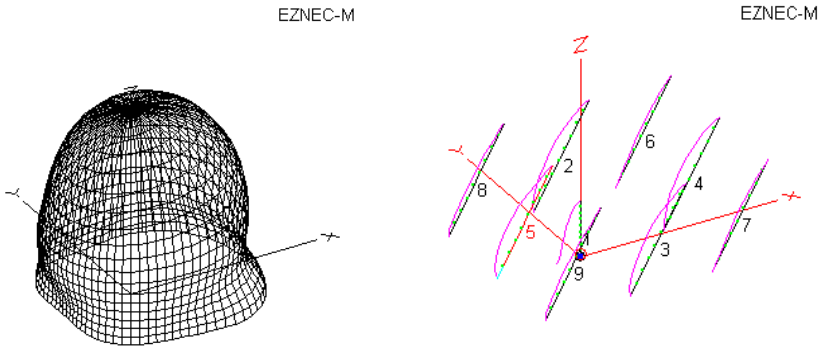

5. All parasites are tilted 45 degrees in one direction

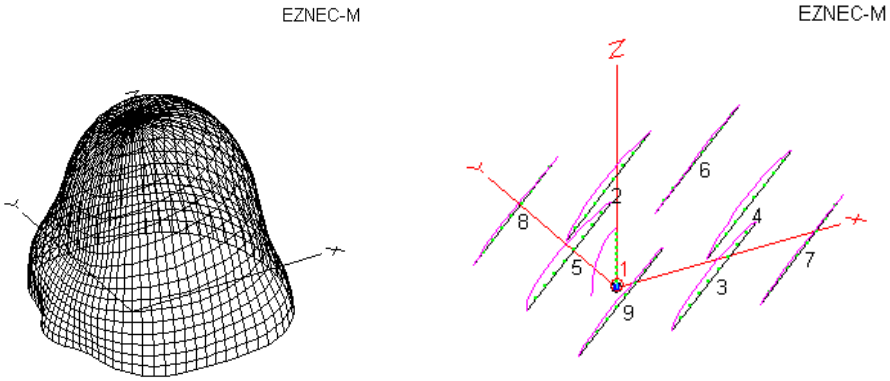

6. All parasites tilted 60 degrees in one direction.

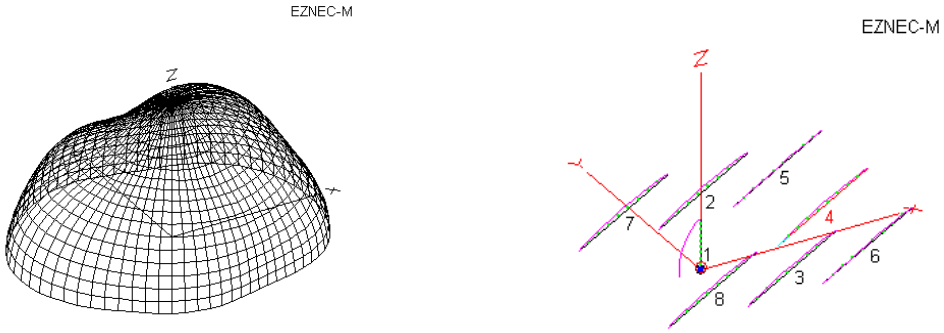

II. Quarter wavelength parasites

7. All parasites are straight up in one direction

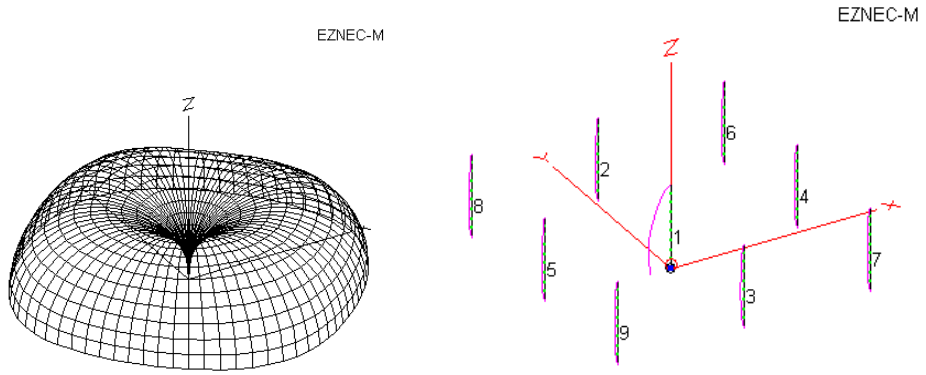

8. All parasites tilted 30 degrees in one direction

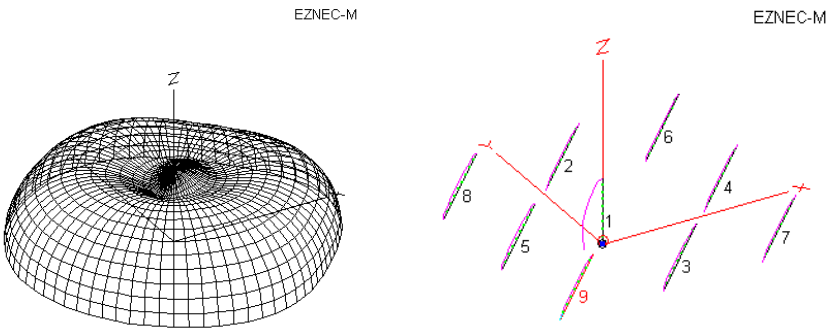

III. Three quatrer wavelength parasites

9. All parasites are straight up in one direction

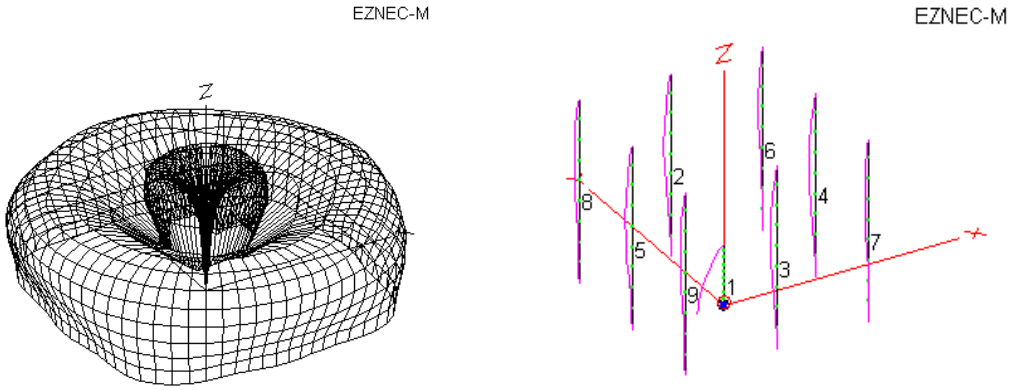

10. Three quarter wavelength parasites tilted 30 degees in one direction